

https://dspace.org/

First principle study of inorganic metal halide perovskites for solar cells application

Maleka, Prettier Morongoa

2024-08
University of the Witwatersrand, Johannesburg
https://hdl.handle.net/10539/45987
Maleka, Prettier Morongoa. (2024). First principle study of inorganic metal halide perovskites for solar cells application. [PhD thesis, University of the Witwatersrand, Johannesburg]. WIReDSpace. https://hdl.handle.net/10539/45987

Downloaded from a DSpace repository. https://dspace.org/

FIRST PRINCIPLE STUDY OF INORGANIC METAL HALIDE PEROVSKITES FOR SOLAR CELLS APPLICATION



A thesis submitted in partial fulfillment of the requirements for the degree of

Doctor of Philosophy

by

Prettier Morongoa Maleka

Supervisors: R.R. Maphanga and O.M. Ntwaeaborwa

Faculty of Science

University of Witwatersrand

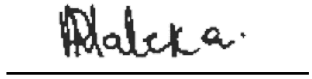
Acknowledgments

I am thankful to my supervisors Professor R.R. Maphanga, and Professor O.M. Ntwaeaborwa for their assistance, patience, and valuable guidance throughout the course of this project. Their dedication, effort and knowledge were vital to the project's success. I would also love to convey special thanks to Council for Scientific and Industrial Research in providing the financial support, facilities and other resources throughout my PhD studies. A Special thanks to the Centre for High Performance Computing for providing of high computing resources which enabled me to carry out simulations and calculations for this study.

I am thankful to my family: my mother (Christina Maleka), brothers, and sister for their support, as well as my spouse and son (Lucas Gailele and Resiamisitswe Gailele) for their loving, support and encouragement during the writing of my thesis. Studying for a PhD is a challenging experience, often accompanied by numerous failed attempts in the pursuit of new, encouraging results. During periods of stress, exhaustion, and a sense of hopelessness, having the support, encouragement, and understanding of others is crucial. Fortunately, my family and friends generously provided me with these essential needs.

Declaration

I, Prettier Morongoa Maleka, hereby declare that all the information provided is accurate and truthful. If necessary, I will provide the supporting documentation.



Date: August 15, 2024

Author Name

Abbreviations

PV	Photovoltaic
PSC	Perovskite Solar Cell
PCE	Power Conversion Efficiency
LED	Light Emitting Diodes
FF	Fill Factor
ETL	Electron Transport Layer
HTL	Hole Transport Layer
QD	Quantum Dots
DFT	Density Functional Theory
H-F	Hatree-Fock
H-K	Hohenburg and Kohn
H-S	Kohn and Sham
VASP	Vienna Ab initio Simulation
LDA	Local Density Approximation
GGA	Generalized Gradient Approximation
SCAN	Strongly Constrained and Appropriately Normed
BZ	Brillouin Zone
CE	Cluster Expansion
ECI	Elective Cluster Interaction
UNCLE	Universal Cluster Expansion
CVS	Cross Validation Score
PBE	Perdew, Burke and Ernzerhof
TDOS	Total Density of States
PDOS	Partial Density of States
CBM	Conduction Band Minimum
VBM	Valence Band Maximum
PAW	Projector Augmented Wave
HEG	Homogeneous Electron Gas
LUMO	Lowest Unoccupied Molecular Orbital

HOMO	Highest Occupied Molecular Orbital
MA	Methylammonium
FA	Formamidinium
TM	Transition Metal
IPCE	Incident-Photon-to-Current Efficiency
Pb	Highest Occupied Molecular Orbital
Sn	Tin
Ge	Germanium
MC	Monte-Carlo
CB	Conduction Band
VB	Valence Band

List of symbols

ρ	Electron density
$\hat{H}$	Hamiltonian operator
Ψ	Wavefunction
m	Electron mass
η	Efficiency
k	Boltzmann constant
n	Refractive index
$\hat{H}$	Reduced Planck constant
C_p	Specific heat
E_{xc}	Exchange-correlation energy
E_g	Energy bandgap
∇	Laplace operator
e	Elementary charge
k_B	Boltzmann constant
θ_D	Debye Temperature
v_s	Sound Velocity
E_F	Fermi Level
B	Bulk Modulus
G	Shear Modulus
Y	Young Modulus
v	Poisson Ratio
$\alpha(\omega)$	Absorption Coefficient
$k(\omega)$	Extinction Coefficient
$R(\omega)$	Reflectivity
$\sigma(\omega)$	Conductivity
$\varepsilon_1(\omega)$	Real Part Dielectric Function
$\varepsilon_2(\omega)$	Imaginary Part Dielectric Function
t	Goldschmidt's Tolerance Factor
μ	Octahedral Factor

Abstract

All-inorganic halide perovskites have received significant attention as semiconductor materials due to their outstanding opto-electronic properties, which have achieved power conversion efficiency (PCE) of up to 25% in perovskite solar cells. Their exceptional characteristics include long diffusion lengths for electrons and holes, tuneable band gap, high absorption coefficients, small effective masses, high carrier mobility, and simple reproducible process. Despite these excellent properties, metal halide perovskites have drawbacks that negatively affect the PCE and stability of the perovskite solar cell devices. This study investigated all-inorganic halide perovskite, $CsPbI_3$, by employing the first-principle density functional theory (DFT) method. Firstly, the effect of mixing halides on X-site was investigated to probe the structural stability and opto-electronic properties. The structural, electronic, optical, mechanical and thermodynamics properties of $CsPbI_{3-x}Br_x$ were investigated using three exchange correlation functionals, namely, LDA, GGA-PBE and SCAN meta-GGA. The findings revealed that mixed halide perovskites have an ideal direct energy band gap for suitable photovoltaic applications. For GGA-PBE and SCAN meta GGA exchange correlation functionals, the determined energy band gap ranges from 1.33 eV and 1.877 eV, whereas the LDA band gap ranges between 0.960 eV and 1.137 eV. The electronic band gaps predicted by GGA-PBE and SCAN meta GGA exchange correlation, which offer better precision compared to LDA suggest that Br-doped $CsPbI_{3-x}Br_x$ perovskite is suitable for photons absorption from near-infrared to visible regions of the spectrum. The modification of the band gap is an essential feature of photovoltaics, as it enables the optimization of solar cell performance. In addition, the systems $CsPbI_3$, $CsPbI_2Br$, $CsPbIBr_2$, and $CsPbBr_3$ exhibited exceptional mechanical and thermodynamic stability.

Secondly, perovskites that are considered for photovoltaic applications contain toxic element lead (Pb) on the B-site, which limits application of these perovskites in photovoltaic devices. In this study, substitution of toxic Pb with a smaller percentage of selected transition metals was investigated in order to alleviate the toxicity problems. Thus, $CsPbI_3$ doped with 12.5 % concentration of transition metal, Mn, Fe, Ni and Zn was investigated using DFT. The results showed that transition metal doped-$CsPbI_3$ perovskites enhanced the absorption of this material, although they are all indirect band gaps semiconductors.

All the materials were found to be mechanically stable.

Lastly, cluster expansion which is a method that is capable of describing the concentration dependent thermodynamic properties of materials while maintaining DFT accuracy, was used to predict new $(CsPbI/Br)_3$ structures. The cluster expansion method generated 42 new stable $(CsPb)_xI_yBr_z$ (where x = 1 to 3 and y and z = 1 to 8) structures and these were ranked the meta-stable structures based on their formation enthalpies. Monte Carlo calculations showed that $CsPbI_{0.5}Br_{0.5}$ composition separates into different phases at 300K, but changes to homogeneous phase at 700 K, suggesting that a different phase of $CsPbI_3$ may exist at higher temperature. Among the 42 predicted structures, randomly selected structures around iodide rich, 50:50 and bromine rich sites were studied further by determining their electronic, optical, mechanical and thermodynamic properties using DFT. The materials possess similar properties as cubic Br doped $CsPbI_3$ perovskites. The mechanical properties of these compounds revealed that they are ductile in nature and mechanically stable. In summary, the thesis present a novel work on introduction of impurities into $CsPbI_3$ perovskite material as well as compositional engineering to alter its electronic and optical properties for solar cells application.

Contents

Acknowledgments **iii**

Abstract **xi**

List of Figures **xix**

List of Tables **xxiii**

1 Introduction **1**

1.1 Background 1
1.2 Problem Statement 3
1.3 Justification 4
1.4 Aim and Objectives 5
1.4.1 Aim 5
1.4.2 Objectives 5
1.5 Thesis Outline 6

2 Literature Review **7**

2.1 Perovskites 7
2.2 Classification of Halide Perovskites 9
2.2.1 Hybrid Organic-Inorganic ABX_3 Perovskites 9
2.2.1.1 Methylammonium Lead Halide Perovskites 9
2.2.1.2 Formamidinium Lead Halide ABX_3 Perovskites 10
2.2.2 All-Inorganic Perovskites 11
2.2.2.1 Cesium Lead Halide Perovskites 12
2.2.2.2 Rubidium Lead Halide Perovskites 13
2.2.2.3 Potassium Lead Halide Perovskites 14
2.3 Physical Properties of Perovskites 15
2.3.1 Absorption 15
2.3.2 Band Gap Tuneability 17
2.3.3 Carrier Recombination 18

2.3.4 Charge Transport . . . 19
2.3.5 Power Conversion Efficiency . . . 21
2.4 Operational Principle of Perovskite Solar Cells . . . 22
2.4.1 Hole Transport Layer . . . 24
2.4.2 Electron Transport Layer . . . 24
2.4.3 Active Layer Materials . . . 25
2.4.4 Transparent Conducting Oxide . . . 25
2.4.5 Back Contact Materials . . . 26
2.5 Current Performances of the Devices . . . 26
2.6 Doping and Halides Mixing as Mechanisms of Improving the Performance of Perovskites . . . 27
2.6.1 A-site Doping . . . 28
2.6.2 B-site Doping . . . 28
2.6.3 X-site Doping . . . 31

3 Theoretical Method **33**
3.1 Background . . . 33
3.2 Many-Body Problem and Schrödinger Equation . . . 34
3.3 Born-Oppenheimer Approximation . . . 36
3.4 Hartree-Fock Method . . . 37
3.5 Density Functional Theory . . . 39
3.5.1 Hohenberg-Kohn Theorems . . . 39
3.5.2 Kohn-Sham Equations . . . 41
3.6 Exchange and Correlation Approximation . . . 43
3.6.1 Local Density Approximation . . . 43
3.6.2 Generalized Gradient Approximation . . . 44
3.6.3 Meta-Generalized Gradient Approximation . . . 44
3.6.4 Hybrid Functionals . . . 45
3.6.5 DFT+U . . . 46
3.7 Plane Wave Pseudopotential Method . . . 47
3.7.1 Plane Wave Basis Sets . . . 47
3.7.2 Pseudopotentials . . . 48
3.7.3 K-point Sampling . . . 50
3.8 Cluster Expansion . . . 51
3.8.1 Theoretical Background . . . 51
3.8.2 UNiversal CLuster Expansion . . . 52
3.8.2.1 Genetic Algorithm . . . 53
3.8.2.2 Iterative Optimization of the Training Set . . . 54
3.8.2.3 Monte Carlo . . . 56

3.9 Calculated Properties . . . 57
3.9.1 Electronic Properties . . . 57
3.9.1.1 Band Structure . . . 57
3.9.1.2 Density of States . . . 58
3.9.1.3 Bond Population Analysis . . . 59
3.9.2 Optical Properties . . . 59
3.9.3 Elastic Properties . . . 61
3.9.4 Thermodynamic Properties . . . 65
3.10 Computer Codes . . . 66
3.10.1 VASP Code . . . 66
3.10.2 UNCLE Code . . . 66

4 Mixed Halide $CsPbI_{3-x}Br_x$ 69
4.1 Introduction . . . 69
4.2 Computational Details . . . 70
4.3 Structural Properties . . . 71
4.4 Electronic Properties . . . 73
4.4.1 Band Structure . . . 73
4.4.2 Density of States . . . 74
4.5 Optical Properties . . . 75
4.5.1 Dielectric Function . . . 75
4.5.2 Refractive Index . . . 78
4.5.3 Extinction Coefficient . . . 80
4.5.4 Reflectivity . . . 80
4.5.5 Absorption . . . 81
4.5.6 Conductivity . . . 83
4.6 Elastic Properties . . . 84
4.7 Thermodynamic Properties . . . 86
4.8 Summary . . . 92

5 Doping $CsPbI_3$ with Transition Metals (Mn, Fe, Ni and Zn) 93
5.1 Introduction . . . 93
5.2 Computational Method . . . 94
5.3 Structural Properties . . . 95
5.4 Electronic Properties . . . 97
5.4.1 Band Structure . . . 97
5.4.2 Density of States . . . 99
5.5 Optical Properties . . . 101
5.5.1 Dielectric Function . . . 101

5.5.2 Refractive Index . . . 103
5.5.3 Extinction Coefficient . . . 104
5.5.4 Reflectivity . . . 105
5.5.5 Conductivity . . . 106
5.5.6 Absorption . . . 107
5.6 Elastic Properties . . . 108
5.7 Thermodynamic Properties . . . 110
5.8 Summary . . . 113

6 Prediction of Mixed Halides $CsPb(I/Br)_3$ Structures 115
6.1 Introduction . . . 115
6.2 Computational Methodology . . . 116
6.2.1 Cluster Expansion . . . 116
6.2.2 Monte Carlo . . . 117
6.2.3 Geometry Optimization . . . 117
6.3 Ground States Search . . . 117
6.3.1 Miscibility Gap . . . 121
6.4 Monte-Carlo . . . 121
6.5 Structural Properties . . . 125
6.6 Electronic Properties . . . 127
6.6.1 Band Structure . . . 127
6.6.2 Density of States . . . 129
6.7 Optical Properties . . . 131
6.7.1 Dielectric Function . . . 131
6.7.2 Refractive Index . . . 132
6.7.3 Extinction Coefficient . . . 133
6.7.4 Reflectivity . . . 134
6.7.5 Absorption . . . 135
6.7.6 Conductivity . . . 136
6.8 Elastic Properties . . . 137
6.9 Thermodynamic Properties . . . 139
6.10 Summary . . . 140

7 Conclusion and Future Work 143
7.1 Conclusion . . . 143
7.2 Future Work . . . 145

A Appendix 147

References 151

List of Publications **169**

List of Figures

2.1 Cubic crystal structure of perovskite ABX_3 [19]. 8
2.2 Schematic illustration of crystalline structure of $CsPbI_3$ and its polymorphic phase transition [37]. 13
2.3 (a) The tolerance factor and different melting temperature of $CsPbI_3$ ()and $RbPbI_3$ perovskites [46]. 14
2.4 Optical absorption coefficient comparison for $CH_3NH_3PbI_3$, $CsSnI_3$ and GaAs solar cell materials [52]. 16
2.5 The solar radiation spectrum versus wavelength [38]. 17
2.6 Device architecture of (a) n-i-p and (b) the charge transport process type PSCs, (c) p-i-n with (d) charge transport process in p-i-n type PSCs. . . . 21
2.7 Efficiency graph for silicon, perovskite, and tandem silicon-perovskite devices during the past ten years. Information extracted from the US NREL's efficiency graph [65]. 22
2.8 An illustration of perovskite solar cell layers [66]. 23
2.9 Different doping elements and their functions in tailoring lead halide perovskites [85]. 27

3.1 Pseudopotentials and pseudo wavefunctions [131]. 49
3.2 Illustration of genetic algorithm approach [139]. 54
3.3 Binary groundstate diagram illustrating miscible constituent [139]. 55
3.4 Binary groundstate diagram illustrating miscibility gap [139]. 56

4.1 The constructed cubic polyhedron crystal structure of $CsPbI_3$. The perovskites $CsPbI_2Br$, $CsPbIBr_2$, and $CsPbBr_3$ were constructed by replacing the I^- ion with the Br^- ion. 71
4.2 Band structures of (a) $CsPbI_3$, (b) $CsPbI_2Br$, (c) $CsPbIBr_2$ and (d) $CsPbBr_3$ perovskites obtained using three functionals. 74
4.3 Total and partial density of states for (a) $CsPbI_3$, (b) $CsPbI_2Br$, (c) $CsPbIBr_2$ and (d) $CsPbBr_3$ perovskites obtained using SCAN meta-GGA. 76

4.4 Calculated real part $\varepsilon_1(\omega)$ of (a) $CsPbI_3$, (b) $CsPbI_2Br$, (c) $CsPbIBr_2$ and (d) $CsPbBr_3$ compounds obtained using LDA, GGA-PBE and SCAN meta-GGA. 77
4.5 Calculated imaginary dielectric function $\varepsilon_2(\omega)$ of (a) $CsPbI_3$, (b) $CsPbI_2Br$, (c) $CsPbIBr_2$ and (d) $CsPbBr_3$ compounds obtained using LDA, GGA-PBE and SCAN meta-GGA. 78
4.6 Calculated refractive index $n(\omega)$ of (a) $CsPbI_3$, (b) $CsPbI_2Br$, (c) $CsPbIBr_2$ and (d) $CsPbBr_3$ compounds obtained using LDA, GGA-PBE and SCAN meta-GGA. 79
4.7 Calculated extinction coefficient $K(\omega)$ of (a) $CsPbI_3$, (b) $CsPbI_2Br$, (c) $CsPbIBr_2$ and (d) $CsPbBr_3$ compounds obtained using LDA, GGA-PBE and SCAN meta-GGA. 80
4.8 Calculated reflectivity $R(\omega)$ of (a) $CsPbI_3$, (b) $CsPbI_2Br$, (c) $CsPbIBr_2$ and (d) $CsPbBr_3$ compounds obtained using LDA, GGA-PBE and SCAN meta-GGA. 81
4.9 Calculated absorption coefficient $\alpha(\omega)$ of (a) $CsPbI_3$, (b) $CsPbI_2Br$, (c) $CsPbIBr_2$ and (d) $CsPbBr_3$ compounds obtained using LDA, GGA-PBE and SCAN meta-GGA. 82
4.10 Calculated optical conductivity $\sigma(\omega)$ of (a) $CsPbI_3$, (b) $CsPbI_2Br$, (c) $CsPbIBr_2$ and (d) $CsPbBr_3$ compounds obtained using LDA, GGA-PBE and SCAN meta-GGA. 84
4.11 Temperature dependence of heat capacity of (a) $CsPbI_3$, (b) $CsPbI_2Br$, (c) $CsPbBr_2I$ and (d) $CsPbBr_3$ perovskites obtained using GGA-PBE and LDA the functionals. 88
4.12 Temperature dependence of thermodynamic properties, that is, enthalpy, temperature entropy, and free energy of (a) $CsPbI_3$, (b) $CsPbI_2Br$, (c) $CsPbBr_2I$ and (d) $CsPbBr_3$ perovskites obtained using GGA-PBE. 89
4.13 Temperature dependence of heat capacity of (a) $CsPbI_3$, (b) $CsPbI_2Br$ and (c) $CsPbBr_3$ perovskites and their (d) - (e) enthalpy, temperature entropy, and free energy using SCAN functional. 90
4.14 Temperature dependence of heat capacity of (a) $CsPbI_3$, (b) $CsPbI_2Br$, (c) $CsPbIBr_2$ and (d) $CsPbBr_3$ perovskites and their (e) - (h) enthalpy, temperature entropy, and free energy using LDA functional. 91

5.1 The constructed polyhedron unit cell (left) and supercell cubic perovskite crystal structure with A-cation (blue), B-cation (grey) and X-anions (magenta). 95
5.2 Electronic band structure of the (a) Mn-doped $CsPbI_3$, (b) Fe-doped $CsPbI_3$, (c) Ni-doped $CsPbI_3$, and (d) Zn-doped $CsPbI_3$ perovskites. 99

5.3 Total and partial DOS for undoped $CsPbI_3$ perovskite. 100
5.4 Total and partial density of states for (a) $CsPb_{0.875}Mn_{0.125}I_3$, (b) $CsPb_{0.875}Fe_{0.125}I_3$, (c) $CsPb_{0.875}Ni_{0.125}I_3$, and (d) $CsPb_{0.875}Zn_{0.125}I_3$ perovskite materials. . . 101
5.5 The calculated real part of the dielectric function, $\varepsilon_1(\omega)$ for undoped $CsPbI_3$ and TM doped perovskites. 102
5.6 The calculated imaginary part of the dielectric function, $\varepsilon_2(\omega)$ for undoped $CsPbI_3$ and TM doped perovskites. 103
5.7 The calculated refractive index, $n(\omega)$ for the undoped $CsPbI_3$ and TM doped perovskites. 104
5.8 The calculated extinction coefficient of undoped $CsPbI_3$ and TM doped perovskites 105
5.9 The calculated reflectivity, $R(\omega)$ of undoped $CsPbI_3$ and TM doped perovskites. 106
5.10 The calculated conductivity, $\sigma(\omega)$ of undoped $CsPbI_3$ and TM doped perovskites using GGA-PBE functional. 107
5.11 The calculated optical absorption coefficient, $\alpha(\omega)$ of the undoped $CsPbI_3$ and TM doped perovskites. 108
5.12 The calculated heat capacity, enthalpy, entropy and free energy against temperature for $CsPbI_3$ perovskite. 112
5.13 The calculated heat capacity against temperature for $CsPb_{0.875}TM_{0.125}I_3$ perovskite materials. 112
5.14 The calculated enthalpy, entropy and free energy against temperature for $CsPb_{0.875}TM_{0.125}I_3$ perovskite materials. 113

6.1 Ground state diagram of $CsPb(IBr)_3$. 119
6.2 Temperature profile cross section through 25x25x25 Monte Carlo simulation for $CsPb(IBr)_3$. 123
6.3 Monte Carlo simulation cells of $CsPbI_{0.5}Br_{0.5}$ at different temperature. Blue and orange balls are I and Br atoms. 124
6.4 The cluster expansion predicted structure $Cs_2Pb_2I_3Br_3$, $Cs_2Pb_2I_5Br$ and $Cs_3Pb_3IBr_8$. 126
6.5 The calculated band structures of the predicted (a) $Cs_2Pb_2I_3Br_3$, (b) $Cs_2Pb_2I_5Br$ and (c) $Cs_3Pb_3IBr_8$ structures. 128
6.6 The calculated total and partial density of states for the predicted structures (a) $Cs_2Pb_2I_3Br_3$, (b) $Cs_2Pb_2I_5Br$ and (c) $Cs_3Pb_3IBr_8$. 130
6.7 The calculated real $\varepsilon_1(\omega)$ dielectric function of the predicted structures (a) $Cs_2Pb_2I_3Br_3$, (b) $Cs_2Pb_2I_5Br$ and (c) $Cs_3Pb_3IBr_8$. 131
6.8 The calculated imaginary $\varepsilon_2(\omega)$ dielectric function of the predicted structures (a) $Cs_2Pb_2I_3Br_3$, (b) $Cs_2Pb_2I_5Br$ and (c) $Cs_3Pb_3IBr_8$. 132

6.9 The calculated refractive index $n(\omega)$ of the predicted structures (a) $Cs_2Pb_2I_3Br_3$, (b) $Cs_2Pb_2I_5Br$ and (c) $Cs_3Pb_3IBr_8$. 133
6.10 The calculated extinction coefficient $k(\omega)$ of the predicted structures (a) $Cs_2Pb_2I_3Br_3$, (b) $Cs_2Pb_2I_5Br$ and (c) $Cs_3Pb_3IBr_8$. 134
6.11 Calculated reflectivity $R(\omega)$ of predicted structures(a) $Cs_2Pb_2I_3Br_3$, (b) $Cs_2Pb_2I_5Br$ and (c) $Cs_3Pb_3IBr_8$. 135
6.12 The optical absorption coefficient $\alpha(\omega)$ of the predicted structures (a) $Cs_2Pb_2I_3Br_3$, (b) $Cs_2Pb_2I_5Br$ and (c) $Cs_3Pb_3IBr_8$. 136
6.13 The optical conductivity $\sigma(\omega)$ of the predicted structures (a) $Cs_2Pb_2I_3Br_3$, (b) $Cs_2Pb_2I_5Br$ and (c) $Cs_3Pb_3IBr_8$. 137
6.14 Temperature dependence of heat capacity of (a) $Cs_2Pb_2I_3Br_3$, (b) $Cs_2Pb_2I_5Br$ and (c) $Cs_3Pb_3IBr_8$ perovskites and their (d) - (e) enthalpy, temperature entropy, and free energy. 140

A.1 Total and partial density of states for (a) $CsPbI_3$, (b) $CsPbI_2Br$, (c) $CsPbIBr_2$ and (d) $CsPbBr_3$ perovskites using GGA. 148
A.2 Total and partial density of states for (a) $CsPbI_3$, (b) $CsPbI_2Br$, (c) $CsPbIBr_2$ and (d) $CsPbBr_3$ perovskites using LDA. 149

List of Tables

2.1 Tolerance factor merit used to define the type of ABX_3 structure [25]. . . 9

4.1 Calculated lattice constant, unit cell volume and energy band gap for $CsPbI_3$, $CsPbI_2Br$, $CsPbIBr_2$, and $CsPbBr_3$ compounds obtained using three functionals compared with experimental and other calculated theoretical values. 72
4.2 The calculated static refractive index n(0), and n(max) of $CsPbI_3$, $CsPbI_2Br$, $CsPbIBr_2$ and $CsPbBr_3$ compounds obtained using three functionals. . . . 79
4.3 Calculated elastic constants and energy Cauchy pressure for $CsPbI_3$, $CsPbI_2Br$, $CsPbIBr_2$, and $CsPbBr_3$ compounds obtained using three functionals compared with experimental and other calculated theoretical values. 85
4.4 Calculated elastic constants and energy Cauchy pressure for $CsPbI_3$, $CsPbI_2Br$, $CsPbIBr_2$, and $CsPbBr_3$ compounds obtained using the three functionals. 86
4.5 Calculated average sound velocities (v_s) and Debye temperature (θ_D), obtained using the three functionals. 87

5.1 The computed structural parameters, angle, and bond length for transition metal doped $CsPbI_3$ perovskites are compared with experimental and theoretical values. 97
5.2 The calculated elastic contants C_{ij}, and Caunchy pressure of an undoped and TM doped $CsPbI_3$. 109
5.3 The calculated bulk modulus, shear modulus, Young's moduli, Pugh's ratio and Poisson for $CsPbI_3$ and TM doped perovskites 109
5.4 The computed average sound velocity v_s, Debye temperature θ_D, and melting temperature for undoped $CsPbI_3$ and $CsPb_{0.875}TM_{0.125}I_3$ perovskites. 111

6.1 Cluster expansion structural predicted structures $(CsPb)_xI_yBr_z$ (where x = 1 to 3 and y and z = 1 to 8) for binary system at various composition. . . . 120
6.2 The development of an iterative procedure that lists stable structures constructed of numerous pure phases. 121
6.3 The calculated structural parameters, angle and bond length of (a) $Cs_2Pb_2I_3Br_3$, (b) $Cs_3Pb_3IBr_8$ and (c) $Cs_2Pb_2I_5Br$. 126

6.4 The calculated elastic constants C_{ij} of (a) $Cs_2Pb_2I_3Br_3$, (b) $Cs_2Pb_2I_5Br$ and (c) $Cs_3Pb_3IBr_8$. 138
6.5 The calculated bulk, shear, Young's moduli, Pugh's and Poisson ratio of (a) $Cs_2Pb_2I_3Br_3$, (b) $Cs_2Pb_2I_5Br$ and (c) $Cs_3Pb_3IBr_8$. 139

1

Introduction

1.1 Background

The depletion of non-renewable resources and rapid advancement in technology have encouraged researchers to find alternative energy sources, particularly renewable energy sources that show promise to supply power in homes and industries. Various options like solar power, wind energy, nuclear power, and biomass can be utilized as alternative sources for energy supply [1]. Among all these sources, solar energy is considered a more environmentally friendly mode of alternative energy supply and most countries are investing in solar energy research and development [1, 2]. Photovoltaic devices (commonly known as solar panels) are mooted as promising candidates for a "green" source of electricity and thus leaving a zero-carbon footprint while providing alternative ways to meeting the ever-

increasing energy demand.

Photovoltaic (PV) devices that convert sunlight into energy are known as solar cells [3]. Currently, there are three generations of solar cells, each distinguished by the materials used. First-generation solar cells are composed of poly or mono-crystalline silicon. Materials including cadmium telluride (CdTe), copper indium gallium selenide (CIGS), and amorphous silicon (a-Si) are used in the construction of second generation solar cells. Lastly, third-generation solar cells incorporate organometallic and inorganic compounds, specifically perovskites. For the purpose of this study, perovskite solar cell materials are discussed.

Perovskites solar cells (PSCs) are solar cells that utilize materials with perovskite crystal structure. The perovskite compounds are predominantly organic-inorganic hybrid halide perovskites, with a specific chemical composition. These materials have ABX_3 crystal structure, wherein A is monovalent cations such as methylammonium (MA) or formamidinium (FA) for organic perovskites or cesium (Cs^+), potassium (K^+), and rubidium (Rb^+) for inorganic perovskites, B is the divalent metal cation lead (Pb^{2+}) or tin (Sn^{2+}), and X is the halogen anion including iodine (I^-), bromine (Br^-), and chlorine (Cl^-). Perovskite materials serve as photo-active layers in solar cells [4]. Furthermore, these materials can easily convert to thin films and suitable crystal forms such as nanocrystalline, nanoparticles, and nanowire for device applications [5]. These halide perovskites possess a great potential to be applied as high performing solar cells light harvesting materials due to their exceptional opto-electronic characteristics, like optical absorption coefficient that is significant for light harvesting, tuneable band gap, and their simple reproducible preparation process [6, 7]. In essence, the efficiency for PSCs has significantly been improved from 3.8 % to 25.5 % in the recent years [8–10]. Despite their excellent properties, the organic-inorganic halide perovskites have drawbacks that negatively impact the stability and efficiency of the PV device. Additionally, the stability of these hybrid perovskites may be compromised in real world application, especially when they are subjected to conditions such as heat, moisture, defects on the surface, and light. The presence of organic cations is the primary factor that contributes to this volatility in perovskites. However,

all-inorganic halide perovskites have demonstrated improved stability compared to their organic-inorganic counterparts. As a result, there has been increased research focus on enhancing the opto-electronic properties and stability of all-inorganic metal halides perovskites, which have attracted significant scrutiny in scientific community. Doping these perovskite materials either by mixing cations (A and B) or X-halides, the perovskites offer degree of compositional tunability, which leads to tunable band gap and improved materials stability. In this work, various compositional engineering schemes were employed to investigate the structural, electronic, mechanical, optical, and thermodynamic properties of doped $CsPbI_3$ using first principle methods.

1.2 Problem Statement

Organic and inorganic perovskite materials for solar cells have demonstrated potential as replacements for currently used photovoltaic technologies, because of exponential growth in their PCE. Despite significant advances in understanding the stability and degradation of PSCs, there are, however, several challenges to circumvent before they can be commercialized, and key challenges are highlighted below:

(i) **Toxicity**: The inclusion of the hazardous element lead (Pb) in high-performance perovskite solar cells is indeed of an environmental and public health concern. Despite the relatively small amount of Pb used in these cells, its toxic nature poses limitations on the application spectrum and can potentially affect the competitive advantage of perovskite solar cells. Replacing toxic Pb with eco-friendly and non-toxic materials that have the same electronic configuration (for example germanuim (Ge) and tin (Sn)) for solar cells applications has been considered to alleviate the problem of toxicity.

(ii) **Stability**: Apart from improving the efficiency, stability is one major problem for PSCs, especially when exposed to environmental conditions like elevated temperature, moisture and under UV light, as well as with encapsulation. The presence of organic cations, including FA^+ and MA^+, makes them susceptible to decomposition at higher temperatures, consequently affecting the overall device stability [11]. Inorganic perovskites

generally demonstrate higher stability than organic counterparts. As a result, the incorporation of inorganic cations in place of the organic component (for example, Cs^{2+}, Rb^{2+}, etc.) in perovskites can drastically improve the thermal stability and ultimately the general performance of the PCS devices [12, 13]. Incorporation of both organic FA^{+} and inorganic Cs^{+} has demonstrated an enhanced moisture retention and thermal stability, and also the materials have been found to be stable when operating in the presence of oxygen [14]. All inorganic perovskite materials are considered to have the ability to contribute to a long-term, economically viable solution for large-scale power generation by utilizing ecologically acceptable materials [15].

(iii) **Efficiency penalty**: The PCE of 13.21 % has been reported when using $CsPbI_3$ PSC with an energy band gap of 1.7 eV for solar cell application. However, the main challenge with all inorganic perovskites especially, $CsPbX_3$ (where X = F, Cl, Br, and I) that have a narrow band gap is the thermodynamic instability of their phases, which means that the preferred cubic, α phase (i.e., "black phase") of the material undergoes an unwanted phase transition to the orthorhombic, δ phase (i.e., "yellow phase"), which at ambient temperature is thermodynamically stable. This spontaneous phase transition currently poses limitation on the development of high-performance all-inorganic $CsPbI_3$ PSCs [16]. Additionally, recent reports have brought attention to the issue of self-degradation of iodine, which can potentially reduce the lifespan of iodine-containing perovskite materials [17]. Therefore, this study uses halide substitution and doping mechanisms employing first-principle calculations to probe properties of doped $CsPbI_3$ perovskite in order to understand and circumvent both stability and toxicity issues.

1.3 Justification

Scientific efforts are being made for renewable energy sources with the intention of utilizing alternate sources of energy to avert a potential global energy catastrophe. All inorganic mixed halide perovskites have the potential in improving the photovoltaic properties by increasing the stability and efficiency of the solar cell devices. Also, addition of other met-

als and Br to $CsPbI_3$ is expected to modify the band gap, resulting in the enlargement of the energy band gap. Replacing lead by different elements will possibly lead to properties that suits the photovoltaic application such as Goldsmiths tolerance and some additional opto-electrical properties. Essentially, inorganic halide perovskites have the potential to revolutionize solar cell technology.

1.4 Aim and Objectives

1.4.1 Aim

This investigation aims to use first-principle calculations or simulations to study the properties such as structural, electronic, optical, mechanical and thermodynamic of doped $CsPbI_3$ for potential photovoltaic applications.

1.4.2 Objectives

The specific objectives of this work were to:

(i) investigate the structural, electronic, optical, mechanical, and thermodynamic properties of $CsPbI_3$ polymorphs using different exchange correlation functions LDA, GGA, and SCAN meta-GGA in density functional theory to understand their chemical and thermal stability.

(ii) carry out systematic investigation of mixed halide $CsPbI_{3-x}Br_x$ using the above mentioned exchange correlation functionals to engineer the band gap and other opto-electronic properties.

(iii) investigate the effect of doping $CsPbI_3$ perovskite with transition metal, Mn^{2+}, Fe^{2+}, Ni^{2+} and Zn^{2+} and calculate their structural, electronic, optical, mechanical, and thermodynamic properties employing GGA+U functional for strong Coulomb forces in transitional metals.

(iv) apply cluster expansion method to investigate concentration dependent thermodynamic properties of mixed halides $CsPbI_3$ perovskite and predict new ($CsPbI_xBr_{1-x}$) structures.

(v) calculate structural, opto-electronic, elastic, and thermodynamic properties of selected

new $CsPb(I/Br)_3$ structures to determine their stability and opto-electronic characteristics.

1.5 Thesis Outline

The research reported in the thesis is organized into seven chapters, as outlined below:

Chapter 2 - presents a general overview of the research work, providing the background theory and a comprehensive literature review related to the study. This review includes an introduction to perovskite materials, their classifications, physical properties, and operational principles.

Chapter 3 - provides the theoretical methods utilized in this study. It focuses on computational techniques, particularly density functional theory and cluster expansion methods.

Chapter 4 - focuses on the structural, opto-electronic, elastic, and thermodynamic properties of $CsPbI_3$ perovskite material doped with bromine. The GGA-PBE, SCAN, and LDA functionals were used in the analysis.

Chapter 5 - focuses on the structural, electronic, optical, mechanical and thermodynamic properties of $CsPbI_3$ perovskite material doped with transition metals. It explores the effect of doping with transition metal (Mn^{2+}, Fe^{2+}, Ni^{2+} and Zn^{2+}), including that of the Hubbard parameter on the properties of the $CsPbI_3$ material.

Chapter 6 - focuses on the analysis of a binary diagram to identify new stable configurations using cluster expansion method. After identifying these stable configurations, calculations of their structural, electronic, optical, and thermodynamics properties employing DFT are presented. These calculations serve to verify the stability of the identified configurations by examining their response to mechanical stress, and their electronic behavior. This comprehensive analysis helps ensure the reliability and stability of the newly generated configurations within the binary diagram.

Chapter 7 - provides a general conclusion of the thesis, summarizing the findings and their implications in solar cell applications.

2

Literature Review

2.1 Perovskites

Perovskite was discovered for the first time by mineralogist Gustav Rose as a natural mineral called calcium titanium oxide ($CaTiO_3$) and was named after the Russian mineral scientist Perovski [18]. All perovskite materials adopt the structure depicted in Figure 2.1 and their general chemical formula is ABX_3, where A represents a large cation (whether atoms or molecules), B represents small cation, and X represents an anion and, normally could be oxygen or halogen. They are broadly classified into two groups, namely; halide perovskites (ABX_3) and metal oxide perovskites (ABO_3).

The halide perovskite crystal structure is a cubic unit cell, with a lattice parameter a = b = c as illustrated in Figure 2.1 [19]. The unit cell contains eight corner atoms of X

ions, which form a cube, and one A ion at the center. The B-ions are found at the centre of each face of the cube. This arrangement of ions creates a three-dimensional network of corner-sharing BX_6 octahedral, connected by shared faces to form a continuous framework [12].

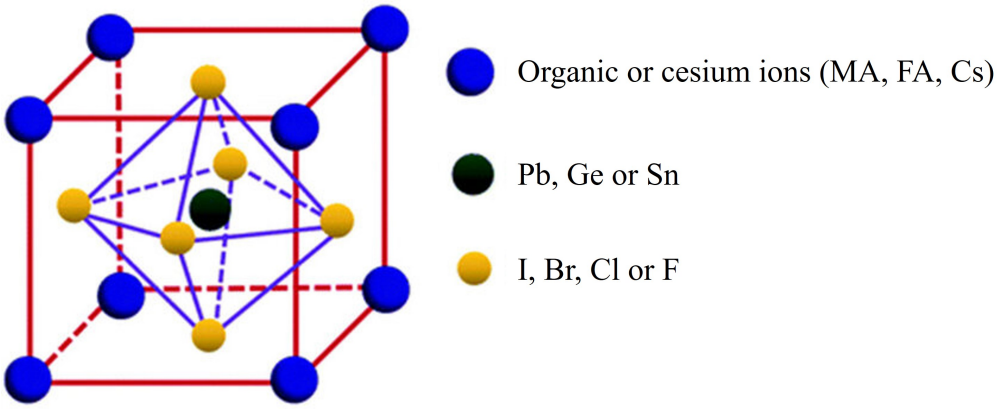


Figure 2.1: Cubic crystal structure of perovskite ABX_3 [19].

Perovskite materials are archetypal systems, and the cubic structure can tilt or distort to form mono-clinic, tetragonal, and orthorhombic polymorphs based on the temperature or pressure [20, 21]. The distortion and stability of perovskite materials are determined by X, B, and A atomic radii. The Goldschmidt tolerance factor, also known as the Goldschmidt constant, is a dimensionless parameter made used to predict the chemical stability of a perovskite materials. It was initially proposed by a German mineralogist Viktor Goldschmidt in the 1920s. It is calculated by dividing the geometric mean of cations (A and B) ionic radii by the geometric mean of an anion (X and Y), ionic radii occupy the center of the cubic unit cell. Goldschmidt's tolerance factor denoted by t is an important parameter to determine perfect perovskite crystal structure and together with the octahedral factor (μ) [22, 23] and is described as:

$$t = \frac{r_A + r_X}{\sqrt{2}(r_B + r_X)} \tag{2.1}$$

where r_A and r_B are the radii of cations A and B, respectively; and r_X represents the radius of anion X. There is a probability that the perovskite crystal structure will develop or form when the t ranges between 0.71 and 1 [24]. Additionally, it is feasible to determine the phase created by considering the values of t; Table 2.1 details this relationship [25].

Table 2.1: Tolerance factor merit used to define the type of ABX_3 structure [25].

Value of t	Phase	Notes
> 1	Single chained, hexagonal or tetragonal	A is very large or B is very small
0.8 - 1	Cubic	Ideal size A and B radii
0.71 - 0.8	Rhombohedral or orthorhombic	A is very small
< 0.71	Non-perovskite	radius of A or B are similar

2.2 Classification of Halide Perovskites

Halide perovskites can be grouped into two classes based on chemical composition, namely; hybrid or organic perovskites and conventional or inorganic perovskites. The two types are discussed briefly in the next subsections.

2.2.1 Hybrid Organic-Inorganic ABX_3 Perovskites

2.2.1.1 Methylammonium Lead Halide Perovskites

The methylammonium lead iodide ($MAPbI_3$) perovskite was first discovered by Weber in 1978 [26] and has been extensively studied in solar cell technology because of its remarkable photovoltaic characteristics. Weber created the first three dimensional organic-inorganic hybrid perovskite by replacing Cs^+ with MA^+.

$MAPbI_3$ as an absorber material for PV applications, has good properties including a direct energy band gap values from 1.55 - 1.6 eV, a high absorption coefficient $10^4 - 10^5$ cm^{-1} and a strong light absorption throughout the visible region of the spectrum [11]. In addition, it has a low exciton binding energy of approximately 16 me$V$ at ambient temperature, which allows it to dissociate quickly into separate electrons and holes. It also has moderate electron mobility, with a value of 10 $cm^2V^{-1}s^{-1}$ for $MAPbI_3$ [7], that is processed through solution mixing and high carrier diffusion lengths, which can reach as far as 175 μm in mono-crystals under direct sunlight and between 100 nm - 1000 nm when is used in thin films [27]. These characteristics suggest that $MAPbI_3$ has long recombination times, in the hundreds of nanoseconds range. However, $MAPbI_3$ stability has been found

to significantly vary depending on temperature, crystal orientation or changing phase. The instability is mainly attributed to the existence of the organic cation methylammonium that is prone to decomposition and volatilization. Numerous ways have been proposed as a way to improve the chemical stability of $MAPbI_3$, whose stability has been demonstrated under various environmental conditions.

2.2.1.2 Formamidinium Lead Halide ABX_3 Perovskites

The formamidinium lead halide $(HC(NH_2)_2)PbX_3$ (X = I, Br, Cl or F) materials are referred to as $FAPbI_3$ and these are perovskite materials that have also gained attention for photovoltaic applications. These materials are a subclass of hybrid organic-inorganic perovskites, meaning that they contain both organic and inorganic components. Both $MAPbI_3$ and $FAPbI_3$ are direct band gap semiconductor. These perovskites have a unique crystal structure with a distorted perovskite lattice, ascribed to comparatively large size of the formamidinium cation [28]. $FAPbX_3$ perovskites have emerged as promising alternatives methylammonium (MA) perovskites because of its longer charge diffusion length, improved photo-stability and lower band gap energy, which result in expanded light harvesting capabilities. This modification allows for the fine-tuning of the perovskite material's optical properties, making it more suitable for achieving desired energy conversion efficiencies in solar cells. Formamidinium lead halide perovskites have a high thermal, moisture and chemical stability compared to $MAPbI_3$ as well as all-inorganic K, Rb or Cs perovskites compounds [28–30]. These preferred properties make them favorable for use in photovoltaic solar cells. However, compared to MA perovskites, the technology for preparing thin films, microcrystalline powders or crystals are not well established because of the following:

(i) $FAPbI_3$ crystals or thin films that normally crystallize in the so called "yellow" non-perovskites phase [31, 32].

(ii) Ionic radius differences (MA^+ 2.17 $\AA$ and FA^+ 2.53 $\AA$) affecting the growth kinetics [33]. Previous research has demonstrated that the energy band gap can be engineered from 1.55 and 2.30 eV in this material by varying the concentration of iodide to bromide, allow-

ing for color variation and optimization for use in multi-junction solar cells [34].

2.2.2 All-Inorganic Perovskites

Inorganic perovskites have come out as prominent materials for photovoltaic applications because of their stability, ability to achieve competitive power conversion efficiencies, and low production costs, making them economically important for large-scale production and incorporation in photovoltaic devices. Here are a few concepts that are being researched to improve the overall performance of all-inorganic PSC materials:

Passivation: The use of surface treatment techniques to reduce charge carrier recombination of the perovskite-electrode junction, which increases the power conversion efficiency of photovoltaic devices.

Doping: Introducing impurities into the perovskite material to tailor its electronic properties and increase the conductivity of the material.

Stabilization: Improving the structural and chemical stability of these material for degradation reduction over time and enhancing long-term performance of the solar cell devices.

Interfacial engineering: Developing new materials and interfaces for efficiency improvement of charge transfer across the electrodes and perovskite material.

Morphology control: Using techniques such as solution processing to control the shape, size, and orientation of ABX_3 crystal structures to enhance the solar cell's performance.

Compositional engineering: Exploring new perovskite compositions to optimize opto-electronic properties of the material for photovoltaic applications.

Temperature treatments: Exploring the use of post-synthesis thermal treatments to enhance the crystallinity, morphology, and opto-electronic properties of the perovskite materials.

Hybrid perovskites: Combining inorganic perovskites with other materials to improve their properties, including the energy band gap, efficiency and stability.

2.2.2.1 Cesium Lead Halide Perovskites

$CsPbX_3$ (X = Cl, Br, or I) perovskites were first discovered by Moller in 1958, 64 years later after discovery of organometal trihallide perovskites. Cesium lead halide perovskites are among mostly researched all-inorganic perovskite materials due to their prospective photovoltaic applications. Their broad absorption spectrum which covers the visible region and extends into the near-infrared wavelengths is one of their distinct characteristics. This feature can be attributed to the presence of cesium ions, which can absorb light over a wide range of wavelengths. Additionally, cesium lead halide perovskites have a high electron mobility and long carrier lifetime that can improve performance of the solar cells.

Numerous researchers have also become interested in the carrier mobility of three-dimensional structures. For example, Ying *et al*. detailed the hole and electron mobilities of 2820 and 430 $cm^2V^{-1}s^{-1}$, respectively, for cubic $CsPbI_3$ [35]. Jong *et al.* reported that the charge mobilities of $CsGeI_3$, $CsGeBr_3$ and $CsGeCl_3$ were 1677, 1401 and 863 $cm^2V^{-1}s^{-1}$ at 300 K temperature, respectively [36]. Another advantage of $CsPbI_3$ have higher stability compared to $MAPbI_3$ and $FAPbI_3$ as cesium oxidation state can help to reduce their degradation over time and stabilize ABX_3 perovskite structure. This makes cesium lead halide perovskites more suitable for use in long-term applications such as solar energy conversion. The two main factors affecting the phase stability of $CsPbX_3$ are thought to be large crystal distortion and low tolerance factor.

Even though the underlying transition mechanism responsible for the acceleration of the phase change from α to δ $CsPbI_3$ is not fully understood, moisture plays a pivotal part in the phase change. This may be due to the intermediate states created by water molecules and $CsPbI_3$ [24, 37]. The phase change phenomenon is demonstrated in Figure 2.2. The phase change energy barrier from cubic to orthorhombic-$CsPbI_3$ may be lowered by intermediate states, and the water molecules released by the degradation products could the accelerate conversion of additional α- into δ-$CsPbI_3$ phase. Therefore, when exposed to external conditions $CsPbI_3$ has stability issues [38, 39] requiring quantum dot–induced phase stabilization [40] and mixed halides are found to have improved stability. According to some experimental findings, $CsPbBr_3$ [41], $CsPbI_2Br$ [38], and $CsPbIBr_2$ [42, 43]

all exhibited exceptional stability when exposed to light, high temperature till 300 °C and moisture. Therefore, these all-inorganic mixed halides may offer the best chance of overcoming their inherent instability. Hence, this study investigates mixed halides $CsPbI_{3-x}Br_x$ and transition metals doped $CsPbI_3$ to further understand their stability.

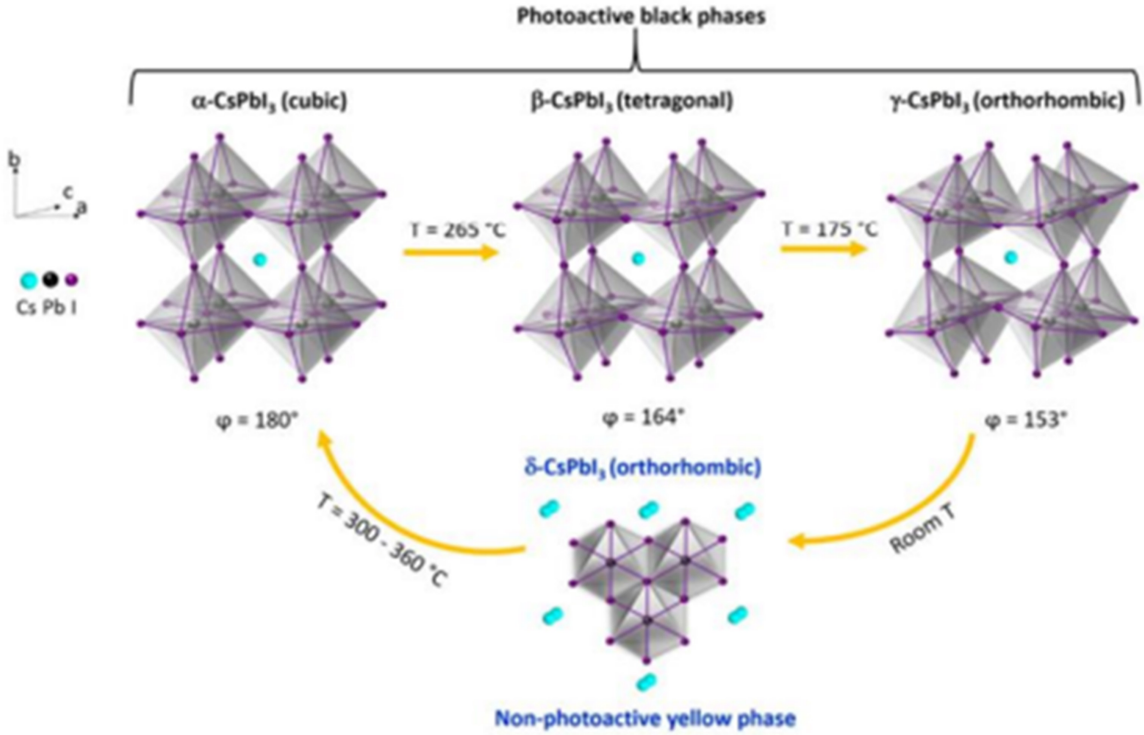


Figure 2.2: Schematic illustration of crystalline structure of $CsPbI_3$ and its polymorphic phase transition [37].

2.2.2.2 Rubidium Lead Halide Perovskites

Another option for the A cation to be considered for all-inorganic perovskites of the form ABX_3 is rubidium (Rb), the neighboring alkali element of cesium. More importantly, the $RbPbBr_3$ perovskite may have novel optoelectronic properties and help in understanding the relationship between the perovskite family's structure and properties [44]. Cesium (1.76 Å) has a larger ionic radius compared to rubidium (1.52 Å) with the tolerance factor of 0.81 and 0.77 respectively, as shown in Figure 2.3 (a) [45]. However, these two materials ($RbPbI_3$ and $CsPbI_3$) draw the boundary between photo-inactive yellow non-perovskite phase and photo-active black perovskite phase, demonstrating that even a small difference can have a significant effect. Trots *et al*. reported that $RbPbI_3$ and $CsPbI_3$ start melting

irreversibly at 460°C as demonstrated in Figure 2.3 (b). The $RbPbI_3$ phase does not show a black phase at high temperatures [46].

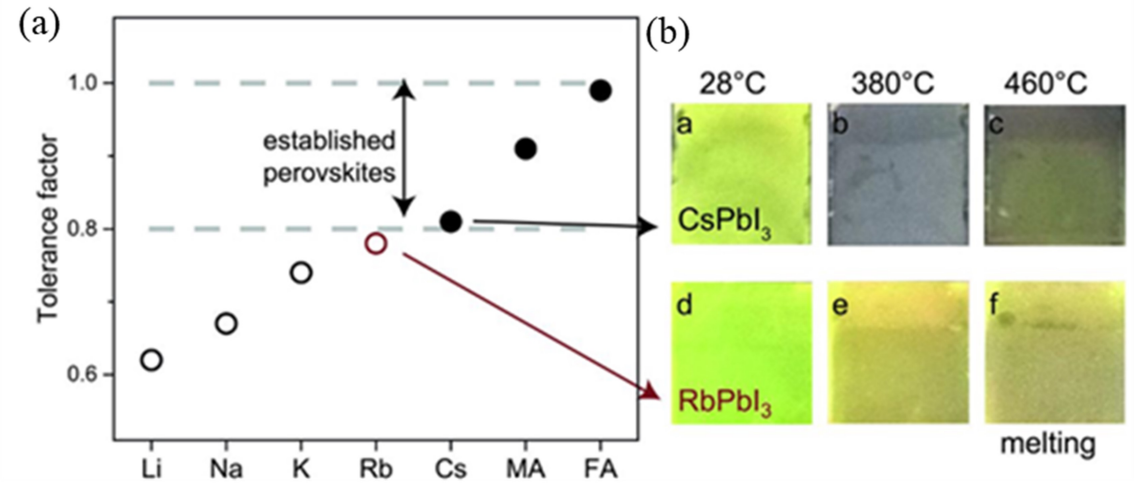


Figure 2.3: (a) The tolerance factor and different melting temperature of $CsPbI_3$ ()and $RbPbI_3$ perovskites [46].

2.2.2.3 Potassium Lead Halide Perovskites

Potassium is another element that has been explored as a potential candidate to replace Cs, however, there has been not much work reported on $KPbX_3$. Pitriana *et al.* reported on alkali lead iodide $APbI_3$ (where A=Cs,Li, K, Na or Rb), investigating their electronic properties using the first-principles calculations [47]. Their findings demonstrated that the presence of the alkali metal atoms (A) within the crystal structure has a minimal effect on the semiconducting characteristics of these inorganic perovskites, which include a small and direct band gap. Furthermore, potassium incorporation cations into the perovskite improves the stability of the material while reducing the formation of lead halide defects. Some researchers hypothesized that the improvement observed after the addition of K^+ was due to the reduction of trapping defects at the material electrode interface as well as the suppression of ion migration [48, 49].

Nam *et al.* studied compositional engineering strategy to change $CsPbI_3$ compounds by adding potassium cations [50]. This approach was motivated by previous research on hybrid perovskites, which demonstrated that partially substituting the A-site cation in ABX_3 perovskites with smaller cations can yield advantageous properties. The incorporation of K

cation into $CsPbI_3$ perovskites resulted in the reduction of the perovskite's volume, which is because cesium (1.76 Å) has a bigger ionic radius than potassium (1.38 Å). The ratio of PbX_6 octahedra (where X represents iodine or bromine) to A-site cations determines phase stability of these perovskites.

The shifts in binding energy peaks of the X-ray photoelectron spectroscopy spectra confirm that increasing the cationic charge of Pb and the confinement of the halide lattice is enhanced, resulting in a shrinkage of the PbX_6 octahedral volume. This is advantageous because the A-site cations effectively anchor the corner-shared PbX_6 octahedra, thereby improving the overall phase stability. These results highlighted the important role of compositional engineering and that of the A-site cations in modifying the structural and stability of $CsPbI_3$ perovskite.

2.3 Physical Properties of Perovskites

2.3.1 Absorption

Light absorption is the phenomenon in which a material absorbs light, resulting in the excitation of electrons to higher energy levels. PSCs are known for their high absorption coefficients, allowing them to efficiently absorb light across the spectrum range especially having Pb^{2+} and halide ions which may absorb light over a broad range of the spectrum wavelengths [51]. As shown in Figure 2.4, perovskites have a greater absorption coefficient than gallium arsenide (GaAs) for the wavelength 400 - 800 nm [52]. By modifying the perovskite structural composition, the absorption spectrum of PSC can also be modified. For example, by changing the halide ions, the absorption spectrum can be shifted to different regions of the electromagnetic spectrum. This is useful for optimizing the solar cell performance.

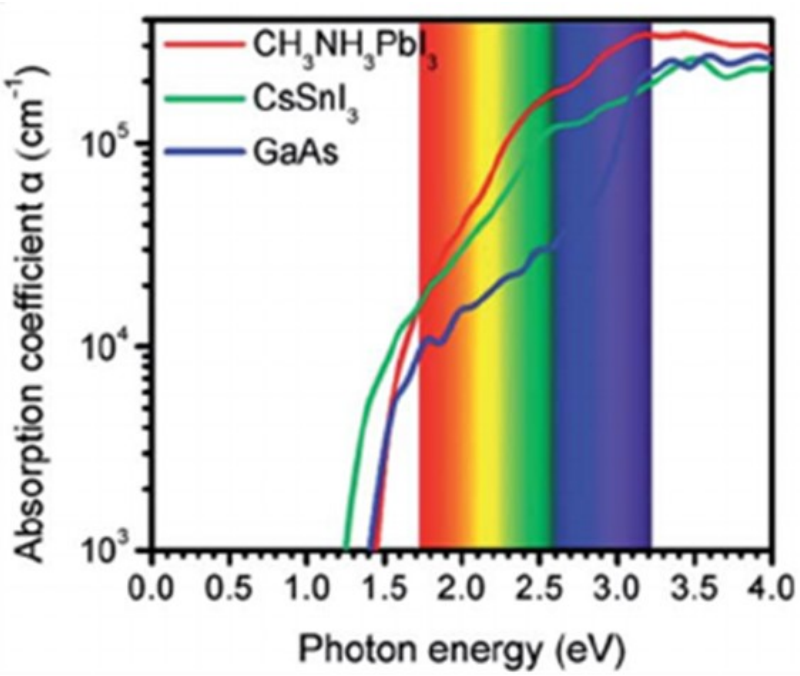


Figure 2.4: Optical absorption coefficient comparison for $CH_3NH_3PbI_3$, $CsSnI_3$ and GaAs solar cell materials [52].

To efficiently utilize solar energy through photocatalysis, understanding the solar spectrum is essential. Most solar radiation reaching the Earth's surface falls within the 300–2500 nm wavelength range, which includes UV light (<380 nm), visible light (380–780 nm, also known as sunlight), and near-infrared (NIR) light (>780 nm). As illustrated in Figure 2.5, the solar spectrum consists of 3-5 % UV light, 42-43 % visible light, and 52-55 % NIR light [38]. The irradiance at the Earth's surface is lower than at the top of the atmosphere due to scattering and absorption by gas molecules such as N_2, O_2, H_2O, and CO_2. The globally averaged solar irradiance is estimated to be approximately 1.365 kW per square meter over a 24-hour day throughout the year.

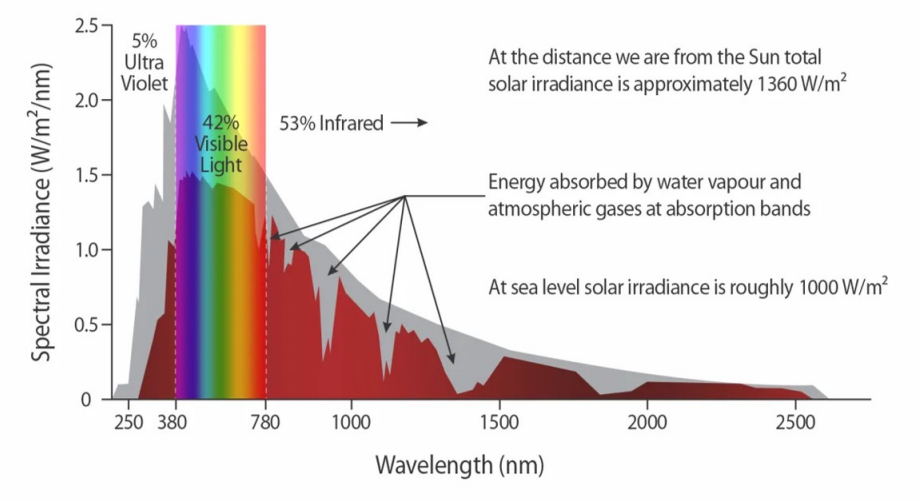


Figure 2.5: The solar radiation spectrum versus wavelength [38].

2.3.2 Band Gap Tuneability

In a material, the energy difference between the lowest unoccupied electron level (i.e., the conduction band) and the highest occupied electron level (i.e., the valence band) is known as the energy band gap. The energy band gap defines the optical and electronic properties of semiconductor materials. Perovskite solar cells possess a tunable energy band gap, implying that the band gap's value may be modified by adjusting the perovskite materials composition. For instance, the energy band gap can be tuned to different values from 1.5-2.0 eV by varying the types of halogen atoms present in the perovskite compound [53–55]. The absorption edge of the perovskite materials may be adjusted by controlling the energy band gap value, which allows for optimization of the device's performance. In relation to this specific property, in this study the energy band gap of $CsPbI_3$ was tuned using two different strategies, namely; doping the material with mixing halide anions iodine and bromine as well as doping with small concentrations of transition metals.

The X-site anions in perovskite materials directly affect the band edge states and determine the opto-electronic properties of the materials [56]. The most common X anions used in perovskites are halide anions F, Cl, Br, and I. These halides have seven valence electrons, and their respective ionic radii are 2.20, 1.96, 1.81 and 1.33 Å for I, Br, Cl and F, respectively. When the ionic radius of the halide anion decreases, it leads to a reduction in the bond length between the Pb atom and X anion in the perovskite material. Consequently,

the coupling of atomic orbitals between the Pb and the anion becomes stronger, resulting in an increased overlap of the wavefunctions. This enhanced overlap has the effect of enlarging the energy band gap. In other words, increased interaction of electron wave functions, more repulsion leading to large band gaps.

The thermal stability and the exciton binding energy of the materials are dependent on the band gap. An exciton is an electron-hole pair that is produced when a photon with energy greater than a semiconductor's optical band-gap is absorbed [57]. The electrostatic energy that binds the electron-hole pair together is known as the exciton binding energy (EB). For effective dissociation of excitons and the generation of free electron-hole pairs in a semiconductor, it is essential for the EB to be relatively low, approximately on the scale of thermal energy. Perovskites, characterized by a smaller band gap, exhibit enhanced thermal stability; however, this is accompanied by a reduction in exciton binding energy, potentially resulting in decreased efficiency. For this reason, achieving a balance between the energy band gap and the other properties of these perovskites is essential in order to maximize the performance of the solar cells. Shumao *et al.* reported on the band gap engeineering of $CsPbI_3$ to over 1.7 eV by incorporation of a small fraction of ethylammonium ($x<0.15$); as well as enhanced stability and improved transport properties [58].

2.3.3 Carrier Recombination

Carrier recombination is a process in which electrons and holes (positively charged carriers) that are separated during the absorption of light, come back together and recombine, releasing energy in the form of heat or light. It is an undesired process in solar cells because of reduction of the cell's efficiency by preventing the carriers from reaching the electrodes and contributing to the current. Radiative recombination and non-radiative recombination are two types of carrier recombination processes. Radiative recombination refers to direct band-to-band transitions of an electron from the conduction band to the valence band while emitting a photon. This process is known as luminescence and used mostly for light-emitting diodes applications. Non-radiative recombination results in the release of heat and is not useful for energy conversion. The rate of carrier recombination in PSC is influ-

enced by different factors, including the perovskite-electrode interface, temperature, and the amount of defects and impurities within the material. Current development and scientific research include working on developing strategies to reduce the carrier recombination in PSC, including passivating the surface defects, reducing the density of impurities and defects, and engineering the electrodes and perovskite interfaces.

Yuang *et al.* reported on the contribution of deep trap states in carrier recombination in $CsPbI_3$ [59]. The study reported that deep trap states can significantly increase of non-radiative recombination rate in the material, which reduces device efficiency. Also, the findings proposed that reducing the density of deep trap states through careful control of fabrication conditions could be an effective approach to improving device performance. Furthermore, Huimin *et al.* proposed that controlling the grain size and orientation of the material could be a useful approach for reducing the density of grain boundaries while enhancing performance of the device [60].

2.3.4 Charge Transport

Charge transport refers to the movement of electrons and holes (collectively referred to as charge carriers) through a material, and it is a key parameter that influences solar cell performance. In PSC, charge transport occurs through the movement of electrons and holes through the photoactive layer and the charge transport layers, which are in contact with the electrodes [61]. The performance of charge transport in PSC is affected by numerous factors, including the quality of the perovskite material, band level alignment between the constituent layers, and the interface between the perovskite layer and the electrodes. These variables collectively determine how effectively charges (electrons and holes) are transferred within the device, impacting its overall performance and efficiency. In general, the charge transport layers should have high electron conductivity, and a low density of defects and impurities to minimize the charge carriers recombination. It is crucial to note that while the perovskite layer itself is involved in charge generation, the surrounding transport layers are responsible for efficient electron and hole transport within the device. The perovskite material quality is crucial for the solar cell performance, as impurities and defects in the

material can function as recombination centers and reduce the efficiency of charge transport. Additionally, the grain size of the perovskite material may also influence the charge transport, as larger grain sizes can promote better charge transport by reducing the density of defects and impurities. Several strategies on improving the charge transport in PSC have been proposed throughout the years, for example, modifying the ABX_3 perovskite material, optimizing the charge transport layers, and engineering the perovskite-electrodes interface [62, 63]. Ling *et al*. used a facile surface passivation technique for $CsPbI_3$ quantum dots film by adapting different cesium salts, namely cesium nitrate ($CsNO_3$), cesium carbonate (Cs_2CO_3), cesium acetate (CsAc),and cesium idodide (CsI) [64]. The quantum dots (QDs) films treated with CsAc demonstrated enhanced free carrier mobility and decreased trap-assisted non-radiative recombination. These enhancements are attributed to the improvement of surface passivation and electron coupling.

Depending on the arrangement of charge transport layers, perovskite solar cells (PSCs) can be classified into two types: the regular negative-intrinsic-positive (n-i-p) structure and the inverted positive-intrinsic-negative (p-i-n) structure demonstrated in Figure 2.6. In these configurations, the light-absorbing perovskites are positioned between an electron transport layer (ETL) and a hole transport layer (HTL) or vice versa. Below is the process happening in Figure 2.6 (b) and (d):

1. Photon harvesting and charge generation
2. Electron (e^-) transport and collection
3. Hole (h^+) transport and collection
4. Charge recombination and p-type contact
5. Charge recombination and n-type contact

Efficient charge carrier generation (process 1 in Fig. 2.6), as well as extraction and transport (processes 2 and 3 in Fig. 2.6), are essential for achieving high power conversion efficiencies (PCEs). Suitable HTL and ETL can enhance charge carrier extraction and minimize recombination (processes 4, and 5 in Fig. 2.6).

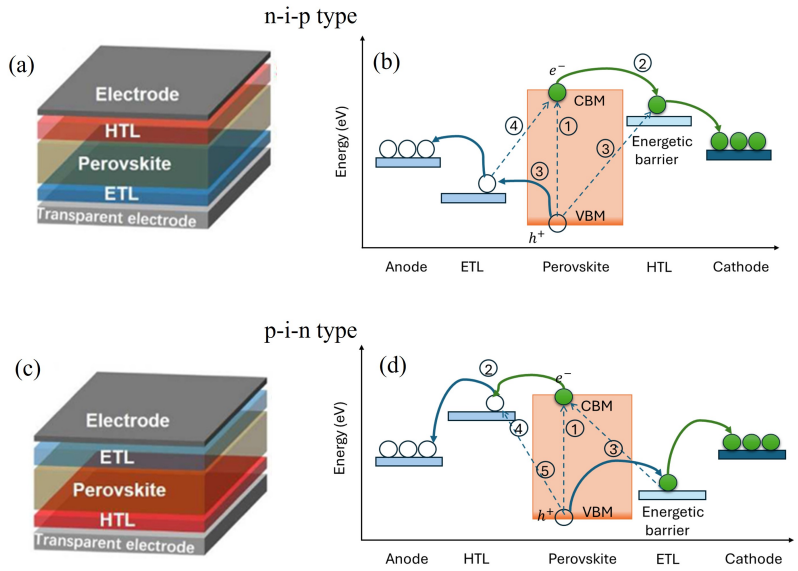


Figure 2.6: Device architecture of (a) n-i-p and (b) the charge transport process type PSCs, (c) p-i-n with (d) charge transport process in p-i-n type PSCs.

2.3.5 Power Conversion Efficiency

The halide perovskites are used mostly for solar cell applications and have shown a rapid growth in terms of efficiency since they were discovered compared to other materials for photovoltaic application based on the US National Renewable Energy Laboratory (NREL) as demonstrated in Figure 2.7 [65].

The efficiency of a solar cell (also known as PCE, (η)) is defined as a ratio of input and output power in a device or system designed to convert one form of energy into another. This ratio is typically expressed as a percentage, and it represents how effectively the device or system is able to convert energy from one form to another. The overall PCE (η) of the photovoltaic cell can be calculated as:

$$\eta = \frac{P_{\max}}{P_{in}} = \frac{V_{oc} I_{sc} FF}{P_{in}} \tag{2.2}$$

where I_{sc} is the short-circuit photo-current density, V_{oc} is the open-circuit voltage, FF is the fill factor, and the incident light intensity (P_{in} = 1000 mW/c^2). PCE is a widely used parameter to quantify and compare different solar cells. Several factors such as the solar emission spectrum, the band gap of the photo-active layer and the operational tempera-

ture determine the power conversion efficiency of any solar cell device. Earth-based solar cells are typically evaluated under standard testing conditions at 300 K temperature and illumination equivalent to the AM 1.5 solar spectrum. The irradiance of AM 1.5 solar spectrum corresponds to an input intensity. The AM 1.5 denotes the spectrum of sunlight that has reached the surface of the Earth surface after passing through the air mass, AM, of the Earth's atmosphere on a journey that is 1.5 times the shortest (normal incidence) path length.

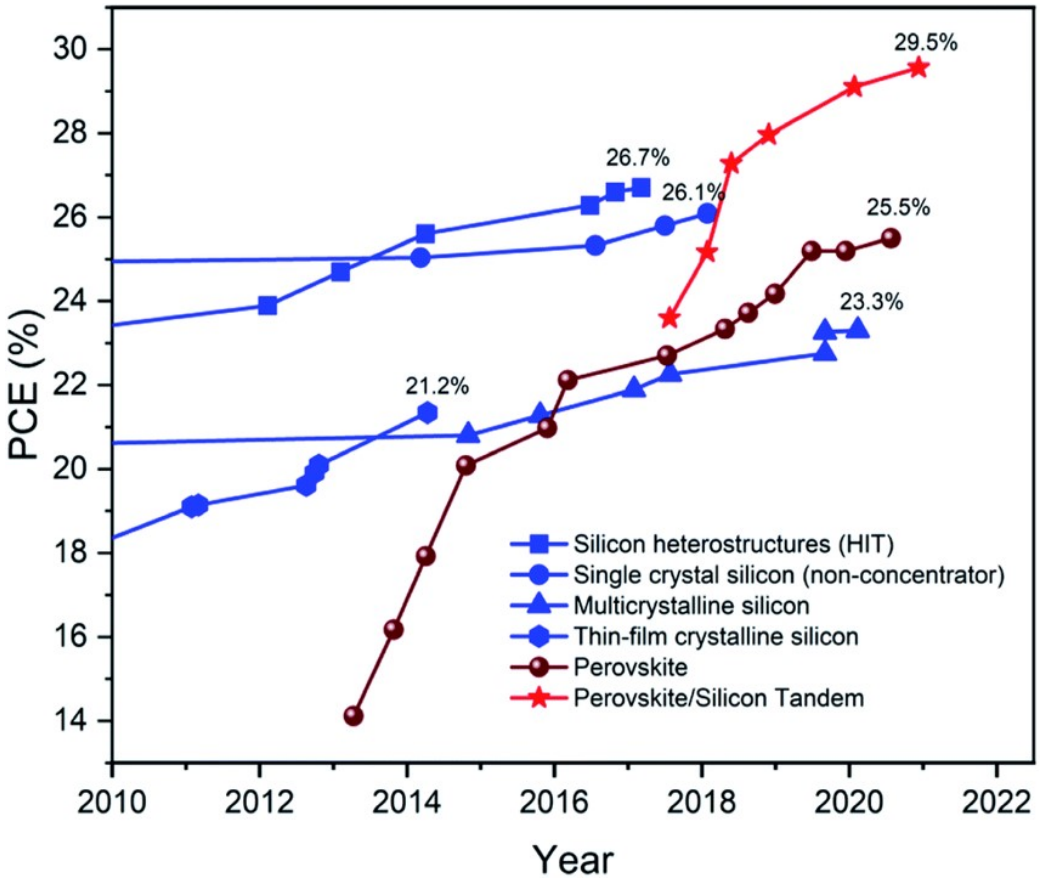


Figure 2.7: Efficiency graph for silicon, perovskite, and tandem silicon-perovskite devices during the past ten years. Information extracted from the US NREL's efficiency graph [65].

2.4 Operational Principle of Perovskite Solar Cells

The structure of a PSC device comprises five distinct layers, each playing a crucial role in the device's functionality. These layers include the absorber layer whose band gap determines the threshold photo absorption and exciton generation rate, the low work function metal cathode to extract electrons, a high work function photoanode which is formed from a

transparent conducting oxide such as ITO, hole and electron transport layers. A schematic to illustrate the structure and arrangement of these layers is presented in Figure 2.8. In addition, for the device to operate more effectively in PV technology, factors including internal photon conversion efficiency (IPCE), open circuit voltage , fill factor, short circuit current density, and solar cell's response range must be taken into account. Photovoltaic systems operate in three stages listed below:

- stage 1: photon absorption, followed by free charge carrier generation,
- stage 2: charge transport, and
- stage 3: charge extraction.

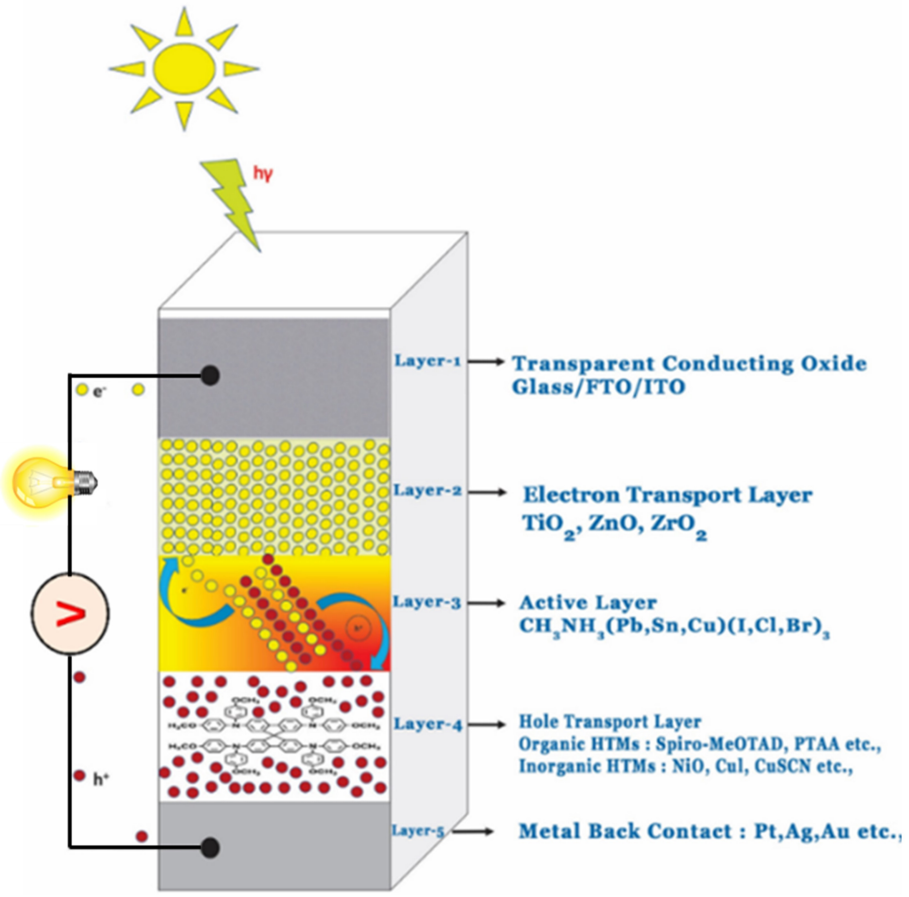


Figure 2.8: An illustration of perovskite solar cell layers [66].

Figure 2.8 illustrates that when the device is exposed to sunlight, excitons are generated in the absorber layer, then these excitons are then separated into holes and electrons. These charge carriers are transported by the respective electron and hole transport layers to their designated electrodes, where they are collected to contribute to the electrical current gener-

ated by the photovoltaic device [66]. The functions of the different layers are summarized in the next subsections.

2.4.1 Hole Transport Layer

The materials used as HTL can either be organic or inorganic, made of materials including CuO, NiO_x, PTAA, MoO_x, CuI, Spiro-OMeTAD, etc. [67–69]. The role of the HTL also known as anode interfacial layer is to facilitate the extraction and transportation of holes while preventing electrons from entering the anode. To ensure proper functioning, the highest occupied molecular orbital (HOMO) of the hole transport material is required to be somewhat higher than the perovskite absorber layer. This energy alignment aids in the efficient collection and transport of charge carriers within the photovoltaic cell.

2.4.2 Electron Transport Layer

Electron transport material (ETM) is responsible for collecting and transporting electrons from the perovskite absorber layer to the cathode, while it blocks (prevents) holes from flowing into the cathode. It is required that the conduction band must be lower compared to the ETM perovskite layer. The ETM must have a high UV-visible transmittance due to allowing all photons to travel through and be maximally collected through the absorber layer. The materials that are mostly used are metal oxides such as SiO_2, SnO_2, TiO_2 and ZnO [70–72], also are known to assist in enhancing the PCE of solar cells. Transport layers must have high thermal stability and non-toxic elements. ETL materials are chosen for their ability to efficiently transport electrons from the photoactive layer (where sunlight is absorbed and generates electron-hole pairs) to the electrode. Efficient charge transport is crucial to prevent recombination of electron-hole pairs before they can contribute to the electrical current.

2.4.3 Active Layer Materials

In a solar cell, the active layer (perovskite) material is the layer where light absorption and electron-hole pair generation occur, leading to the generation of electric power. The common active layer materials used in photovoltaics are crystalline silicon [73], thin-film silicon [74], CIGS [75], CdTe [76], and recently perovskite materials [77–79].

The most commonly used active layer material in commercial photovoltaic cells is crystalline silicon because of its high efficiency and stability. Thin-film silicon is also commonly used because of its lower cost and easy to manufacture. In addition, CdTe and CIGS are thin-film materials that have demonstrated promising commercial applications due to low manufacturing costs and their high efficiency [75, 76]. Perovskite materials are a newer class of active layer materials with promising high PCE, however their long-term stability and scalability for commercial production still need to be addressed.

At 550 nm [80], this inorganic ($CsPbI_3$) metal halide perovskite material demonstrate significant absorption with a wavelength of 1.5 x $10^4 cm^{-1}$. The structure of these metal halides allows for the modification of their band gap. They possess a high dielectric constant, absence of deep trap states in the energy band gap leading to long carrier lifetime, and high mobility for charge carriers [81]. Moreover, they have an extended lifespan for charge carriers, are composed of multiple crystals, and exhibit effective transfer of both positive and negative charges.

2.4.4 Transparent Conducting Oxide

The TCOs are defined as a class of materials that have both electrical conductivity and a high transmittance within the visible range. Transparent conducting oxides typically include a non-metal component, denoted as B, which is mostly oxygen. When combined with various metals or metal combinations, element A forms compound semiconductors, denoted as A_xB_y, which exhibit distinct opto-electrical properties. TCOs can be made out of several materials such as NiO, ZnO, In_2O_3, SnO_2, etc. The material must be transparent like glass but also conductive like metal [82, 83].

2.4.5 Back Contact Materials

Metal contacts also known as electrodes are essential components in solar cells. Their main function is to gather electron/hole charge carriers and transfer them to the load where electricity is needed. To ascertain efficient collection and minimize recombination, the interface between the metal and semiconductor contact should be well designed. In the case of PSC, the nature of this interface can vary according to the architecture of the solar cell. Thus, the contact between the metal and semiconductor can be either an inorganic or organic interface. The choice between the two options depends on the specific configuration of the photovoltaic. In most high-performance PSC that utilize spiro-OMeTAD as the hole transport material, the back electrode materials commonly employed are gold (Au) and silver (Ag) [73].

2.5 Current Performances of the Devices

A remarkable progress has been made in PSC devices, and their performance has improved considerably. Currently, PSC have achieved power conversion efficiencies higher than 25 % [84], almost comparable to that of traditional silicon photovoltaic devices. These high efficiencies are achieved by carefully engineering the perovskite material, charge transport layers, and perovskite-electrode interfaces. In addition to their high efficiencies, PSCs also have added advantages over traditional silicon solar cells. For example, perovskites can be easily synthesized at low temperatures and using low-cost solution processing methods, which can reduce the cost of production. Furthermore, PSC may also be made flexible and semi-transparent, opening new applications including flexible electronic devices and building-integrated solar cells.

However, there are still challenges to be addressed before perovskite solar cells can be widely commercialized. One of the major challenges is their stability, as perovskites can degrade over time due to environmental factors including change in temperature and humidity. Additionally, the toxicity of lead also needs to be addressed. Research is ongoing to improve their stability and safety, and it is expected that the performance of these devices

will continue to improve in the future. Incorporation of the defects into all-inorganic halide ABX_3 perovskites acts as an additional lever other than compositional engineering, for altering the properties of perovskites materials. Illustrated in Figure 2.9 is the effect of elemental doping on improving the performance of PSCs. Doping with different elements improve the different aspects of performance of PSCs, for example doping with group I and II elements improves the optoelectronic properties and structural stability as illustrated in the picture [85]. Relevant to this study, the effect of elemental doping on the optoelectronic properties of perovskite materials is further discussed in the next section.

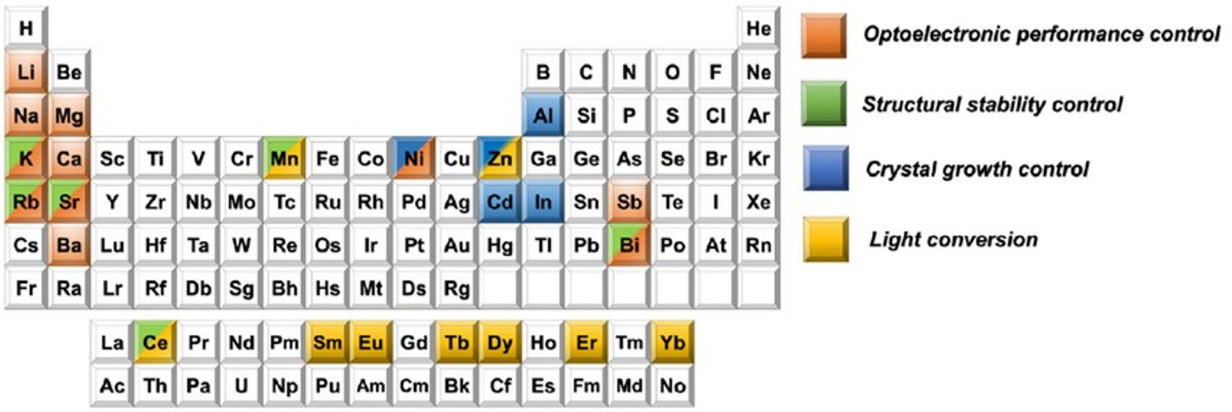


Figure 2.9: Different doping elements and their functions in tailoring lead halide perovskites [85].

2.6 Doping and Halides Mixing as Mechanisms of Improving the Performance of Perovskites

Of interest to this study, the effect of different elemental doping classified as A-, B-, and X-site doping are briefly discussed in this section. Doping involves introducing impurities into the target lattice to modify the properties of the material, which is important for different technologies. According to reports, doping can affect the performance of $CsPbI_3$ perovskites in different ways based on the doping site [86]. On the other hand, elemental mixing involves adding impurities with higher concentrations.

2.6.1 A-site Doping

Adjusting the $CsPbI_3$ perovskites with elemental doping modifies the tolerance factor (t) and octahedral factor (μ) values, in some instances stabilizing the structure. The t value can be adjusted to be in the range of 0.9 and 1, by substituting Cs^+ ions of larger ionic radii, thus adjusting A-site to improve the stability of $CsPbI_3$ materials. However, A-site adjustment with other inorganic metals does not contribute much in stabilizing all inorganic halide perovskites since Cs^+ is one of the largest cations in IA group elements. Section 2.3 discussed reports from several studies in which Cs^+ ion was replaced by Rb and K and highlighted the challenges [48, 87]. It is beyond the scope of this study to replace Cs^+ ion with other ions, hence A site doping is not discussed in detail.

2.6.2 B-site Doping

One of key issues in most Pb-based halide perovskites is that Pb can dissolve in H_2O, posing a serious environmental and health risk when the panel breaks or becomes wet, such as when it rains. Several studies reported that the most hazardous phase of the PSC life cycle for the environment is the operational phase outdoors, with the possibility of water ingress into a damaged panel and subsequent leaching out of Pb [88–90]. Bivalent Ge and Sn are considered as potential candidates in substituting toxic Pb since they have the same electronic configuration. B-site compositional engeneering is much less explored, while the limited reported results show great potential to be further explored. The effect of stability by partial substitution in $CsPbI_3$ and mixed halide $CsPbI_{3-x}Br_x$ of Pb^{2+} with other elements is not fully understood.

The first $CsSnI_3$ as a solid electrolyte in DSSCs was studied by Chung *et al.* [91]. The replacement of Pb with Sn in ABX_3 perovskite crystal structures does not alter the original cubic crystal structure. This is attributed to the smaller atomic radius of Sn (1.35 Å) compared to Pb (1.49 Å) [86]. However, this substitution does have an impact on the energy band gap of the perovskite material. Sn-based perovskites tend to have narrower band gaps than their Pb-based compounds, which suggests the potential for increased efficiency in Sn-based PSCs [92]. The photovoltaic performance of inorganic tin halide perovskites,

specifically $CsSnX_3$ is strongly influenced by their chemical composition. The energy band gap and crystal structure of $CsSnX_3$ vary, on the compositional elements. For example, variations in composition lead to $CsSnIBr_2$ that has a direct band gap of 1.65 eV and 1.37 eV for $CsSnI_2Br$ [93]. $CsSnI_3$ perovskite is considered as another alternative for PSC owing to its narrow band gap and outstanding optoelectronic properties, with an anticipated 23 % of power conversion efficiency [94, 95]. However, $CsSnX_3$ perovskites including $CsSnI_3$, are susceptible to oxidation, where Sn^{2+} ions can be converted to Sn^{4+}. This oxidation process significantly hampers their efficiency and can lead to rapid device degradation or breakdown. This oxidative instability poses a major challenge for Sn-based perovskite materials in PSCs. Furthermore, Sn-based ABX_3 perovskites are commonly characterized as a p-type metallic systems. This behavior arises from the combined effects of tin oxidation and the low formation energy of Sn defects, which result in significant "self-doping" within the material. This self-doping phenomenon further complicates the optimization of device performance and limits the solar cells efficiency.

Germanium is one of the element with the potential of replacing Pb due to an electronic configuration similar to that of Sn and Pb, but the ionic radius is smaller (0.73 Å). Inorganic perovskite based on Ge was first synthesized in 2015 and has been found to have energy band gap (1.6 eV) and higher ionic conductivity relative to those that are Pb or Sn [25] based, which makes them suitable for solar cell devices. But, the PCE achieved by $CsGeI_3$-based solar cells was relatively low, measuring only 0.11 % [96]. A higher PCE of 4.94 % was reported in 2018 for $CsGeI_3$ material, indicating significant advancements in optimizing the device architecture and fabrication processes [97]. This improved efficiency value demonstrates the feasibility and potential of $CsGeI_3$ as an absorbing material for PSCs, although further development and scientific research are still required to enhance its performance.

B-site doping can change the intensity and distance of B-X bond length, thereby increasing the phase stability and environmental tolerance. However, partial substitution with other ions is more challenging because of larger formation energy of B-site. Zou *et al*. conducted an analysis of the formation energy for $CsPbX_3$ nanocrystals doped with man-

ganese (Mn) using first-principle calculations [98]. Their findings showed that substituting Pb^{2+} with lower concentration of Mn^{2+} in the lattice of $CsPbX_3$ increased the formation energy and resulted in lattice contractions. This contraction was because of bond length variation among Mn–Br and Pb–Br bond lengths, which induced lattice distortions that stabilized $CsPbX_3$ crystal structure.

Akkerman *et al*. studied the effects of partial replacement of Pb^{2+} with Mn^{2+} in the $CsPbI_3$ system. The authors also examined the impact of this substitution on the electronic structure, but found that there were no significant photoluminescence changes with Mn-doped systems [99]. This was supported by their comparison of densities of states of undoped $CsPbI_3$ and $CsPb_{0.88}Mn_{0.12}I_3$ perovskites using the exchange correlation of HSE06 functional. Manganese ions (Mn^{2+}) has emerged as the most widely used dopant among transitional metals in perovskite materials. It has attracted significant attention for over a decade in the area of doped metal perovskites due to its d electron energy levels, which align favorably within the band gap of various semiconductors. This characteristic has made (Mn^{2+}) a highly sought-after dopant for introducing d electron energy levels into perovskite structures. Manna *et al*. demonstrated the positive effects of incorporating Mn^{2+} ions into nano-crystal structures of $CsPbI_3$ [99]. The inclusion of Mn^{2+} led to a notable increase in phase stability, both in films and in solution. Remarkably, this enhanced phase stability was maintained for a duration exceeding one month [99]. These results showed the potential of doping perovskite materials with Mn^{2+}, specifically $CsPbI_3$, to enhance the stability of the phases, which is necessary for the practical application and long-term performance of perovskite-based devices. The research underscores the significance of Mn^{2+} as a dopant for improving the stability and reliability of perovskite materials. To extend the body of knowledge in B-site doping, in this study Mn, Fe, Ni, and Zn doped $CsPbI_3$ is investigated. These are non-toxic transition metals, with smaller ionic radius than Pb^{2+}. Doping with transition metal could introduce new energy levels into $CsPbI_3$, ultimately enhancing stability and opto-electronic properties.

2.6.3 X-site Doping

Long term stability of halide perovskite compounds has been a challenge because of sensitivity to environmental exposure to oxygen, heat, light and moisture. All-inorganic metal halide perovskite, $CsPbI_3$ exists in four polymorphs depending on temperature including the black cubic phase (α-phase, 1.73 eV), orthogonal phase (γ-phase, 1.75 eV), tetragonal phase (β-phase, 1.68 eV), and yellow non-perovskite phase (δ-phase, 2.82 eV). The dynamic instability of the black phase in $CsPbI_3$ has a significant impact on the lattice structure and polarization. This instability ultimately influences the opto-electronic properties and characteristics of the perovskite materials. X-site ions are crucial in adjusting t and μ value to make it optimal, despite the broadening of the band gap [100]. According to the recent findings, self-degradation of iodide can reduce the lifespan of iodine-containing PSCs [70].

It is essential to discover methods for stabilizing the cubic phase at the ambient temperature. One possible method is to decrease the crystal size, which is known as size-controlled stability. This approach involves the creation of $CsPbI_3$ quantum dots, and reducing crystal size can promote the formation of a more symmetrical cubic structure [40]. Several studies have been reported on $CsPbI_3$ phases stability by modifying the perovskite's grain size (i.e., by producing quantum dots) due to the significant contribution of surface energy [40]. $CsPbX_3$ QDs have enhanced stability of cubic polymorph at ambient temperature as well as desirable optical properties for different applications. [101].

Halogen doping is another solution to overcome stability issue of all-inorganic perovskites. This perovskite material may be further stabilized at room temperature by partially substituting I^- in $CsPbI_3$ with Br^-. Saliba *et al.* reported that Cs^+ and X = I^- or Br^- can improve the electronic coupling across QDs, which in turn increases carrier mobility [100]. The stability of perovskites has been shown to improve by chemical intervention at grain boundaries, this may make the process of water getting into the perovskite layer more difficult. [102]. The mixed-halide $CsPbI_2Br$ showed an enhanced Goldschmidt tolerance factor (0.84) as well as a better stability of the cubic phase, which paves the way for an incredibly stable all-inorganic PSCs [103]. The combination of various halogen ions (I^-,

Br^-, F^- and Cl^-) can increase the carrier mobility while reducing non-radiative recombination that is assisted by bulk traps [65]. By introducing Br^- ions into $CsPbI_3$ perovskite using mixed halide composition via a two-step approach, Snaith *et al.* reported experimental results with greatly improved ambient thermodynamic stability, exceeding that of hybrid perovskite [101]. In this study, $CsPbI_3$ is doped with different concentrations of Br.

3

Theoretical Method

3.1 Background

The non-relativistic Schrödinger equation for the many-electron wavefunction is defined using the relation $\Psi(r_1, r_2, \ldots, r_n)$, where r_i represents the position of the i^{th} electron, serves as the theoretical fundamental building blocks of the electronic structure of matter. The Schrödinger equation should be solved on a microscopic level, interacting electrons in solids. The electronic density functional, $\rho(r)$ that only depends on three spatial coordinates and the spin plays an important part in DFT, a substitute approach to the description of matter in the electronic structure. DFT solves many-body problems depending on the two theorems proposed by Hohenberg and Kohn (H-K) in 1964 [104] and Kohn and Sham (K-S) in 1965 [105]. DFT in the H-K formulation is derived from the n-particle

Schrödinger equation but represented in terms of the electron density $\rho(r)$. Also, in the K-S formulation can be represented by two functions, namely electron density $\rho(r)$ and single particle wavefunctions $\psi(r)$.

3.2 Many-Body Problem and Schrödinger Equation

The basic difficulty in computational materials science, chemistry and condensed matter physics, involves determining the properties of matter, particularly the dynamics of many-electron systems and geometrical structures. These systems include everything from mesoscopic systems to individual atoms, which are the fundamental building blocks of matter, as well as all other forms of molecules [106]. The electronic structure of matter can be determined by the basic Schrödinger's equation being solved, which is expressed analytically in a general form:

$$\hat{H}\Psi(\mathbf{R}_I;\mathbf{r}_i;t) = i\hbar\frac{\partial}{\partial t}\Psi(\mathbf{R}_I;\mathbf{r}_i;t) \tag{3.1}$$

with $\hat{H}$ describing the Hamiltonian and wavefunction Ψ of a many-body system in a the quantum mechanical system, $\mathbf{R}_I$ $(I = 1,2,3,\ldots,P)$ denotes the position vector of the I^{th} nucleus, $\mathbf{r}_i$ $(i = 1,2,3,...,N)$ denotes the position vector of the i^{th} electron and finally, N denotes the number of nuclei and P denotes the number of electrons. The many-body problem may be deconvoluted to electron-electron, nuclei-nuclei and electron-nuclei Coulombic interactions. Consequently, the $\hat{H}$ of the quantum mechanical system is defined analytically as:

$$\begin{aligned}\hat{H} = &-\frac{\hbar^2}{2m_e}\sum_i \nabla_i^2 + \sum_{i,I}\frac{Z_I e^2}{|\mathbf{r}_I - \mathbf{R}_i|} + \frac{1}{2}\sum_{i\neq j}\frac{e^2}{|\mathbf{r}_i - \mathbf{r}_j|} - \sum_I \frac{\hbar^2}{2M_I}\nabla_I^2 \\ &+ \frac{1}{2}\sum_{I\neq J}^{P}\frac{Z_I Z_J e^2}{|\mathbf{R}_I - \mathbf{R}_J|},\end{aligned} \tag{3.2}$$

The parameters $\hbar$ represent the reduced Planck constant, m is the electron mass and e is the elementary charge, and lastly, M_I and Z_I are the masses and charges of the nuclei

respectively. [107–109]. The Hamiltonian is then expressed as:

$$\hat{H} = \hat{T}_e + \hat{V}_{ee} + \hat{T}_n + \hat{V}_{nn} + \hat{V}_{en}. \tag{3.3}$$

The different terms are the electronic kinetic energy:

$$\hat{T}_e = -\frac{\hbar^2}{2m_e}\sum_i \nabla_i^2 \tag{3.4}$$

The electronic Coulomb interaction is given by:

$$\hat{V}_{ee} = \frac{1}{2}\sum_{i\neq j}\frac{e^2}{|\mathbf{r}_i - \mathbf{r}_j|} \tag{3.5}$$

The total kinetic energy of the N nuclei in the quantum mechanical system is given by:

$$\hat{T}_n = -\sum_I \frac{\hbar^2}{2M_I}\nabla_I^2. \tag{3.6}$$

The nuclei-nuclei interaction is expressed as:

$$\hat{V}_{nn} = \frac{1}{2}\sum_{I\neq J}\frac{Z_I Z_J e^2}{|\mathbf{R}_I - \mathbf{R}_J|} \tag{3.7}$$

And the Coulomb interaction of the electron-nuclei system is expressed as:

$$\hat{V}_{en} = \sum_{i,J}\frac{Z_i e^2}{|\mathbf{r}_I - \mathbf{R}_i|} \tag{3.8}$$

The time-independent form of the Schrödinger equation (3.1) can now be derived over time as:

$$\Psi\left(\{\mathbf{R}_I;\mathbf{r}_i\};t\right) = \Psi\left(\{\mathbf{R}_I;\mathbf{r}_i\}\right)\mathrm{e}^{-\mathrm{i}(E/\bar{h})t} \tag{3.9}$$

and it becomes:

$$\hat{H}\Psi\left(\{\mathbf{r}_i\},\{\mathbf{R}_I\}\right) = E\Psi\left(\{\mathbf{r}_i\},\{\mathbf{R}_I\}\right). \tag{3.10}$$

In the Born-Oppenheimer approximation, the groundstate energy, denoted as $\bar{E}_{\mathrm{GS}}$, corre-

lates with the lowest eigenvalue in the energy spectrum of the Hamiltonian's system. This eigenvalue accounts for the electrons, nuclei and the total energy, (E_{tot}) of the system. The parameter, $E_{GS,tot}$ of the groundstate of the system's motion or variation may be denoted within this approximation as:

$$\bar{E}_{\mathrm{GS}} = E_{\mathrm{GS,tot}} = E_{\mathrm{GS}} + V_{\mathrm{nn}} \tag{3.11}$$

where $\bar{E}_{\mathrm{GS}}$ is the total groundstate of the electronic system and $\hat{V}_{nn}$ denotes Coulomb energy of nuclei-nuclei interaction. It is worth noting that the Hamiltonian used to calculate $\bar{E}_{\mathrm{GS}}$ still includes the electrons-nuclei Coulomb interaction, $\hat{V}_{en}$. This is known as the external potential in DFT terms. The electronic wavefunctions must adhere Pauli's exclusion principle, i.e., be anti-symmetric in terms of electron exchange, and must also satisfy the normalization condition. It is impossible to solve Schrödinger's equation therefore approximations are needed. One of such approximation is discussed in the following section.

3.3 Born-Oppenheimer Approximation

The Schrödinger equation (3.1) cannot be solved without approximation due to the fact that any particle's motion in an interacting system is defined as a function of motion of all other particles. The initial approach to address this complexity and solving the Schrödinger equation for systems involving multiple electrons is the Born-Oppenheimer approximation. In the Born-Oppenheimer approximation, $\Psi(\mathbf{R}_I;\mathbf{r}_i)$ in equation (3.1) is approximated as a product to form [110]:

$$\Psi(\mathbf{R}_I;\mathbf{r}_i) = \Psi_e(\mathbf{R}_I;\mathbf{r}_i)\,\Psi_n(\mathbf{R}_I) \tag{3.12}$$

where $\Psi_e(\mathbf{R}_I;\mathbf{r}_i)$ represents the wavefunction of the electron and $\Psi_n(\mathbf{R}_I)$ represents the wavefunction of the nucleus. Born-Oppenheimer approximation assume the nuclei move slower compared to the electrons in equation (3.12) and ignores their motion and treated

them as static. Using these two equations (3.1) and (3.12), we obtain a pair of equations:

$$\begin{aligned}\hat{H}_e\Psi_e(\mathbf{R}_I;\mathbf{r}_i) &= \left[\hat{T}_e+\hat{V}_{ee}+\hat{V}_{en}\right]\Psi_e(\mathbf{R}_I,\mathbf{r}_i)\\ &= E_e\Psi_e(\mathbf{R}_I;\mathbf{r}_i)\end{aligned} \tag{3.13}$$

and the nucleus Hamiltonian is given by:

$$\begin{aligned}\hat{H}_n\Psi_n(\mathbf{R}_I) &= \left[\hat{T}_n+\hat{V}_{nn}+E_e\right]\Psi_n(\mathbf{R}_I)\\ &= E_e\Psi_n(\mathbf{R}_I)\end{aligned} \tag{3.14}$$

Then the electronic Hamiltonian is reduced to:

$$\hat{H}_e = \hat{T}+\hat{V}_{ee}+\hat{V}_{en}. \tag{3.15}$$

It is challenging to deal with the numerical and conceptual issues associated with $\hat{V}_{ee}$ in Equation (3.15) which is the electron-electron interaction. This complexity may be lessened though the solution of equation (3.15) always remains difficult [111]. Thus, in order to address this problem, alternative approximations were derived. Hartree-Fock method is based on such alternative approximations and is discussed next in section 3.4.

3.4 Hartree-Fock Method

Some approximations can significantly reduce the complexity. The Hartree-Fock (H-F) method aims to approach the wavefunction by adjusting the electron-electron interaction differently [112]. Thus, the product of the one-electron wave-functions must equal to the electronic wave function of N uncorrelated electrons:

$$\Psi(y_1,y_2\ldots y_N) = \Psi(y_1)\Psi(y_2)\ldots\Psi(y_N) \tag{3.16}$$

This ansatz simplifies the Schrödinger equation for the entire system into a set of independent single-particle equations, making the calculations more tractable. The problem

with HF approach is that it does not comply with Pauli's exclusion principle because anti-symmetry requirement is not met [110]. This problem can be solved by two electrons with wavefunctions such as this:

$$\Psi(y_1, y_2) = \frac{1}{\sqrt{2}} \left[\Psi_1(y_1)\Psi_2(y_2) - [\Psi_1(y_2)\Psi_2(y_1)]\right] \tag{3.17}$$

The wavefunction can be generalized by using determinants to consider any system size with the relation:

$$\Psi = \frac{1}{\sqrt{N!}} \begin{vmatrix} \Psi_1(\mathbf{y}_1) & \Psi_2(\mathbf{y}_1) & \cdots & \Psi_N(\mathbf{y}_1) \\ \Psi_1(\mathbf{y}_2) & \Psi_2(\mathbf{y}_2) & \cdots & \Psi_N(\mathbf{y}_2) \\ \vdots & \vdots & \vdots & \vdots \\ \Psi_1(\mathbf{y}_N) & \Psi_2(\mathbf{y}_N) & \cdots & \Psi_N(\mathbf{y}_N) \end{vmatrix} \tag{3.18}$$

called the Slater determinant [113]. A simplified Hamiltonian can be derived by removing the nuclear kinetic energy and repulsion terms. Following that, the Hamiltonian is then reduced to a pair of a single-electron equation written as:

$$\hat{H} = -\sum_{j=1}^{N} \frac{\nabla_i^2}{2} + \sum_{i=1}^{N} V(\mathrm{r}_j) + \frac{1}{2} \sum_{j \neq k}^{N} \frac{1}{|\mathrm{r}_j - \mathrm{r}_k|} \tag{3.19}$$

To solve the entire many-body Schrödinger equation is impossible. Instead, the variational technique was applied:

$$\left[-\frac{\nabla^2}{2} + V(\mathrm{r}) + \int d^3r' \frac{n(\mathrm{r}')}{|\mathrm{r} - \mathrm{r}'|}\right] \Psi_j(\mathrm{r}) - \sum_{k=1}^{N} \int d^3r' \frac{\psi_k^*(\mathrm{r}')\,\psi_k(\mathrm{r})}{|\mathrm{r} - \mathrm{r}'|} \Psi_i(\mathrm{r}') = \varepsilon_j \Psi_j(\mathrm{r}) \tag{3.20}$$

The Slater determinant follows the Pauli Exclusion Principle. Exchanging any two rows of a determinant alters the sign of Ψ, resulting in the anti-symmetry principle and with the variational theorem states that given a time-independent Hamiltonian with a discrete spectrum of eigenvalues whose lowest eigenvalue is the energy which is ε. The determinant vanishes, if two rows are similar. Two identical electrons cannot occupy the same spin orbitals at the same time. The H–F approach accurately describes electron exchange and

can be derived using the Rayleigh-Ritz variational method.

3.5 Density Functional Theory

DFT is a widely useful method within computational material sciences, chemistry and physics for determining the electronic structures of condensed matter and molecules. Any groundstate property for an interacting system may be derived using its electron-density of a non-interacting system, according to the basic principle of DFT. The H-F theorem does not address many-body impacts caused by electron exchange and correlation, which are considered as an electron-density. DFT can predict material properties such as E_{tot}, electron density, equilibrium structure, vibrational frequencies and parameters linked to total energy differences, such as defect surface and formation energies. Walter Kohn and Pierre Hohenberg's research in 1964 laid the groundwork for DFT's theoretical foundation [104]. The K-S DFT is the product of further research and development that was conducted by Kohn and Sham [105]. However, in the recent decades the exchange-correlation functional were developed, allowing the usage of density functional theory in practice.

3.5.1 Hohenberg-Kohn Theorems

About six decades ago, Hohenberg and Kohn [104] proposed two theories that formed the foundation of today's DFT, which is a solution to the many-body Schrödinger equation (3.1). Theorem 1 says that $V_{ext}(r)$ *is (up to an arbitrary constant) a distinct functional of* $\rho(r)$*; given that,* $V_{ext}(r)$ *solves H we observe that the full many particles groundstate is a unique functional of* $\rho(r)$.

The proof follows the contradiction method by assuming that the potentials, $V_{ext}(r)$ and $V_{ext}\prime(r)$ are various external potential, however it yields the identical groundstate density $\rho_0(r)$. According to the variational principles, the groundstate energy is given by:

$$\begin{aligned} E_0 < \left\langle \Psi' | \widehat{H} | \Psi' \right\rangle &= E_0' + \left\langle \Psi' \left| V_{\text{ext}} - V_{\text{ext}}' \right| \Psi' \right\rangle \\ &= E_0' + \int n_0(\mathbf{r}) \left[V_{\text{ext}} - V_{\text{ext}}' \right] d\mathbf{r}, \end{aligned} \tag{3.21}$$

and

$$\begin{aligned} E_0' < \langle \Psi | \widehat{H} | \Psi \rangle &= E_0 + \left\langle \Psi \left| V_{\text{ext}} - V_{\text{ext}}' \right| \Psi' \right\rangle \\ &= E_0 + \int \rho_0(\mathbf{r}) \left[V_{\text{ext}} - V_{\text{ext}}' \right] d\mathbf{r} \end{aligned} \tag{3.22}$$

Combining equation (3.21) and (3.22) creates a contradiction:

$$E_0 + E_0' < E_0' + E_0 \tag{3.23}$$

This implies that there are not two distinct external potentials $V_{ext}(r)$ that produce a similar groundstate electron density. Thus, the groundstate electron density precisely determines the $V_{ext}(r)$. This theorem indicates that the groundstate of a system that contains numerous electrons is solely defined by a density of electrons that relies on three spatial coordinates. It lays the basis to minimize the many-body problem of N electrons with 3N spatial coordinates to 3 spatial coordinates by employing the electron density functional. This H-K theorem may be expanded to time-independent fields in order to create a time-dependent DFT which may be employed to define excited states. It shows that the energy of the basic state is a unique electron density function expressed as:

$$E = E[\rho(r)] \tag{3.24}$$

where E denotes the groundstate energy and ρ denotes groundstate density of the system. Theorem 2 *states that the groundstate energy of the system, produces the least energy if and only if the given input* ρ *corresponds to the actual ground density* $E[\rho]$. By employing the electronic Hamiltonian equation, one can define the H-K energy functional as:

$$E[\rho] = \langle \Psi[\rho] | \widehat{H} | \Psi[\rho] \rangle = \left\langle \Psi[\rho] \left| \hat{T} + \hat{V}_{\text{ee}} \right| \Psi[\rho] \right\rangle + V_{\text{ext}}[\rho] \tag{3.25}$$

And from the variational principle:

$$E[\rho] < (F[\rho] + V_{\text{ext}}[\rho]) = F[\rho] + \int \rho(\mathbf{r}) V_{\text{ext}}(\mathbf{r}) d\mathbf{r} = E_0[\rho_0(\mathbf{r})] \tag{3.26}$$

Since the electron-electron interaction and kinetic energy terms depend only on the density. The universal H-K functional is defined as:

$$F[\rho] = \hat{T}[\rho(r) + E_{int}\rho(r)] \tag{3.27}$$

$F_{HK}[\rho]$ included the kinetic energy $\hat{T}[\rho(r)]$ and the interaction energy of the particles $E_{int}[n(r)]$.

The second H-K theory describes the system's energy function and verifies that the correct electron density in the groundstate minimizes the system's energy function:

$$\mathrm{E}[\rho(r)] > E_0[\rho_0(r)] \tag{3.28}$$

Based on the second theorem, the $\rho(r)$ provides a complete explanation of Schrödinger's equation and minimizes the entire energy functional, $E[\rho(r)]$. K-S presented an advantageous approach to calculate the minimum energy result of the total energy functional [114]. The method solves Schrödinger's equation in a simple system per electron. The K-S single electron system can therefore be defined as:

$$\left[-\frac{\hbar}{2m}\nabla^2 + V_{ext}(r) + V_H(r) + V_{xc}(r)\right]\psi_i = \varepsilon_i\psi_i \tag{3.29}$$

If universal functional within H-K theorems $F[\rho(r)]$ is unknown, it is practically difficult to determine any properties of the system. The properties of the system are resolved using the Kohn-Sham method which is presented in detail in the next subsection.

3.5.2 Kohn-Sham Equations

Hohenburg and Kohn published their discoveries on the representability of the external potential by the particle density, followed by K-S [104] by proposing the following assumptions: First, a system of interacting electrons is placed into a system of non-interacting electrons with a similar $\rho(r)$ as an interacting system. Second, the auxiliary Hamiltonian with an effective potential (r) and the kinetic operator are selected. The system's Hamilto-

nian [115] is described as:

$$H = T_s + V_s \tag{3.30}$$

The energy of this system according to H-K theory may be expressed analytically as:

$$E[\rho(r)] = T_s[\rho(r)] + \int V_s(r)\rho(r)dr \tag{3.31}$$

An electron density of a non-interacting electron system may be computed by summing over all occupied single-particle orbitals:

$$\rho(r) = \int_{i=1}^{N} |\psi_i(r)|^2 \tag{3.32}$$

The true system's energy functional, when the kinetic term is included in the equation is written as follows:

$$\begin{aligned} E[\rho(r)] = T_s[\rho(r)] + E_{xc}[\rho(r)] + \int V_s(r)\rho(r)dr \\ + \iint \frac{\rho(r)\rho(r')}{|r-r'|}drdr' \end{aligned} \tag{3.33}$$

having $E_{xc}[n\rho(r)]$ as an energy of the exchange-correlation. The variational principle can be determined using the K-S formulations:

$$\left[-\frac{\hbar^2}{2m_e}\nabla_i^2 + V_H(r) + V_{ext}(r) + V_{xc}(r)\right]\psi_i(r) = \varepsilon_i\psi_i \tag{3.34}$$

at which the potential exchange-correlation is represented as:

$$V_{xc} = \frac{\partial E_{xc}[\rho(r)]}{\partial\rho(r)} \tag{3.35}$$

The exchange-correlation energy functional is the only thing that remains unknown. K-S proposed a LDA and an enhancement using a gradient extension in their work since there was no exact form of it.

3.6 Exchange and Correlation Approximation

An E_{xc} must be approximated to use K-S DFT, where there is an expanding list of functionals with varying degrees of complexity. The "Jacob's ladder" rungs represent different density functional approximations which increase in complexity as one ascends it, according to Perdew [116]. We have chosen approximations relevant to this study and will be unpacked in the following subsections.

3.6.1 Local Density Approximation

The local density approximation (LDA) was widely used method for solids. The LDA is a straightforward functional and determines the E_{xc} as a function of the electron density $\rho(r)$ using this expression below:

$$\varepsilon_{xc}^{LDA}[\rho] = \int \rho(r)\varepsilon_{xc}^{HEG}(r)dr \tag{3.36}$$

Assuming E_{xc} is similar to a homogeneous electron gas (HEG) with the same electron density, which ρ can be expressed as:

$$\varepsilon_{xc}^{HEG}(\rho) = -\frac{2}{3}\left(\frac{3}{\pi}\rho(r)\right)^{\frac{1}{3}} \tag{3.37}$$

LDA normally overestimates correlation energy while underestimating exchange energy and to a certain extent, neglects these errors. LDA can determine the structural geometries and vibration frequencies very well; but considerably overestimate the binding energy. The drawback of this approximation is that it performs poorly in inhomogeneous systems due to the fact that it "washes out" the finer details of the charge density, such as those of the core electrons. This method demonstrates effective performance in practice for metallic, covalent and ionic compounds where it predicts firmer chemical bonds. However, when dealing with materials that are negatively charged, hydrogen bonds, and Van der Waals interactions, the LDA approximation is insufficient.

3.6.2 Generalized Gradient Approximation

The LDA is an approximation used in DFT to describe the exchange-correlation energy in terms of the local electron density. However, this approximation fails to provide accurate results when the density becomes significantly increasing, such as in molecules. To overcome the limitations of the LDA, an improvement is made by incorporating two variables: the electron density and the gradient of the electron density. These variables determines the E_{xc}, which is a crucial component in accurately describing the behavior of electrons in a system. By considering not only the density but also its spatial variations, this approach offers a more refined approximation that can better account for the complex interactions within the system. Generalized gradient approximation enhances LDA by incorporating terms based on the electron density gradient [117] expressed in equation (3.38).

$$E_{xc}^{GGA}[\rho] = \int \varepsilon_{xc}(r)[\rho(r), \nabla\rho(r)]d^3r \tag{3.38}$$

There are two main approaches employed in GGA, namely 1) by numerous parameters to improve accuracy; and 2) also by fitting few parameters as possible while maintaining accurate physical constraints specifically in the case of Perdew method. GGA preserves the properties of local density approximation because the previous terms remain in the formalism, but in general it improves the calculation of binding energy however performs poor in chemical accuracy and the underestimation of energy band gap. This is suitable for non-homogeneous systems such as molecules and surfaces with rapid electron density changes. There are number of generalized gradient approximation functionals including PBE, PBEsol, BLYP and PW91 [115, 117], which can be generated using the approximation.

3.6.3 Meta-Generalized Gradient Approximation

Meta-GGA often outperforms GGA in terms of accuracy since it takes into consideration the local kinetic energy density. As a result, compared to LDA and GGA, meta-GGA can handle different chemical bonds namely ionic, covalent, and metallic more accurately. By

adding the 2^{nd} or more derivative of the electron density or more, meta-GGA is one step further than GGA functionals and the kinetic energy density τ is written as [118]:

$$\tau(\mathrm{r}) = \sum_{\mathrm{i}} \frac{1}{2} |\nabla \varphi_{\mathrm{i}}(\mathrm{r})|^2 \tag{3.39}$$

and the E_{xc} is denoted by:

$$E_{xc}^{\text{meta-GGA}}[\rho] = \int \varepsilon_{xc}(r) \left[\rho(r), \nabla\rho(r), \tau(r)\right] d^3r \tag{3.40}$$

Meta-GGA are non-local functionals of the density, but also serves as a local density functional of orbitals. The construction of ε_{xc} is a complicated process that involves the orbitals, which is a key in constructing the 2^{nd} derivates of the density. The process is much more complicated for meta-GGA, unlike a straight forward process for GGA and LDA. The functionals include TPSS, M061 and the modified Berke Johnson potential [119–121].

3.6.4 Hybrid Functionals

The hybrid functional is an exchange correlation functional constructed by mixing DFT's LDA and GGA exchange correlation functionals with a portion of the hybrid exchange correlation functional. The hybrid functional is derived from the H-F's exact exchange functional [112, 122] and is given by:

$$E_{XC} = \alpha E_x^{HF} + (1-\alpha) E_x^{PBE} + E_c^{PBE} \tag{3.41}$$

in which α denotes the H-F mixing parameter (it controls the exact E_x^{HF} included in the hybrid functional). In several studies, the proportional of exact exchange is tuned accurately to reproduce different properties correctly. The parameters that determines how much of the exact exchange is mixed in are typically specified by fitting to experiments, but in some instances, an "adiabatic connection functionals" can be set by taking an inter-electronic strength parameter into account [123, 124].

3.6.5 DFT+U

Density functional theory with Hubbard U correction (DFT+U) is an extension of standard DFT that includes a correction term to account for the strong on-site Coulomb interactions among electrons in localized orbitals [125, 126]. Standard DFT calculations often struggle to accurately describe strongly correlated electron systems, where localized electrons may be subject to significant on-site interactions. In DFT+U, the Hubbard U term is added to the standard exchange-correlation functional to better capture the influences of electron-electron interactions [127]. The Hubbard U correction is particularly useful for systems with partially filled f or d orbitals, including transition metal oxides, rare-earth compounds, and other strongly correlated electron.

The Hubbard U term modifies the effective potential in the following way:

$$E_{\mathrm{DFT+U}} = E_{\mathrm{DFT}} + U \sum_{\text{occ. orbitals}} n_{i\uparrow} n_{i\downarrow} \tag{3.42}$$

where E_{DFT} is the standard DFT total energy, U is the Hubbard parameter representing the strength of on-site Coulomb interactions, $n_{i\uparrow}n_{i\downarrow}$are the spin-up and spin-down electron occupation numbers of the localized orbital at site i. The Hubbard U correction helps to enhance the description of electronic correlation effects and may result in more accurate predictions of electronic structure properties including the band gaps, magnetic moments, and charge densities in materials where strong electron correlations play a significant role [128]. The Hubbard U parameter is a key input in DFT+U calculations, and choosing an appropriate value for U can be challenging. The value of U is often determined through comparison with experimental data or other more advanced theoretical methods. Additionally, care should be taken to apply DFT+U judiciously, as it is not universally applicable and might not be suitable for all materials or situations.

3.7 Plane Wave Pseudopotential Method

Within the frameworks of DFT, the pseudopotential plane-wave technique for determining the groundstate properties of an extended systems. The K-S equations may be resolved through extremely effective numerical algorithms because of the simplicity of planewaves, and the use of pseudopotentials enables the expansion of the wavefunctions in a limited number of planewaves.

3.7.1 Plane Wave Basis Sets

The system's electronic wavefunctions must extend the infinite sets of plane wave basis. The planewave pseudopotential (PWP) method is an effective technique for determining material properties. This technique is commonly employed for periodic solids and solving atomic and surface problems simulated using supercells. Bloch's theory, which forms the foundation of this technique, crucially involves expanding electronic wavefunctions using a discrete set of plane waves as in the expression below:

$$\psi_i(r) = e^{[ik.r]} F_i(r) \tag{3.43}$$

The wavefunction has periodic cell, $F_i(r)$ and wave-like components:

$$F_i(r) = \sum_G C_{i,G} e^{[iGr]} \tag{3.44}$$

where G denotes the reciprocal lattice vectors in the periodic unit cell. Therefore, each electronic wavefunction may be represented analytically by:

$$\psi \mathrm{k}_i(r) = \sum_G C_{i,K+G} e^{[i(k+g)r]} \tag{3.45}$$

in which C_i and $K+G$ are the coefficients of PW, which are fully dependent on the particular kinetic energy, E_k:

$$\left(\frac{\hbar^2}{2m}\right) |K + G_C|^2 \tag{3.46}$$

The convergence of the expansion process is governed by equation (3.44), which determines the kinetic energy cutoff. The PW basis set is limited within a sphere in reciprocal space, as demonstrated in relation to E_{cut}. For all G values, the E_k remain $\leq$ to a specific E_{cut}, denoted as:

$$\left(\frac{\hbar^2}{2m}\right)|K+G_C|^2 < E_{cut} \tag{3.47}$$

The E_{cut} can be determined by increasing its magnitude up to the total energy converges, ensuring accuracy in calculations [129]. As the number of PWs increases, it becomes possible to describe various characteristics more efficiently and approach an infinitely large basis set. However, when introducing a finite E_{cut} to the discrete PW basis set, it becomes finite, potentially leading to some errors in total energy calculations. To minimize these errors and achieve good convergence, it is essential to employ a denser set of k-points. The required number of k-points relies on the system of interest, with metals typically requiring more k-points compared to semiconductors and insulators.

3.7.2 Pseudopotentials

The pseudopotential is a method employed to simplify the effects of the core electrons in an atom, which includes both the non-valence electrons and the atomic nucleus. It involves replacing the complex interactions of the core with an effective potential, known as the pseudopotential. The modification aims to incorporate an altered effective potential term into the Schrödinger equation, replacing the Coulombic potential term that typically accounts for the core electrons. The construction of pseudopotentials and pseudo wavefunctions ensures that crucial characteristics of real potentials and wavefunctions are preserved. This allows for accurate representation of important properties. As a result, the system then is separated into two regions: that is, the core region, where pseudo-waves and pseudo-potentials occupy, and the interstitial region, which represents delocalized states using a PW basis set. This division is demonstrated in Figure 3.1 [130]. In the pseudopotential generation, a cut-off radius (r_c) or core radius is defined. Then, the resulting pseudo-wavefunction and pseudo-potential should then reproduce the actual potential and

wavefunction outside the radius. The pseudopotential is denoted by:

$$V_{ps} = V_{loc} + \sum_{l,m} (V_l - V_{loc}) \hat{P}_{l,m} \tag{3.48}$$

where V_{loc} represents the arbitrary local potential and V_l is angular potential [131]. When

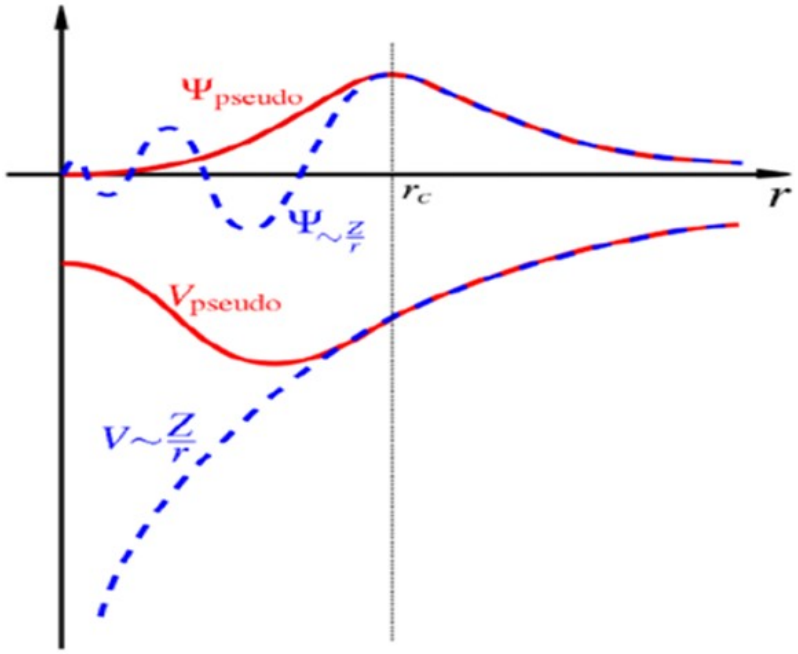


Figure 3.1: Pseudopotentials and pseudo wavefunctions [131].

$V_l = V_{loc}$, then the pseudo-potential is said to be local, and non-local pseudo-potential when they differ. For an isolated atom, pseudopotential is generated using all-electron DFT method. In the core region, true wavefunctions are first determined and adjusted to substitute the nodes with a pseudo wavefunction that is norm-conservation constrained. The pseudopotential is determined with a specific r_c using Schrödinger equation. Thus, in any chemical system, the resulting pseudopotentials can be applied to the specific atom. There are different types of pseudopotentials that can be used, namely, norm-conserving and ultrasoft. The requirements for norm-conserving pseudopotentials include achieving a precise correspondence between the real and pseudopotentials, charge densities, wave-functions, and squared amplitudes of pseudo-wavefunctions throughout the entire region of interest [132]. Norm-conserving pseudo-potentials are usually harder than ultra-soft pseudo-potentials. Ultra-soft schemes reduce pseudopotential hardness using some Fourier

coefficients and relax standard-conserving criteria in the core region [133]. Because of the soft nature of ultra-soft pseudopotentials, the E_{cut} is typically set to a lower value compared to what is specified in the norm-conserving pseudopotential case. The softness of a pseudopotential implies its capacity to facilitate the expansion of valence pseudo-wavefunctions using as few planewaves as possible [134]. Hard pseudopotentials are considered "hard" because they effectively shield the valence electrons from the nuclear charge in a relatively short distance.

3.7.3 K-point Sampling

The range of k-points where electronic states are permitted in the solid system is determined by the boundary constraints. The parameter, ρ of allowed k-points directly depends on the volume of the solid bulk system. The infinite numbers of electrons within the solid are accounted through an infinite number of k-points and only a finite number of electronic states are being filled at each k-point. The calculation of electronic wavefunctions for an infinite solid is simplified by the Bloch theorem, which states that electronic wavefunctions in a periodic crystal lattice can be expressed as the product of a periodic function and a plane wave. In the bulk system, an infinite amount of computations are theoretically required due to the contribution of occupied states at each k-point, in order to calculate the electronic potential. Regardless of the similarities of the electronic wavefunctions at very nearby k-points. This allows us to constitute wavefunctions over a range of k-space using wavefunctions from a single k-point. Consequently, computing the potential and determining the E_{tot} only requires considering electronic states at a finite amount of k-points.

By performing wavefunction calculations at specific sets of k-points, researchers have developed techniques to derive accurate exchange-correlation potentials from filled electronic bands. These methods, often involving Brillouin zone sampling schemes like Monkhorst and Pack, contribute to the accurate description of electronic interactions in materials. The two commonly used methods in DFT are those of Cohen and Chadi [135], and Monkhorst and Pack [136]. Calculating the electronic states at a relatively few k-points, these techniques allow one to determine the system's potential and E_{tot}. For example, to correctly

express the Fermi surface of a metallic system, the E_{tot} and electronic potential must be calculated employing a denser collection of k-points. However, when the k-points are increased to a denser k-space sampling in the BZ, the computational costs of executing the calculations increase. DFT codes employ a finite sampling of k-points to approximate these k-space integrals. By employing the least amount of k-points for a certain accuracy and lower the computing cost, special k-points schemes have been devised.

3.8 Cluster Expansion

Standard DFT methods may be used to handle systems with cells making up a few hundred atoms to determine total energies, forces, and other quantities with typical DFT precision. Furthermore, when describing the concentration-dependent thermodynamic properties of a multi component system one must sample the configuration space, which scales by 2^N for a binary system with N lattice sites. Even for relatively smaller unit cells or supercells, this is not possible in DFT. The CE is a method used for overcoming this configuration limitation and size while maintaining the accuracy of DFT. CE fits a set of elective cluster interaction energies (ECI) employing a set of DFT input structures. Cluster expansion is considered a valuable and commonly used method to explore structures that display substitutional disorder, specifically the crystalline materials in which some sites can be inhabited by more than one kind of element [123-124].

3.8.1 Theoretical Background

The Hamiltonian of a material with atomic configuration or atomic distribution on a particular lattice is generated using an Ising like ansatz on a fictious fixed lattice. For example, in an $A_{1-x}B_x$ system, if i represents type A atom, then the spin value, $S_i = -1$, and if i represents type B atom, then the spin value, $S_i = +1$. The term 'spin' is employed as an analogy for the occupation variable in the Ising-like ansatz for the cluster expansion. The binary formalism can be expanded to ternary, quaternary, and larger multi-component system using Chebychev polynomials as orthogonal basis [137]. The energy, $E(\sigma)$ associ-

ated with σ that can be explained using an Ising-expansion of cluster interaction and their corresponding interaction energies:

$$E(\sigma) = J_0 + \sum_i J_i S_i(\sigma) + \sum_{j<i} J_{ij} S_i(\sigma) S_j(\sigma) + \sum_{k<j<i} J_{ijk} S_i(\sigma) S_j(\sigma) S_k(\sigma) + \ldots \quad (3.49)$$

where J represents ECI's and J_0 is an independent contribution of configuration. The term sum over $J_i j S_i(\sigma)$, which is site independent system's energy depending on the concentration of an atom. All possible pair-figures in the system are included in the summation over $J_i S_i(\sigma) S_j(\sigma)$, while higher order terms such as triplets, quadruplets, reflect many-body interaction with an atomic configuration or atomic distributed on a particular lattice is generated. In order to find a more compact form of equation 3.49, one can introduce a $\bar{\Pi}_G(\sigma)$, which is a correlation function for each and every type of symmetrical corresponds figure G:

$$\bar{\Pi}_G(\sigma) = \frac{1}{ND_G} \sum_g S_{i_1}(\sigma) S_{i_2}(\sigma) \ldots S_{i_m}(\sigma) \quad (3.50)$$

where D_G denotes the number of class G figures per site. The letter m represents the number of sites related to figure g and the index g runs over the ND_G figures in class G. Therefore, equation (3.50) can be expressed as:

$$E(\sigma) = \sum_G D_G \bar{\Pi}_G(\sigma) J_G \quad (3.51)$$

with J_G as the ECI for figure class G. It is important to keep in mind that the ECI's are fitting parameters generated by fitting $E_{CE}(\sigma)$ to values derived using a technique like DFT and have no direct physical significance. The property that the CE is applied to, such as an elastic property, will determine the physical nature of the ECIs.

3.8.2 UNiversal CLuster Expansion

Universal Cluster Expansion (UNCLE) is a computer program-package designed to reduce the cluster expansion's sensitivity to individual inputs and enable the CE applicable beyond simple alloys, particularly bulk binary systems [138]. UNCLE employs a CVS to describe

the average error of the CE prediction compared to actual DFT. The CVS is determined as:

$$\mathrm{CVS} = \sqrt{\frac{1}{nN_{\mathrm{pred}}} \sum_{n} \sum_{N_{\mathrm{pred}}} \left[\Delta H_{DFT}(\sigma) - \Delta H_{CE}(\sigma)\right]^2}, \tag{3.52}$$

However, it is useless to have a set of N_g figures and associated ECIs that can only precisely replicate the energies of the input systems. Instead, the target is to acquire a set of N_g figures with corresponding ECIs that can precisely forecast the energies of structures that were not included in the fit. To anticipate the energy of N_{pred} the excluded, UNCLE fits the ECIs for each set independently. The CVS evaluates a collection of ECIs' prediction ability as a result. A pre-defined training set of genetic algorithm (GA) approach is used to search the best ECIs and is summarized in the next section.

3.8.2.1 Genetic Algorithm

The genetic algorithm can be used to choose clusters from a set of training structures $\{\sigma_1, \ldots, \sigma_m\}$ and their corresponding energy values $E = (E_1, \ldots, E_m)^T$. Its basic principle is illustrated in Figure 3.2. This process is stochastic, meaning that repeating the algorithm on similar training set can yield slightly different outcomes. Even though the fluctuations is not significant after the convergence of the CE has occurred. To evaluate the fitness of the selected clusters, one needs to use the CVS leave-one-out. Leave-one-out cross-validation provides a robust assessment of the model's predictive power because it evaluates the model on every data point in the dataset. This involves removing one structure at a time from the training set and use the $N-1$ structures remaining in a least-squares fit for the evaluation of ECI energies, J. These J are then employed to make a prediction about the energy of the structures that were removed and comparing the actual J value. This process is repeated for all N structures in the training set. Then the standard deviation (SD) of the predicted ECI energies is evaluated against the actual energies.

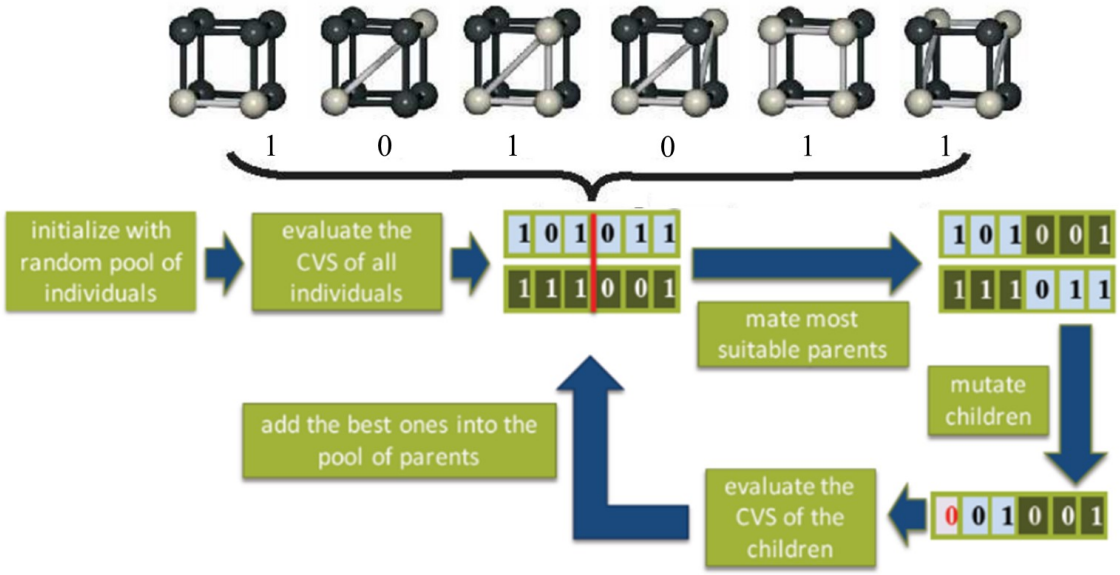


Figure 3.2: Illustration of genetic algorithm approach [139].

3.8.2.2 Iterative Optimization of the Training Set

The method used to select structures for the training set differs depending on whether the model has miscible constituents or miscibility gap. To differentiate between these two types of models, heats of formation, $\Delta H_f(\sigma)$ are calculated for every structure in the training set and expressed as:

$$\Delta H_f(\sigma) = \frac{E_{DFT}(\sigma) - \sum n_i(\sigma) E^i_{DFT}}{\sum n_i(\sigma)} \tag{3.53}$$

where $E_{DFT}(\sigma)$ defines DFT E_{tot} of the system σ, $n_i(\sigma)$ represents the number of atomic species i in the σ, and E^i_{DFT} represents the pure phase density functional theory E_{tot} of atomic species i. The summation includes all sorts of atoms comprised in the system σ. For systems with miscible constituents, the selected materials have negative $\Delta H_f(\sigma)$, indicating that the systems are ordered and thermodynamically stable. On the other hand, the ordered structures with a positive heat of formation have a miscibility gap and they are thermodynamically unstable. Structures with a miscibility gap undergoes a phase separation when exposed to external conditions such as temperature and pressure.

Miscible Constituents

Miscible constituents refer to a type of model where the different atomic species or compounds can mix together homogeneously to form a single phase. When constructing a CE for a system with miscible constituents as illustrated in Figure 3.3, the selection of structures for the training set is performed differently than for models with a miscibility gap. The cluster expansion prioritizes the most important structures, which are those with energies that are not far from the groundstate energy, meaning structures with the least heats of formation at a particular concentration. The cluster expansion predicts the most preferred structures that are not already included in the training set, and these are iteratively included in the training set. The process is repeated until there are no new predicted structures that are more preferred than all those that are already in the set. This process continues until the cluster expansion converges, and all the thermodynamically stable structures from those considered are identified.

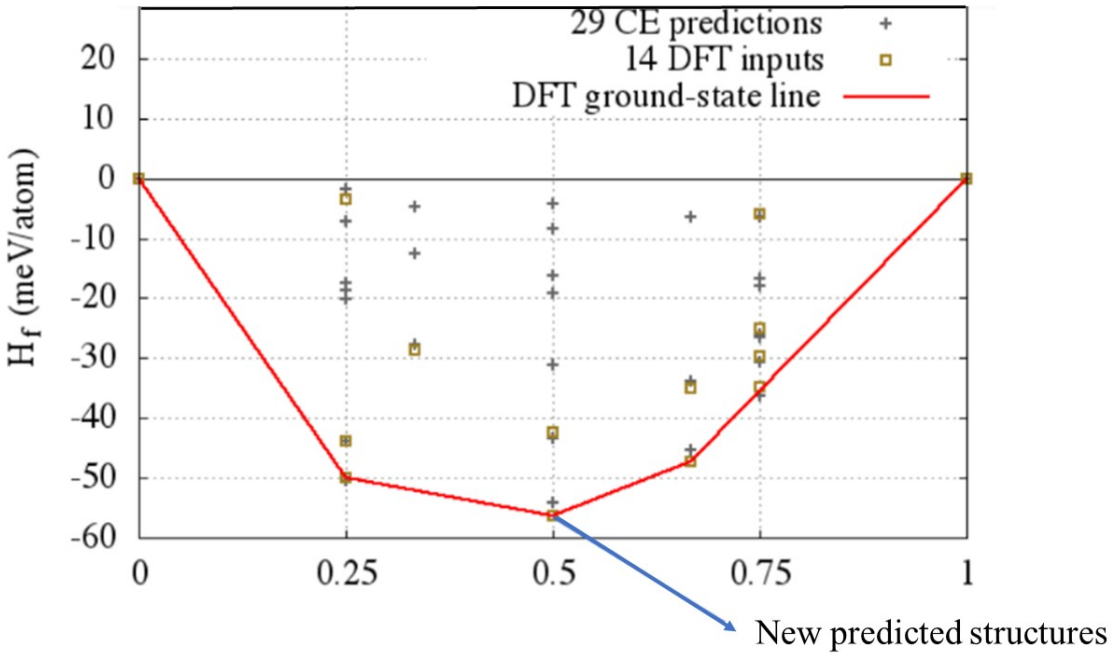


Figure 3.3: Binary groundstate diagram illustrating miscible constituent [139].

Miscibility Gap

If the model displays a miscibility gap, it means that there are no stable ordered structural configurations other than the two pure phases, however all structures are equally important

for the cluster expansion. The objective is to enhance the quality of the CE for all considered materials irrespective of their energy of formation by selecting appropriate structures to add to the training set. Evaluating the accuracy of the CE in predicting structure energies involves utilizing the stochastic nature of the GA approach. Numerous CE calculations are determined using the same training set, and the predicted energies of all compounds are compared across the cluster expansions. The SD of the predicted energies is calculated, and structures with higher SD indicate poor performance of the cluster expansion in modeling those structures. These structures are then progressively incorporated into the training set, iteratively improving the accuracy of the CE. Similarly, an example of predicting structures that are ordered but not thermodynamically stable is illustrated in Figure 3.4

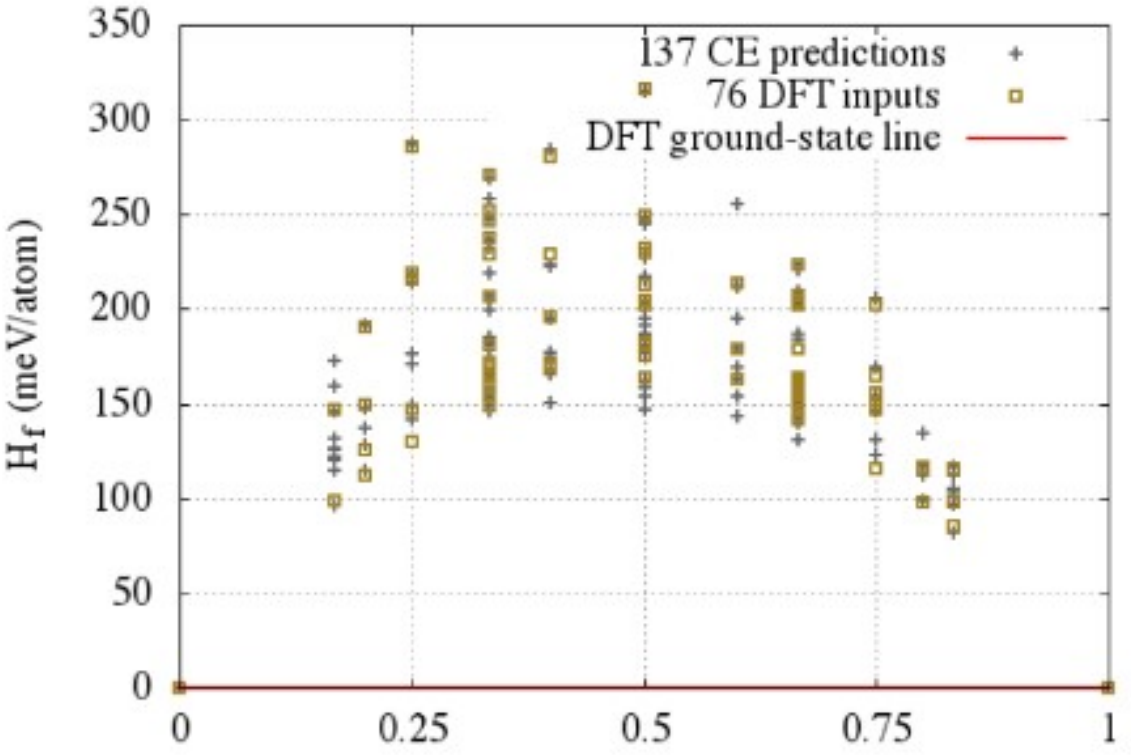


Figure 3.4: Binary groundstate diagram illustrating miscibility gap [139].

3.8.2.3 Monte Carlo

A thermodynamical description of the system can be provided by statistically sampling the configuration space using the ECIs from the CE and a Monte Carlo (MC) technique. In principle, MC is based on a biased random walk of a stationary Markov chain, where the

next state σ_β of the system is only dependent on the previous state σ_α. The probability for a state σ_β is given by:

$$p_\alpha = \frac{1}{Z} e^{\left(-\frac{E(\sigma_\alpha)}{k_B T}\right)} \tag{3.54}$$

where $E(\sigma_\alpha)$ denotes the energy of state σ_α, k_B denotes the Boltzmann constant as always, T denotes the temperature and Z denotes the grand partition function. Given that the stationary Markov chain process is reversible and adheres to the detailed balance principle [105], it follows that the probability of changing from state σ_α to a different state σ_β is the same for the reverse process. Therefore,

$$p_\alpha p_{\alpha\beta} = p_\beta p_{\beta\alpha}, \tag{3.55}$$

where p_α and p_β for the probabilities of the respective states. The probability of transition from one phase to the other is given by $p_{\alpha\beta}$ and $p_{\beta\alpha}$.

3.9 Calculated Properties

3.9.1 Electronic Properties

To gain insights on the electronic properties and characteristics of atomic bonds of doped $CsPbI_3$ perovskite materials, we calculated their band structure, total density of states (TDOS) and partial density of states (PDOS). The descriptions of these properties are summarized in the next subsections 3.9.1.1 - 3.9.1.3.

3.9.1.1 Band Structure

The eigenvalues connected to the valence band (VB) and conduction band (CB) along certain directions in the BZ of a given crystal structure are revealed by the electronic band structure of a solid. Finding the energy band gap, (E_g) (also referred to as band gap), defined as the difference between the energies of the upper VB and the lower CB, is one of the most crucial steps in computing the electronic band structure because it can provide insight into potential applications for optical devices. The K-S equations can be resolved

to produce energy band structure diagrams and DOS using the energy gap determined from the Kohn-Sham eigenvalues [139]. DFT accurately predicts lattice parameters and equilibrium atomic positions depending on the exchange correlation functional employed, but it is unable to predict band gaps and excitation energies. It is either underestimated or overestimated.

3.9.1.2 Density of States

The electronic DOS is an essential concept in quantum mechanics and solid-state physics that gives details about the distribution of energy states for a material [110]. Essentially, DOS denoted by $g(\varepsilon)$, represents the amount of electronic states within a volume per unit energy range. By combining the energies of all states in that range, $g(\varepsilon)$ in the energy range $(\varepsilon, \varepsilon + d\varepsilon)$ may be computed and expressed as [140]:

$$g(\varepsilon) = \frac{2}{(2\pi)^3} \sum_i \int \mathrm{d}\mathbf{k} \delta \left(\varepsilon - \varepsilon_{i,\mathbf{k}}\right) \tag{3.56}$$

where i represents the band index. Usually, the integral is calculated over all k-points within the BZ, the contributions represented by spin up and spin down are favored by inclusion of the number 2, and $\delta(\varepsilon - \varepsilon_{i,\mathbf{k}})$ represents a Dirac delta function. It is important to illustrate the individual atom's proportionate impact on the TDOS, which can be achieved by calculating the PDOS for individual atoms. DOS plots are used to depict the contributions of s, p, d or f states from various elements that result in the peaks within the CB and VB at distinct energy levels. Spectral peaks in the TDOS plots illustrate the cumulative contributions from all participating atoms, while peaks in the PDOS plots highlight the specific contributions of individual atomic orbitals. Additionally, DOS plots serve the purpose of observing the change in the electronic structure when impurities are introduced into crystals, allowing for a comparison between crystals with impurities and those in their pure form.

3.9.1.3 Bond Population Analysis

The electronic distribution in an atomic or molecular system can be described using the Mulliken populations. Sanchez-Portail *et al.*[141] described a method that is used in the CASTEP code to determine the analysis of Mulliken population employing PW states projection on a localized basis. The estimated partial atomic charge for molecular or atomic orbitals to a particular atom, A, is calculated using the equation:

$$Q(A) = \sum_k w_k \sum_u \sum_v 2P_{uv}(k)2S_{uv}(k) \tag{3.57}$$

having:

$$S_{vu}(k) = \langle \phi^u(k) \mid \phi^v(k) \rangle : \text{ represents the overlap matrix} \tag{3.58}$$

$$P_{uv}(k) = \langle \phi^u(k) | \rho(k) | \phi^v(k) \rangle : \text{ is the matrix element of the density matrix} \tag{3.59}$$

$$W_{\alpha u}(k) = \langle \psi^\alpha(k) \mid \phi^u(k) \rangle \langle \phi^\alpha(k) \mid \psi^\alpha(k) \rangle : \text{ is the band weight } \alpha \text{ on the orbital u.} \tag{3.60}$$

Bond population analysis is a valuable tool for understanding chemical bonding, but its application should be approached with an awareness of its limitations and potential sources of error. Some methods used in bond population analysis may neglect electron correlation effects, leading to inaccuracies in predicting bond properties.

3.9.2 Optical Properties

In solids state physics, optical properties is a phenomena related to the interaction of materials with electromagnetic radiation in the optical frequency range. The study of defects, band structures, impurity levels, excitations, lattice vibration, and magnetic excitation, are determined using optical properties analysis [142]. Some of the key optical properties include optical absorption, conductivity, dielectric function, refractive index, loss function, etc. The frequency dependent dielectric function is used to determine the optical and infer

the electronic properties of materials. As a complex quantity it is defined as:

$$\varepsilon(\omega) = \varepsilon_1(\omega) + i\varepsilon_2(\omega) \tag{3.61}$$

where $\varepsilon_1(\omega)$ denotes the real part and $\varepsilon_2(\omega)$ denotes the imaginary part of the dielectric function, $\varepsilon(\omega)$. The imaginary part of dielectric function, $\varepsilon_2(\omega)$ is given by:

$$\varepsilon_2(\omega) = \frac{8}{3\pi\omega^2} \sum_{nn'} \int |P_{nn'}(l)|^2 \frac{ds_l}{\omega_{nn'}(l)} \tag{3.62}$$

$P_{nn\prime}(l)$ are the elements of the dipolar matrix within the first state $|nk\rangle$ with eigen energy $E_n(l)$ and the final state, $n'l$ with eigen energy $E_{n\prime}(l)$:

$$\omega_{nn'}(l) = E_n(l) - E_{n'}(l) \tag{3.63}$$

s_l denotes an energy-efficient surface expressed by :

$$s_l = \{l, \omega_{nn'}(l) = \omega\} \tag{3.64}$$

Using the Kramers-Kronig transformation equation related to the dielectric function, the parameter ε_1 can be determined via $\varepsilon_2(\omega)$. The Kramers-Kronig transformation is based on the principle of causality, ensuring that the real and imaginary parts of the dielectric function are consistent with physical reality. This makes the results physically interpretable and ensures that the material response is causal. However, there are situations where applying the Kramers-Kronig transformation can be challenging or may lead to inaccurate results:
The Kramers-Kronig transformation assumes linearity in the response of the material. In cases where the material exhibits strong non-linear behavior, the transformation may not provide accurate results.
For complex materials with multiple electronic transitions or intricate structures, applying the Kramers-Kronig transformation can be challenging, and simplified models may not capture the full complexity of the dielectric function. These real and imaginary parts of the dielectric function, can be used to derive other optical properties i.e., refractive index,

absorption, extinction coefficient, conductivity and reflectivity using the following expressions:

$$n(\omega) = \frac{1}{\sqrt{2}} \left(\sqrt{\varepsilon_1^2(\omega) + \varepsilon_2^2(\omega)} + \varepsilon_1(\omega) \right)^{\frac{1}{2}} \tag{3.65}$$

$$\alpha(\omega) = \sqrt{2\omega} \left(\sqrt{\varepsilon_1^2(\omega) + \varepsilon_2^2(\omega)} - \varepsilon_1(\omega) \right)^{\frac{1}{2}} \tag{3.66}$$

$$K(\omega) = \frac{1}{\sqrt{2}} \left(\sqrt{\varepsilon_1^2(\omega) + \varepsilon_2^2(\omega)} - \varepsilon_1(\omega) \right)^{\frac{1}{2}} \tag{3.67}$$

$$\sigma(\omega) = -\frac{i\omega}{4\pi} \varepsilon(\omega) \tag{3.68}$$

$$R(\omega) = \left| \frac{\sqrt{\varepsilon(\omega) - 1}}{\sqrt{\varepsilon(\omega) + 1}} \right|^2 \tag{3.69}$$

3.9.3 Elastic Properties

The elastic constants, the modulus (bulk (B), shear (G) and Young (Y)), the ratios (Pugh (B/G) and Poisson v), elastic anisotropy provide a comprehensive understanding of a material's mechanical behavior. In DFT calculations, elastic constants can be computed using two different methods, namely; the energy-strain and stress-strain approaches. The elastic constants matrix, often denoted as C, is a mathematical representation of the linear relationship between strain and stress in the compound under the assumption of small deformations. This matrix is a fundamental concept in the study of elastic behavior. The elastic constants matrix relates the six independent components of stress ($\sigma_{xx}, \sigma_{yy}, \sigma_{zz}, \sigma_{xy}$ σ_{yz}, and σ_{zx}) to the six independent components of strain ($\varepsilon_{xx}, \varepsilon_{yy}, \varepsilon_{zz}, \varepsilon_{xy}, \varepsilon_{yz}$, and ε_{zx}) for an isotropic material. For anisotropic materials, the number of independent constants may be higher.

The relationship is given by Hooke's Law:

$$\begin{bmatrix} \sigma_{xx} \\ \sigma_{yy} \\ \sigma_{zz} \\ \sigma_{xy} \\ \sigma_{yz} \\ \sigma_{zx} \end{bmatrix} = \begin{bmatrix} C_{11} & C_{12} & C_{13} & C_{14} & C_{15} & C_{16} \\ C_{21} & C_{22} & C_{23} & C_{24} & C_{25} & C_{26} \\ C_{31} & C_{32} & C_{33} & C_{34} & C_{35} & C_{36} \\ C_{41} & C_{42} & C_{43} & C_{44} & C_{45} & C_{46} \\ C_{51} & C_{52} & C_{53} & C_{54} & C_{55} & C_{56} \\ C_{61} & C_{62} & C_{63} & C_{64} & C_{65} & C_{66} \end{bmatrix} \begin{bmatrix} \varepsilon_{xx} \\ \varepsilon_{yy} \\ \varepsilon_{zz} \\ 2\varepsilon_{xy} \\ 2\varepsilon_{yz} \\ 2\varepsilon_{zx} \end{bmatrix} \tag{3.70}$$

Here, C_{ij} are the elastic constants representing the stiffness of the material in different directions. The matrix C is symmetric (i.e., $C_{ij} = C_{ji}$) for isotropic materials. In this study, the elastic constants are computed based on Hooke's law from the linear relationship of the computed stress-strain functions. The elastic strain energy density plays a significant role in these calculations. For a cubic phase of $CsPbI_3$, these are independent constants that are used, namely C_{11}, C_{12}, and C_{44}. Using two types of strains (ε_1 and ε_4) may generate stresses related to the constants C_{11}, C_{12}, and C_{44}, resulting in an effective approach for determining cubic elastic constants [143]. The criteria below determines the cubic mechanical stability [144] and expressed as:

$$C_{44} > 0, C_{11} > |C_{12}| \text{ and } C_{11} + 2C_{12} > 0 \tag{3.71}$$

The elastic moduli of polycrystalline materials were computed by Hill using the averaging procedures of Reuss (lower bound) and Voigt (upper bound) based on C_{11}, C_{12}, and C_{44} constants [145]. The mechanical parameters for Voigt's modulus and Reuss's modulus are given as:

$$B_V = B_R = \frac{C_{11} + 2C_{12}}{3} \tag{3.72}$$

$$G_V = \frac{C_{11} - C_{12} + 3C_{44}}{5} \tag{3.73}$$

$$G_R = \frac{5C_{44}(C_{11} - C_{12})}{4C_{44} + 3(C_{11} - C_{12})} \tag{3.74}$$

For tetragonal structures, there are six independent constants, namely; C_{11}, C_{12}, C_{13}, C_{33}, C_{44}, and C_{66}. The corresponding mechanical stability criteria is expressed as:

$$C_{44} > 0, C_{66} > 0, , C_{11} > |C_{12}| \text{ and } C_{11} + C_{12} - \frac{2C_{13}^2}{C_{33}} > 0 \tag{3.75}$$

These three approximation models which are Reuss, Hill, and Voigt may all be used to determine the elasticity of the materials. The maximum and minimum values of the tetragonal $CsPbI_3$ elastic modulus are derived from both of these calculations, Reuss and Hill approximations. In this study, the correction value of the above mentioned values were determined using the Hill approximation model for the Voigt approximation [146] and is given by:

$$B_V = \frac{1}{9}\left[(2C_{11} + 4C_{13} + C_{33})\right] \tag{3.76}$$

$$G_V = \frac{1}{15}(C_{11} + C_{22} + C_{33}) - \frac{1}{15}(C_{12} + C_{13} + C_{23}) + \frac{1}{5}(C_{44} + C_{55} + C_{66}) \tag{3.77}$$

As well as Reuss approximation:

$$B_R = \frac{\left[(C_{11} + C_{22})C_{33} - 4C_{13}^2\right]}{(C_{11} + C_{12} + 2C_{33} + 4C_{13})} \tag{3.78}$$

$$G_R = \frac{5C_{44}C_{66}\left[(C_{11} + C_{12})C_{33} - 2C_{13}^2\right]}{2\left[3C_{44}C_{66} + \left\{(C_{11} + C_{12})C_{33} - 2C_{13}^2\right\}(C_{44} + C_{66}\right]} \tag{3.79}$$

The are nine elastic constants,namely; C_{11}, C_{12}, C_{13}, C_{22}, C_{23}, C_{33}, C_{44}, C_{55}, and C_{66} used to determine the mechanical stability of an orthorhombic system. For Born mechanical stability criteria [147] these elastic constants used are calculated as follows:

$$\begin{gathered} C_{ii} > 0; i = 1 - 6 \\ C_{ii} + C_{jj} - 2C_{ij} > 0; i, j = 1, 2, 3 \\ C_{11} + C_{22} + C_{33} + 2(C_{12} + C_{13} + C_{23}) > 0 \end{gathered} \tag{3.80}$$

To calculate the elastic properties of a compound that has an orthorhombic phase, the Voigt B and G moduli are given by the relation:

$$B_V = \frac{1}{9}[C_{11}+C_{22}+C_{33}]+\frac{2}{9}[C_{12}+C_{13}+C_{23}] \tag{3.81}$$

$$G_V = \frac{1}{15}[C_{11}+C_{22}+C_{33}-C_{12}-C_{13}-C_{23}]+\frac{3}{5}[C_{44}+C_{55}+C_{66}] \tag{3.82}$$

The bulk (B_R) and shear (G_R) Reuss modulus can be written as:

$$B_R = \frac{1}{(C_{11}+C_{22}+C_{33})+2(C_{12}+C_{13}+C_{23})} \tag{3.83}$$

$$G_R = \frac{15}{4(C_{11}+C_{22}+C_{33})-4(C_{12}+C_{13}+C_{23})+3(C_{44}+C_{55}+C_{66})} \tag{3.84}$$

Similarly, for the Hill approximation:

$$B_H \frac{(B_V+B_R)}{2} \tag{3.85}$$

$$G_H \frac{(G_V+G_R)}{2} \tag{3.86}$$

From the calculated B and G moduli, v and Y are determined using the relations:

$$Y = \frac{9BG}{3(B+G)} \tag{3.87}$$

$$v = \frac{3B-2G)}{2(3B+G)} \tag{3.88}$$

The modulus Y, determines the material's stiffness and can be expressed as stress-strain ratio. The greater the value of Young modulus indicates a stiffer material. The parameter, v is the quotient of transverse contraction strain to longitudinal expansion strain during elongation, which indicates the material's resistance to shear forces. A greater Poisson's ratio indicates more ductility at low temperatures in crystalline materials. In contrast, B evaluates a material's resistance to pressure-induced volume changes. The shear modulus represents the isotropic behavior under shearing forces. Understanding and quantifying

these properties allow for the assessment of a material's behavior under different mechanical conditions. They provide crucial information for designing materials with desired characteristics, predicting their mechanical response, and ensuring their suitability for specific applications in technology and engineering. In this study, first principle quantum mechanical method was used to predict mechanical properties of doped $CsPbI_3$ perovskites. The three anisotropy ratios, A_1, A_2 and A_3 for an isotropic monoclinic structures must be equal to unity [148]. Crystals with low symmetry exhibit significant elastic anisotropy [149, 150]. The shear anisotropic factors along various planes quantify the degree of elastic anisotropy of atomic bonding in various directions. For non-cubic phases, the shear anisotropic factors are calculated as follows:

$$(100) : A_1 = \frac{4C_{44}}{C_{11} + C_{33} - 2C_{13}} \tag{3.89}$$

$$(010) : A_2 = \frac{4C_{55}}{C_{22} + C_{33} - 2C_{23}} \tag{3.90}$$

$$(001) : A_3 = \frac{4C_{66}}{C_{11} + C_{22} - 2C_{12}} \tag{3.91}$$

A represent the elastic anisotropy, and is importance in the field of engineering as it correlates strongly with the potential occurrence of microcracks in materials [151]. When a material exhibits complete isotropy, the value of A is equal to 1. However, values lower or higher than 1 indicate varying degrees of elastic anisotropy. Understanding elastic anisotropy is crucial for assessing the susceptibility of materials to microcrack formation.

3.9.4 Thermodynamic Properties

The Debye temperature holds significant importance as a thermodynamic parameter, closely tied to various thermophysical properties of solids. These properties encompass thermal expansion, vibrational entropy, specific heat, hardness, sound velocities, and melting temperature [152]. The Debye temperature, denoted as θ_D can be determined through the

average sound velocity (v_s) using the analytical expression [153]:

$$\theta_D = \frac{\hbar}{k_B}\left(\frac{3n}{4\pi v_a}\right)^{1/3} v_s \tag{3.92}$$

where $\hbar$ denotes the Planck's constant, n is the number of atoms in the molecule, v_a represents the atomic volume and k_B represents the Boltzmann's constant. In polycrystalline systems, v_s is evaluated using the analytical expression [154]:

$$v_s = \left[\frac{1}{3}\left(\frac{2}{v_t^3} + \frac{1}{v_l^3}\right)\right]^{-1/3} \tag{3.93}$$

where v_l denotes the mean longitudinal and v_t denotes the transverse sound velocities. The sound velocities can be related to B and G modulus from Navier's equations and ρ is the density, using the relation:

$$v_l = \left(\frac{3B+4G}{3\rho}\right)^{1/2} \text{ and } v_t = \left(\frac{G}{\rho}\right)^{1/2} \tag{3.94}$$

3.10 Computer Codes

3.10.1 VASP Code

The Vienna Ab initio Simulation (VASP) is a computational tool designed for studying electronic structures in solids, interfaces, and surfaces. The code performs ab initio quantum mechanical calculations using a planewave basis set. The underlying methodology implimented in the code is capable of performing post DFT exchange correlations as well as density functional theory [155]. Pseudopotentials play a key role in representing the electron-ion interactions in these simulations.

3.10.2 UNCLE Code

UNiversal CLuster Expansion is a new program-package designed to reduce the cluster expansion's sensitivity to individual inputs and enable the cluster expansion applicable to

systems other than basic bulk binary ones [138]. The theory behind this code has been discussed in section (3.8.2).

4

Mixed Halide $CsPbI_{3-x}Br_x$

4.1 Introduction

Mixed-halide perovskites $ABX_{3-x}Y_x$ (X and Y = F, Cl, Br, I) have been found to enhance the fundamental properties (i.e. stability, carrier mobility, and band gap tunability) of inorganic perovskites solar cells [24]. Several studies reported the partial substitution of the I^- ion with the smaller percentage of Br^- ion increases the Goldschmidt tolerance factor and subsequently enhance the stability of the cubic structure even at an ambient temperature [97, 98]. Thus, partial substitution is considered a feasible solution to enhance $CsPbI_3$ phase stability. Noh *et al*. reported on the tuned energy band gap of $ABI_{3-x}Br_x$ perovskites by substitution the composition of I^- and Br^- ions [32]. The band gap energy and lattice parameters of $MAPb(I_{1x}Br_x)_3$ exhibit linear relationships with Br content (x). The optical

absorption resulting from band gap engineering can be precisely adjusted to cover almost the entire visible spectrum. Starting with $CsPbBr_3$, Rajeswarapanichamy *et al.* reported the narrow band gap of $CsPbBr_{3-x}I_x$ (x = 0, 1, 2, 3) mixed Br/I halide systems by using GGA approximation [99]. There are limited reports in the literature on the effects of the mixed halogen on properties of inorganic perovskites. In this chapter, a comparative study of structural, opto-electronic, elastic, and thermodynamic properties mixed halide perovskites, $CsPbI_3$, $CsPbI_2Br$, $CsPbIBr_2$, and $CsPbBr_3$. The studied was investigated using three functionals; GGA-PBE, SCAN meta-GGA, and LDA within the first-principles density functional theory. The cubic phase of $CsPbI_3$ used in this study is more symmetric and generally more stable at high temperatures compared to the orthorhombic or tetragonal phases. This high-temperature stability can lead to better performance in practical operating conditions. There are no literature reports on investigation of the properties of using complex exchange correlation functionals incorporated in SCAN meta-GGA.

4.2 Computational Details

The calculations were performed using DFT within the pseudopotential projector-augmented wave [100] technique as implemented in the Vienna Ab initio Simulation Package [101-104]. Three different exchange-correlation functionals, namely, GGA proposed by Perdew, Burke, and Ernzerhof [105], SCAN [106], and LDA [107] were used in the calculations of all the properties. Unlike GGA and LDA, the SCAN meta-GGA introduces the kinetic energy density dependence. SCAN is the first functional to satisfy every known constraints on the exchange correlation functional at the semi local level. It effectively constructs the kinetic energy density in the form of a dimensionless variable that recognizes all types of orbital overlap in its design. The cut-off energy used was 500 eV. The Brillouin-zone integrations for geometry optimization calculations was performed using Monkhorst-Pack 6 x 6 x 6 k-mesh and for density of states and optical properties 11 x 11 x 11 k-mesh was used for all the systems. The total energy convergence threshold was set at 10^{-6} eV/atom. The crystal lattices and atomic coordinates were considered fully optimised

when the Hellmann-Feynman forces were smaller than 10^{-4} eV/ Å through the conjugate-gradient algorithm. The cubic structure was used to determine the lattice parameters and the physical properties of $CsPbI_3$, $CsPbI_2Br$, $CsPbIBr_2$, and $CsPbBr_3$. The compounds were relaxed with respect to both atomic positions and lattice parameters. Both the crystal lattices and atomic positions were fully optimized. Thus, both the crystal lattices and atomic positions were fully optimized while applying topotactic approach to keep the cell shape unchanged.

4.3 Structural Properties

The cubic polyhedron crystal structure of $CsPbI_3$ is illustrated in Figure 4.1, visualized using VESTA software [34]. The mixed halides $CsPbI_{3-x}Br_x$ (x = 1, 2, 3) perovskites were derived from the $CsPbI_3$ parent structure by replacing the I^- ion with the Br^- ion.

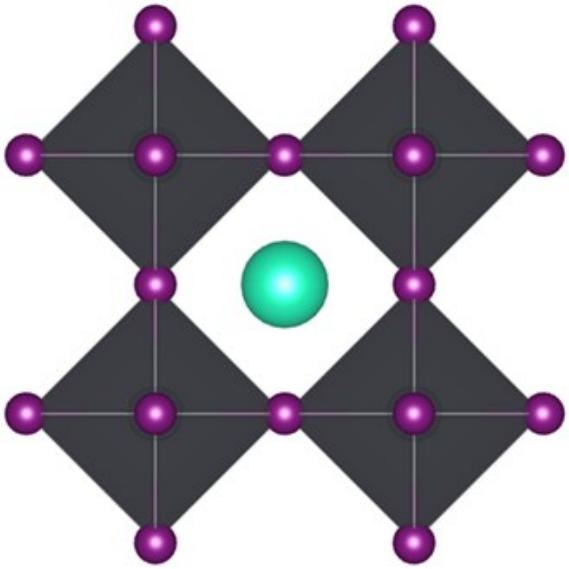


Figure 4.1: The constructed cubic polyhedron crystal structure of $CsPbI_3$. The perovskites $CsPbI_2Br$, $CsPbIBr_2$, and $CsPbBr_3$ were constructed by replacing the I^- ion with the Br^- ion.

The structural parameters were calculated using GGA-PBE, SCAN meta-GGA, and LDA functionals. Table 4.1 summarizes the calculated structural parameters and energy band gaps for $CsPbI_{3-x}Br_x$ (x = 1, 2, 3) with the previously reported experimental and theoretical results. The calculated lattice parameters agree with the theoretical and experi-

mental reported values from the literature. For $CsPbI_3$, the lattice constant obtained using SCAN is 6.290 Å, which is exactly the same as the experimental value of 6.29 Å, while GGA-PBE overestimated the lattice constant of 6.380 Å and LDA underestimated the lattice constant of 6.135 Å [35]. This demonstrates the accuracy of the DFT calculations with other previously reported theoretical values [14, 34]. For doped systems, the calculated results show that the cell volume and lattice constant, decreased when the I^- ion in $CsPbI_3$ was substituted by the Br ion ($CsPbBr_3$), as illustrated in Table 4.1. This is due to the change in the ionic radius of the halide ions from I^- to Br^-, as well as the change in ionic charges. Thus, when I^- ion with a relatively larger ionic radius (2.20) is replaced by Br^- ion with a smaller ionic radius (1.96), the volume of the unit cell decreases and this associated contraction is attributed to the size of the Pb-X bond, where X is either I^-, Br^-. For $CsPbBr_3$, the lattice constant obtained using SCAN is 5.900 Å which differs marginally from the experimental value of 5.874 Å [36] and the theoretical value of 5.99 Å [25].

Table 4.1: Calculated lattice constant, unit cell volume and energy band gap for $CsPbI_3$, $CsPbI_2Br$, $CsPbIBr_2$, and $CsPbBr_3$ compounds obtained using three functionals compared with experimental and other calculated theoretical values.

	$CsPbI_3$			$CsPbI_2Br$			$CsPbIBr_2$			$CsPbBr_3$		
Functional	GGA	SCAN	LDA	GGA	SCAN	LDA	GGA	SCAN	LDA	GGA	SCAN	LDA
Lattice constant (Å)	6.398	6.290	6.140	6.272	6.271	6.176	6.148	6.050	6.158	5.996	5.900	5.771
Exp	6.29 [46]									5.874 [29]		
Cal	6.38 [156]			6.2628 [157]			6.132 [157]			5.99 [158]		5.77 [159]
Volume ($Å^3$)	261.86	249.85	231.51	246.78	234.77	235.58	232.42	221.47	206.82	215.59	206.10	192.39
Cal.		250.12 [46]								216.80 [160]		192.33 [160]
Band gap (eV)	1.33	1.449	0.960	1.396	1.47	0.974	1.533	1.588	0.993	1.776	1.876	1.137
Exp.	1.73 [58]									2.30 [28]		
Cal.	1.307 [157]			1.365 [157]			1.471 [157]			1.75 [161]		1.59 [160]

4.4 Electronic Properties

4.4.1 Band Structure

The electronic band structures are measured along the high-symmetry directions $R-X-\Gamma-M-R-\Gamma$ for both $CsPbI_3$, $CsPbI_2Br$, $CsPbIBr_2$, and $CsPbBr_3$ using GGA-PBE, SCAN, and LDA functionals as depicted in Figure 4.2. The VBM and CBM are situated at the same Brillouin zone's point R for $CsPbI_3$,, and $CsPbBr_3$ and X point for $CsPbI_2Br$, and $CsPbIBr_2$ implying that all these perovskites are direct-band semiconductors. The horizontal red dotted line at zero energy shows the Fermi level (E_F). From the values in Table 4.1 and band structure plots in Figure 4.2, it is evident that the energy band gap increased when the I^- ion was substituted with the Br^- ion as also reported by Rajeswarapalanichamy *et al* [157]. For example, in the case of SCAN meta-GGA exchange correlation functional, energy band gap increased in this order: 1.449 eV> 1.470 eV> 1.588 eV> 1.876 eV for $CsPbI_3$, $CsPbI_2Br$, $CsPbBr_2I$, and $CsPbBr_3$, respectively. The differences in the ionic radii of Br and I in the mixed halide perovskites, as well as the hybridization propensity of the Pb 6s and halide (Br and I) 5p states, might explain this behaviour. All the functionals underesmated the bandgap compared to the experimental values illustrated in Table 4.1. GGA results are comparable with the previous theoretical reports. The band gap energy of these metal-halide perovskites may be adjusted by altering the halogen content, making them excellent materials for solar cell applications.

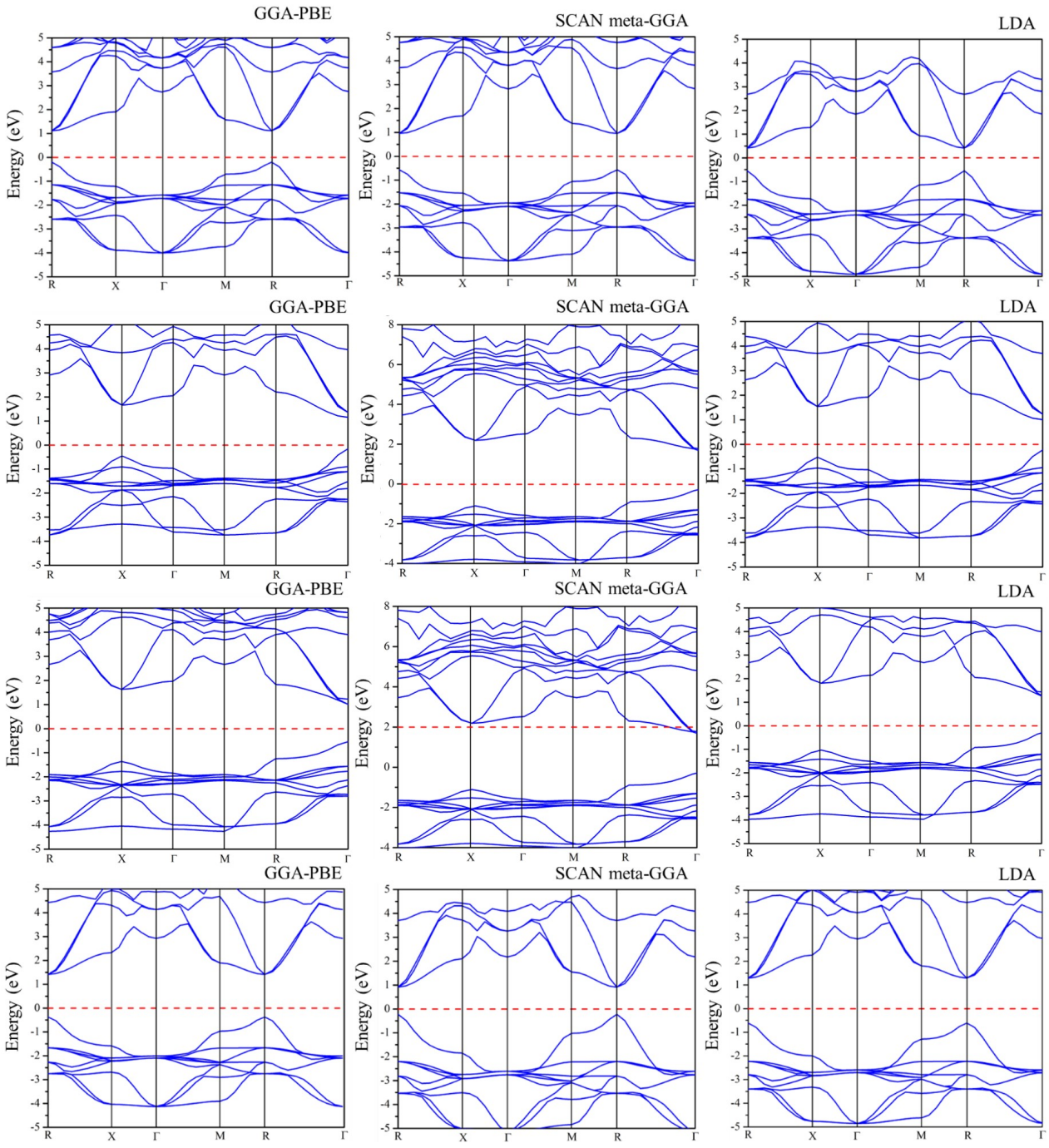


Figure 4.2: Band structures of (a) $CsPbI_3$, (b) $CsPbI_2Br$, (c) $CsPbIBr_2$ and (d) $CsPbBr_3$ perovskites obtained using three functionals.

4.4.2 Density of States

Figure 4.3 demostrates the TDOS and PDOS for $CsPbI_3$, $CsPbI_2Br$, $CsPbIBr_2$, and $CsPbBr_3$ perovskite compounds obtained using SCAN meta-GGA. Similarly, the vertical broken line in the DOS graphs represents the Fermi level. The DOS of these perovskite materials is

essential for understanding the contribution of each atom to bonding, opto-electronic properties, conductivity, and magnetic order. For $CsPbI_3$, PDOS in the VBM near the E_F (-3.5-0 eV) results from I-5p, while in the CBM (2.5-5 eV) the contribution is from hybridization of I-5p and Pb-6s orbitals, as seen in Figure 4.3 (a). For both $CsPbI_2Br$ and $CsPbIBr_2$ in Figure 4.3 (b) and (c), respectively, the contributions near the band edges result from the mixed halide orbitals (Br-4p and I-5p) and Pb-6p states. The same behaviour as $CsPbI_3$ is observed in Figure 4.3(d) for $CsPbBr_3$, but in this case, the VBM (-3.5-0 eV) is contributed by the Br 4p orbital. The Cs states (s and p) are distant from the Fermi level, although they play a key role in keeping charge balance and stabilizing the Pb-I and Pb-Br octahedra lattice for all perovskite compounds, as seen in Figure 4.3 (a) - (d). These findings are consistent with previously reported theoretical studies [16]. A similar observation on the density of states is seen for the perovskite compounds $CsPbI_3$, $CsPbI_2Br$, $CsPbIBr_2$, and $CsPbBr_3$ computed using GGA-PBE and LDA and are presented in Appendix, A.

4.5 Optical Properties

4.5.1 Dielectric Function

Figure 4.4 and 4.5 illustrate the calculated real ($\varepsilon_1(\omega)$) and imaginary ($\varepsilon_2(\omega)$) dielectric functions of these cubic perovskites $CsPbI_{3-x}Br_x$ (x = 1, 2, 3). The spectra were plotted from the data computed using the three functionals. The group velocity of the incident electromagnetic wave in the material is related to $\varepsilon_1(\omega)$ while $\varepsilon_2(\omega)$ is the energy absorption within the material associated with the dipole motion. There are several peaks that are observed in the $\varepsilon_1(\omega)$. These peaks are due to electron transition from I-5p, Br-4p and Pb-6s in the VB to the Pb-6p orbital in the CB. The other observed peaks are the electron transition from Pb-6s and Cs-6s in the VB to Cs-5d and Cs-4f in the CB as reported by Roknuzzaman *et al.* [86].

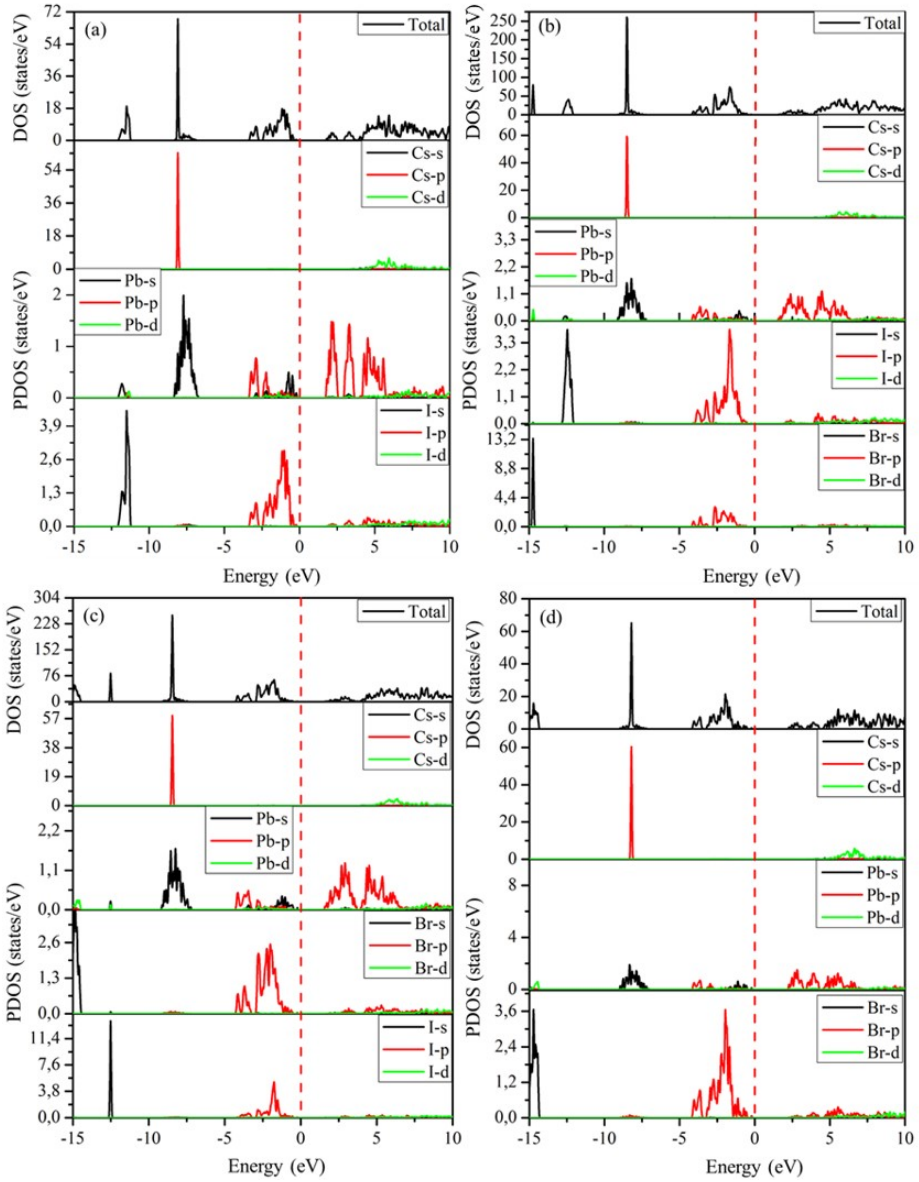


Figure 4.3: Total and partial density of states for (a) $CsPbI_3$, (b) $CsPbI_2Br$, (c) $CsPbIBr_2$ and (d) $CsPbBr_3$ perovskites obtained using SCAN meta-GGA.

The essential parameter in the $\varepsilon_1(\omega)$ spectra is the static dielectric function ($\varepsilon_1(0)$) which gives information on electronic polarizability of materials. The calculated $\varepsilon_1(0)$ and the maximum peak, $\varepsilon_1(max)$ values for $CsPbI_3$ using GGA-PBE, SCAN and LDA functionals were 5.2, 5.06, and 5.78, with energy values of 2.75, 2.50, and 2.72 eV, respectively, are shown in Figure 4.4 (a). The static dielectric of $CsPbI_3$ using SCAN is comparable with the previously calculated value which is 5.0 eV [159]. The $\varepsilon_1(max)$ is provides information about maximum energy storage capability of a material. For $CsPbI_2Br$, as shown in Figure 4.4 (b), the calculated $\varepsilon_1(0)$ and $\varepsilon_1(max)$ were recorded at 6.21, 4.44 and 7.53 with

energy values of 1.99, 2.49 and 1.09 eV using GGA-PBE, SCAN and LDA functionals, respectively. For $CsPbIBr_2$ (Figure 4.4 (c)), the $\varepsilon_1(0)$ and $\varepsilon_1(max)$ were recorded at 5.04, 4.41, and 7.53 with energy values of 2.47, 2.55 and 1.08 eV using the three functionals, respectively. Lastly, the calculated $\varepsilon_1(0)$ and $\varepsilon_1(max)$ of $CsPbBr_3$ are recorded at 5.2, 5.06 and 5.78 with energy values of 2.73, 2.94 and 2.44 eV using these exchange correlation functionals, GGA-PBE, SCAN and LDA, respectively, as illustrated in Figure 4.4 (d). The real part, $\varepsilon_1(\omega)$ falls below zero around 3-14 eV in all systems, implying that either the wave energy does not propagate within the materials, or the wave energy is attenuated but not visible on the surfaces.

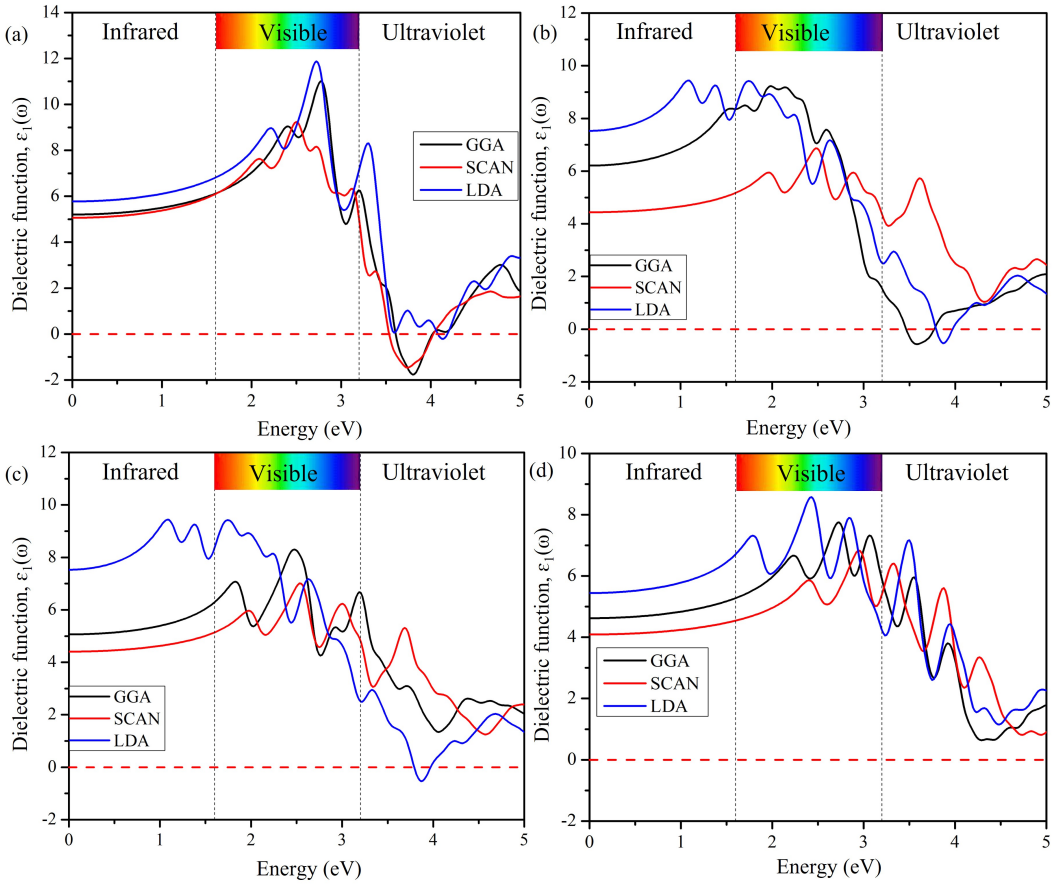


Figure 4.4: Calculated real part $\varepsilon_1(\omega)$ of (a) $CsPbI_3$, (b) $CsPbI_2Br$, (c) $CsPbIBr_2$ and (d) $CsPbBr_3$ compounds obtained using LDA, GGA-PBE and SCAN meta-GGA.

The values of the $(\varepsilon_2(\omega))$ for $CsPbI_3$, $CsPbI_2Br$, $CsPbIBr_2$, and $CsPbBr_3$ spectra are located at 2.32, 2.0, and 1.91 eV, at 1.45, 1.97, and 0.93 eV, 1.56, 1.96, and 0.99 eV and 2.15, 2.38 and 1.74 were determined using GGA-PBE, SCAN and LDA functionals, respectively as demonstrated in Figure 4.5 (a) - (d). These threshold values are closely

related to the fundamental energy band gap of the perovskite materials.

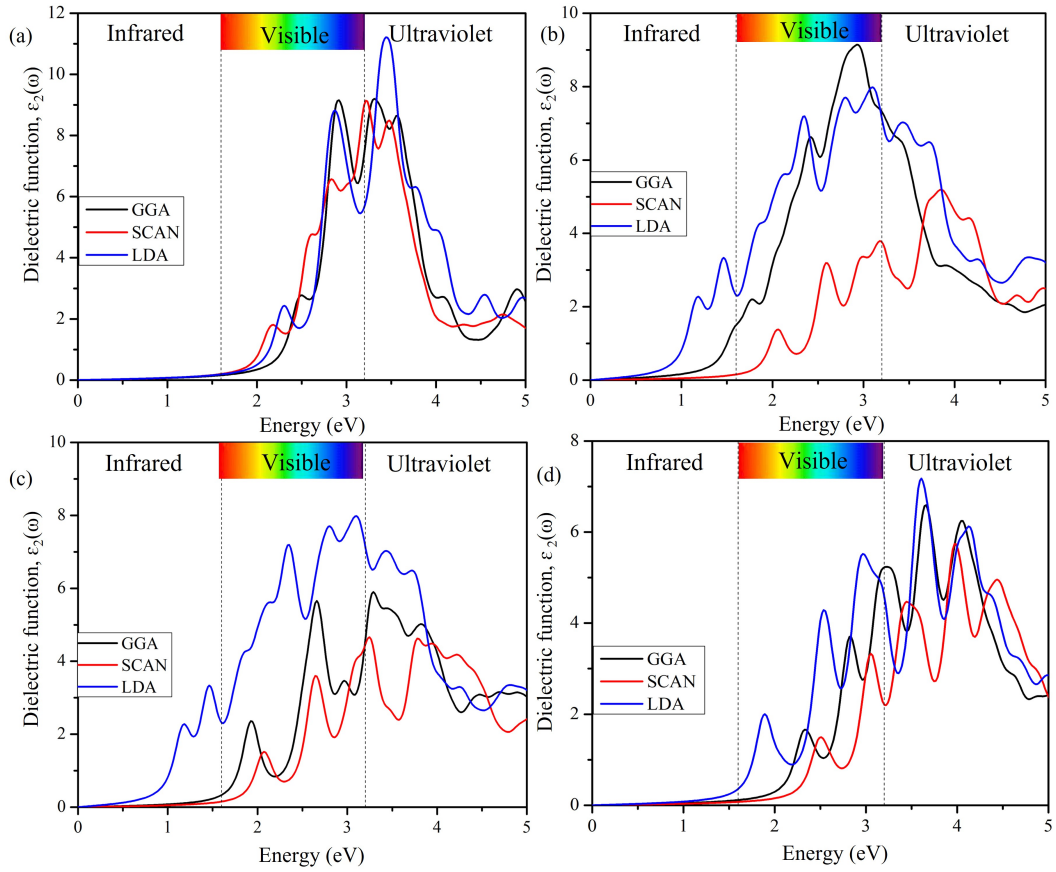


Figure 4.5: Calculated imaginary dielectric function $\varepsilon_2(\omega)$ of (a) $CsPbI_3$, (b) $CsPbI_2Br$, (c) $CsPbIBr_2$ and (d) $CsPbBr_3$ compounds obtained using LDA, GGA-PBE and SCAN meta-GGA.

4.5.2 Refractive Index

The refractive index, $n(\omega)$ is an essential feature of semiconductor compounds that determines how many photons propagate through the materials [19]. Figure 4.6 and Table 4.2 illustrate the dispersion $n(\omega)$ of $CsPbI_3$, $CsPbI_2Br$, $CsPbIBr_2$ and $CsPbBr_3$ perovskites and their calculated static refractive indices and the maximum values.

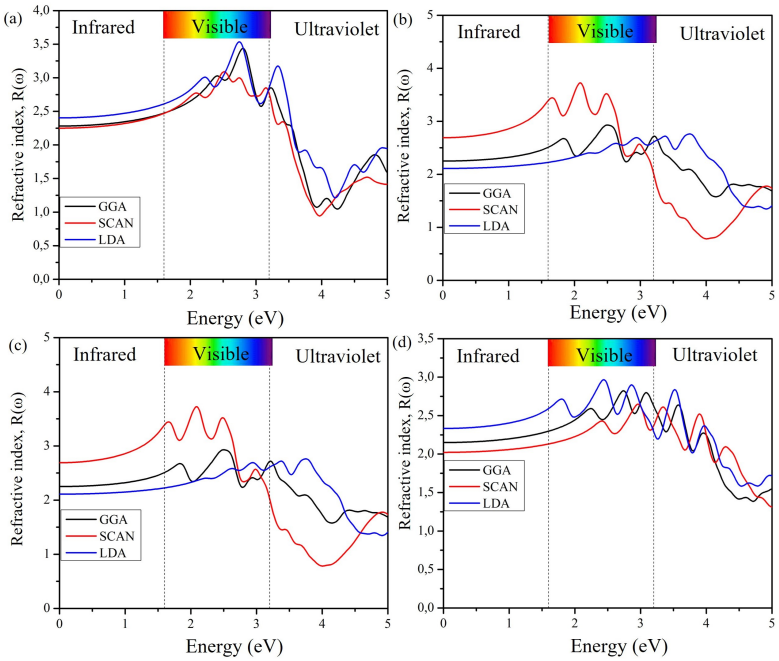


Figure 4.6: Calculated refractive index $n(\omega)$ of (a) $CsPbI_3$, (b) $CsPbI_2Br$, (c) $CsPbIBr_2$ and (d) $CsPbBr_3$ compounds obtained using LDA, GGA-PBE and SCAN meta-GGA.

Table 4.2: The calculated static refractive index n(0), and n(max) of $CsPbI_3$, $CsPbI_2Br$, $CsPbIBr_2$ and $CsPbBr_3$ compounds obtained using three functionals.

Compound	Functional	n (0)	n (max)
$CsPbI_3$	GGA	5.57	3.45
	SCAN	2.25	3.10
	LDA	2.40	3.54
$CsPbI_2Br$	GGA	2.50	3.1
	SCAN	2.20	2.70
	LDA	2.75	3.1
$CsPbIBr_2$	GGA	2.49	3.00
	SCAN	2.19	2.60
	LDA	2.74	3.10
$CsPbBr_3$	GGA	2.13	2.74
	SCAN	2.02	2.65
	LDA	2.33	2.97

4.5.3 Extinction Coefficient

The extinction coefficient $k(\omega)$ is used to measure the absorption of electromagnetic radiation. If there is absorption, $k(\omega)$ will be positive, and if $k(\omega) = 0$, it then implies that light is transmitted through the material. Figure 4.5 and 4.7, which depict the $(\varepsilon_2(\omega))$ and $k(\omega)$, respectively, exhibit the same kind of behaviour. The maximum values of the extinction coefficients for $CsPbI_3$ and $CsPbBr_3$ calculated using GGA, SCAN, and LDA were located around 3.5 - 4.5 eV. For $CsPbI_2Br$, and $CsPbIBr_2$ the maximum extinction is located at 7.5 eV for SCAN compared to GGA and LDA.

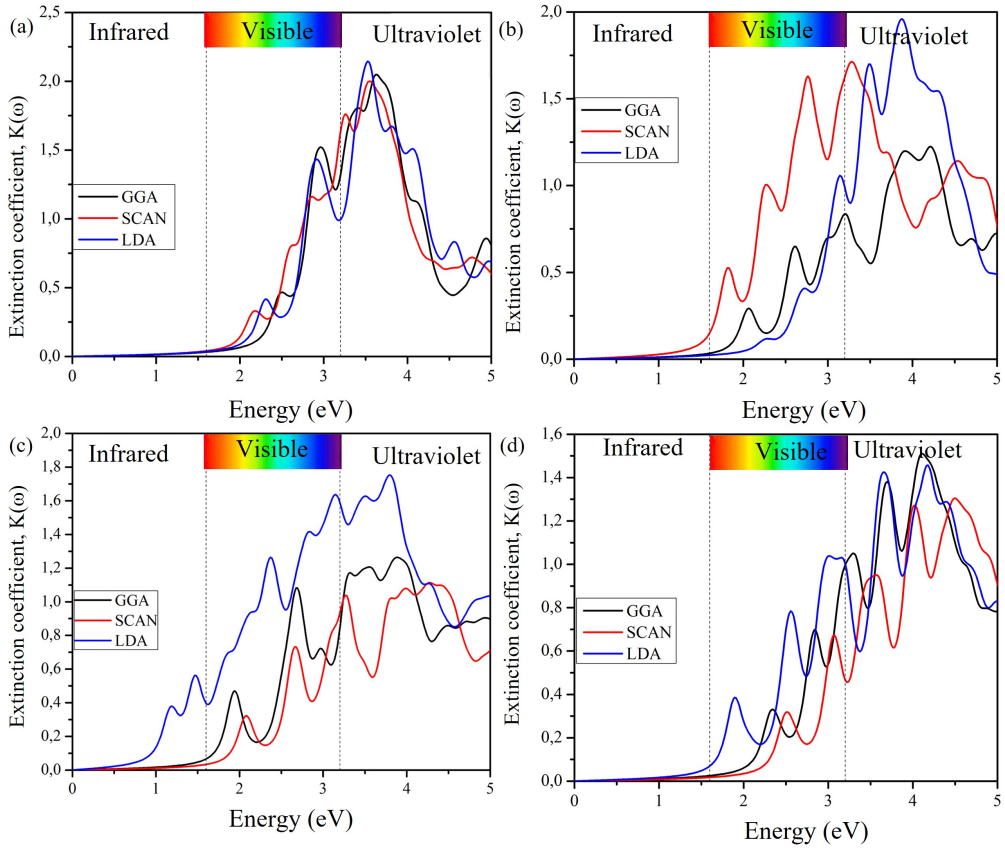


Figure 4.7: Calculated extinction coefficient $K(\omega)$ of (a) $CsPbI_3$, (b) $CsPbI_2Br$, (c) $CsPbIBr_2$ and (d) $CsPbBr_3$ compounds obtained using LDA, GGA-PBE and SCAN meta-GGA.

4.5.4 Reflectivity

Reflectivity energies of $CsPbI_3$, $CsPbI_2Br$, $CsPbIBr_2$, and $CsPbBr_3$ were all less than 16 eV as shown in Figure 4.8, indicating that these perovskites can serve as excellent coating ma-

terials. For the different functionals (GGA, SCAN and LDA), zero-frequency reflectivity, $R(0)$ values were found to be 0.152, 0.148 and 0.17 for $CsPbI_3$; 0.16, 0.127 and 0.217 for $CsPbI_2Br$; 0.14,0.131 and 0.223 for $CsPbIBr_2$; and 0.14,0.114 and 0.16 for $CsPbBr_3$, while the frequency dependent reflectivity $R(\omega)$ values were 3.78, 3.57 and 3.52 eV, 2.98, 3.86 and 14.46 eV, 14.32,15.59 and 14.4 eV, and 14.82, 15.62 and 14.74 eV for $CsPbI_3$, $CsPbI_2Br$, $CsPbIBr_2$, and $CsPbBr_3$, respectively. The reflectivity values of all the structures were located in the low-energy region, and furthermore, as reflectivity decreases, the photon energy increases.

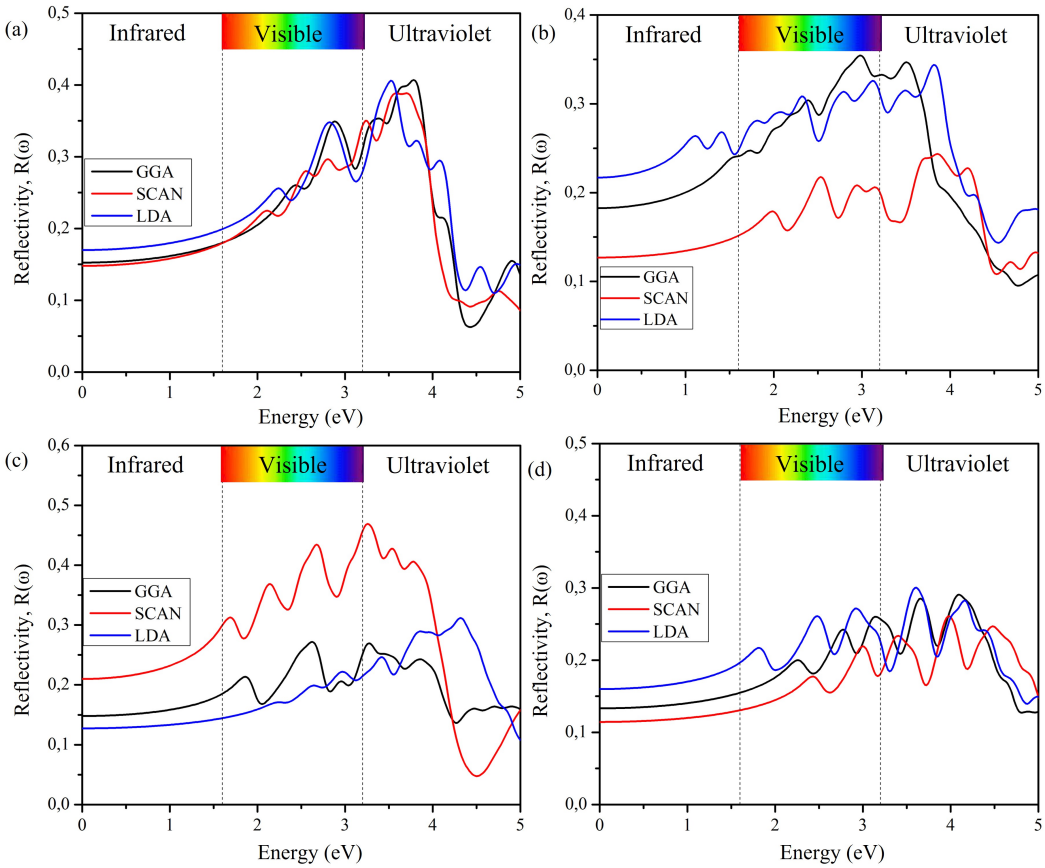


Figure 4.8: Calculated reflectivity $R(\omega)$ of (a) $CsPbI_3$, (b) $CsPbI_2Br$, (c) $CsPbIBr_2$ and (d) $CsPbBr_3$ compounds obtained using LDA, GGA-PBE and SCAN meta-GGA.

4.5.5 Absorption

The absorption coefficient provides crucial information about a material's capability to harvest light, influencing the efficiency of solar energy conversion. Figure 4.9 shows that these materials have several sharp optical absorption peaks located between 0.5 eV to 5 eV,

implying that these materials are capable of absorbing from in the ultraviolet, visible and infrared regions. The primary absorption peak is due to charge-transfer excitation from the VB to the CB. Peak transitions in these compounds start from electrons of the empty orbital valence band, Cs 6s and Pb 6p, to I 5p and Br 4p that dominate the deep conduction band. The substitution of the I^- ion with the Br^- ion increased absorption in the infrared and visible regions but lowers it in the ultraviolet region (4.2-5 eV). Figure 4.9 shows that higher absorptions obtained using SCAN functional, were recorded in the visible region for all the compounds when compared to absorption recorded using GGA and LDA functionals. The replacement of I with Br in $CsPbI_3$ showed maximum absorption in the infrared-visible regions than $CsPbI_3$, making these compounds suitable for applications in solar cells.

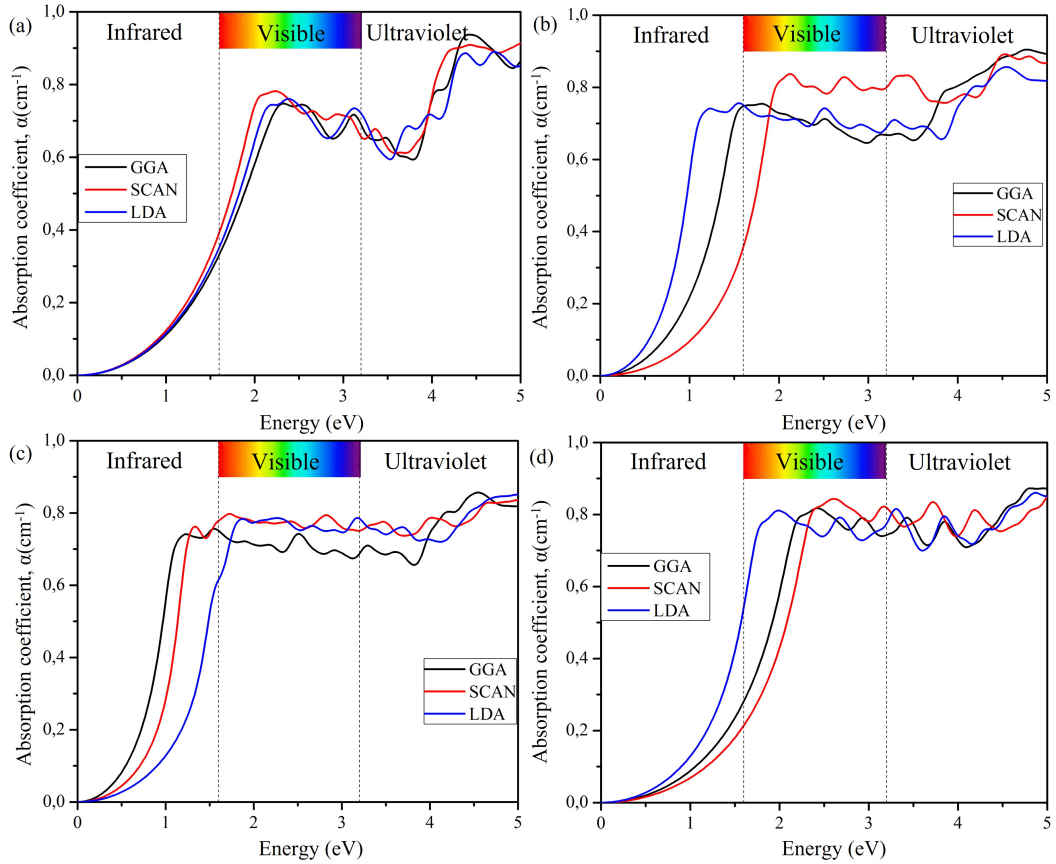


Figure 4.9: Calculated absorption coefficient $\alpha(\omega)$ of (a) $CsPbI_3$, (b) $CsPbI_2Br$, (c) $CsPbIBr_2$ and (d) $CsPbBr_3$ compounds obtained using LDA, GGA-PBE and SCAN meta-GGA.

4.5.6 Conductivity

The optical conductivity (which is defined as the conductivity of free charge carriers) is shown in Figure 4.10 for $CsPbI_3$. The optical conductivity values obtained using GGA, SCAN and LDA functionals starts from 2.29, 2.07 and 2.18 eV while for the other three systems the conductivity starts from 1.56,1.99 and 1.51 eV for $CsPbI_2Br$, 1.54, 2.01 and 1.03 eV for $CsPbIBr_2$, and 2.12, 2.40 and 1.71 eV for $CsPbBr_3$. The maximum values were located between 3.46 eV and 14.85 eV. Lastly, the magnitudes were found to be 2.80, 2.37 and 3.08 (1/fs), 2.58,2.57 and 2.68 (1/fs), 3.49, 2.19 and 3.20 (1/fs), and 3.29, 3.02 and 3.33 (1/fs) for $CsPbI_3, CsPbI_2Br, CsPbBr_2I$ and $CsPbBr_3$, respectively. The relationship between absorption and conductivity in a material is primarily governed by the interaction of photons with the material's electrons. When a material absorbs photons, the energy from the photons excites electrons from the valence band to the conduction band, creating electron-hole pairs. This process increases the number of charge carriers in the material, which in turn enhances its electrical conductivity. Therefore, greater absorption of photons generally leads to an increase in the material's photoconductivity. From the figure, it is clear that an increase in photon absorption leads to a higher rate of photo-conductivity. As a result, the higher absorption and photo-conductivity seen in the I-based perovskite compound could be attributed to a reduced band gap compared to the Br-based perovskite compounds. These materials show good optical properties including high absorption coefficient in the visible - infrared regions, low reflectivity, and photo-conductivity are suitable for solar cell applications.

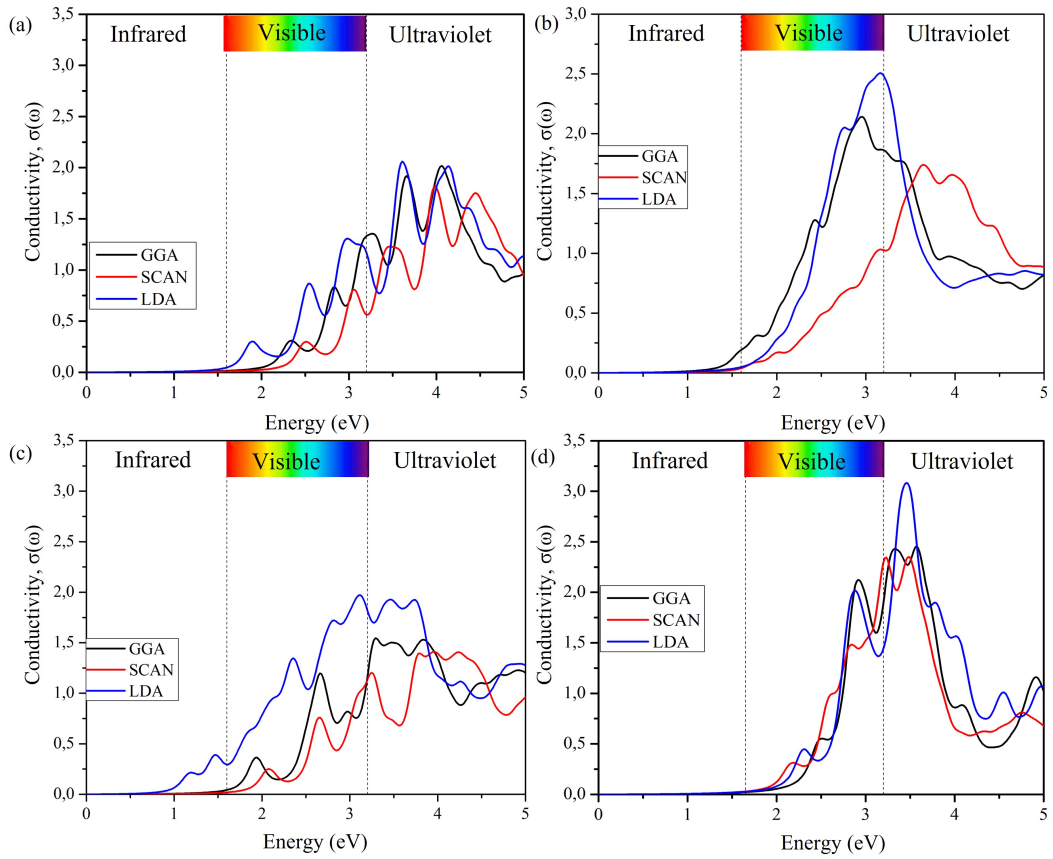


Figure 4.10: Calculated optical conductivity $\sigma(\omega)$ of (a) $CsPbI_3$, (b) $CsPbI_2Br$, (c) $CsPbIBr_2$ and (d) $CsPbBr_3$ compounds obtained using LDA, GGA-PBE and SCAN meta-GGA.

4.6 Elastic Properties

The elastic properties determine how a material deforms under extreme conditions such as external pressure and temperature. It is important to understand the mechanical behavior of these perovskite materials before being applied in the production of photovoltaic devices. To determine the mechanical stability of $CsPbI_{3-x}Br_x$ (x = 0, 1, 2, 3) perovskites, the elastic constants (C_{11}, C_{12}, and C_{44}) listed in Table 4.3 were calculated using GGA-PBE, SCAN and LDA functionals as implemented in VASP. The (C_{11}, C_{12}, and C_{44}) are shown in Table 4.3 satisfy the Born stability conditions indicating that these materials are mechanically stable. The difference between C_{12} and C_{44} ($C_{12} - C_{44}$) determines the Cauchy pressure are used to distinguish between the brittleness (fragility) and ductility (malleability) of the compounds [114]. If the Cauchy pressure is negative, the material is brittle; otherwise, it

is ductile. It is also useful for explaining the nature of atomic bonding in compounds.

Table 4.3: Calculated elastic constants and energy Cauchy pressure for $CsPbI_3$, $CsPbI_2Br$, $CsPbIBr_2$, and $CsPbBr_3$ compounds obtained using three functionals compared with experimental and other calculated theoretical values.

	$CsPbI_3$			$CsPbI_2Br$			$CsPbIBr_2$			$CsPbBr_3$		
Functional	GGA	SCAN	LDA	GGA	SCAN	LDA	GGA	SCAN	LDA	GGA	SCAN	LDA
C_{11} (GPa)	35.31	33.95	51.71	37.0	36.71	56.90	38.71	37.50	59.15	43.23	52.34	63.02
Cal.	34.41 [162]			35.74 [77]						42.32 [86]		
C_{12} (GPa)	4.98	5.22	5.03	5.91	5.02	6.19	5.66	5.41	5.49	6.66	7.08	7.04
Cal.	4.71 [162]			4.93 [77]						6.51 [86]		
C_{44} (GPa)	3.58	4.12	3.40	4.10	4.63	2.94	5.23	5.10	2.97	4.35	4.74	3.67
Cal.	3.85 [162]			4.09 [77]						4.24 [86]		
C_{12} - C_{44}	1.40	1.10	1.63	1.81	0.39	3.25	0.43	0.31	2.52	2.31	2.34	3.37

The material is isotropic when the shear anisotropy factor, A, equals one; otherwise, it is anisotropic when A is less than one or greater than one [115]. The calculated anisotropic values for $CsPbI_3$ were found to be A = 0.233, 0.277 and 0.153 obtained using GGA-PBE, SCAN and LDA functionals, respectively. The calculated values are comparable to the available theoretical value of 0.259 [95]. For $CsPbI_2Br$, A = 0.264, 0.292 and 0.116, which were obtained using GGA-PBE, SCAN and LDA functionals, respectively. For $CsPbBr_2I$ A = 0.316 and 0.111 obtained using GGA-PBE and LDA functionals, respectively. Lastly, the values for $CsPbBr_3$ were calculated to be A = 0.238, 0.209 and 0.131 using GGA-PBE, SCAN and LDA functions, respectively. All the functionals predicted the anisotropy factor to be less than one, implying that these materials are anisotropic. The bulk, 'B' and shear, 'G' moduli determine the strength or hardness of a compound. The calculated perovskite bulk modulus value varies from 14.13 GPa (for $CsPbI_3$ using SCAN functional) and 25.70 GPa (for $CsPbBr_3$ using LDA functional), implying that these compounds are flexible. The B/G ratio and Poisson's ratio are also important parameters to measure the compressibility and distinguish the brittle/ductile nature of the material [7]. For Poisson's ratio (ductile, and brittle) and Pugh's ratio (B/G > 1.75 ductile and B/G < 1.75 brittle). Based on these, we demonstrated that $CsPbI_3$, $CsPbI_2Br$, $CsPbBr_2I$ and $CsPbBr_3$ are ductile, as illustrated in Table 4.4. The calculated elastic constants of $CsPbI_3$, $CsPbI_2Br$, $CsPbBr_2I$ and $CsPbBr_3$ agree with previously reported theoretical results, particularly those obtained with the GGA

functionals, as listed in Table 4.4 [108, 116, 117]. The C_{11} obtained with the LDA functionals is much higher than those reported in the literature and those obtained using GGA in this study. Table 4.4 show that when I^- ion is replaced by Br^- ion, the bulk modulus increases, indicating that these perovskites become less rigid and more compressible.

Table 4.4: Calculated elastic constants and energy Cauchy pressure for $CsPbI_3$, $CsPbI_2Br$, $CsPbIBr_2$, and $CsPbBr_3$ compounds obtained using the three functionals.

	$CsPbI_3$			$CsPbI_2Br$			$CsPbIBr_2$			$CsPbBr_3$		
Functionals	GGA	SCAN	LDA	GGA	SCAN	LDA	GGA	SCAN	LDA	GGA	SCAN	LDA
Bulk (GPa)	15.09	14.13	20.59	16.38	15.64	22.09	17.74		23.62	18.85	22.17	25.70
Cal.	14.61 [162]									17.54 [86]		
Shear (GPa)	6.69	7.10	8.27	7.16	7.71	8.70	7.60		8.94	8.09	9.42	9.51
Cal.	6.86 [162]											
Young (GPa)	17.38	18.17	21.55	18.64	19.77	22.73	19.83		23.41	21.11	24.72	24.99
Poisson	0.3069	0.2848	0.3229	0.309	0.288	0.326	0.313		0.3320	0.3123	0.3139	0.3353
Pugh's (GPa)	2.2566	1.9897	2.4904	2.288	2.029	2.539	2.334		2.643	2.3303	2.3537	2.7018

4.7 Thermodynamic Properties

Thermodynamic properties give valuable insights into a material's behavior in response to pressure and temperature changes, to predict the materials performance in photovoltaic cell. Thermodynamic parameters including thermal expansion, heat capacity, vibrational entropy, sound velocities, hardness, and melting temperature. These parameter provides a detailed information on material features such as thermodynamic stability and inter-atomic interaction for photovoltaic application.

Table 4.5: Calculated average sound velocities (v_s) and Debye temperature (θ_D), obtained using the three functionals.

Compound	Functional	v_s	θ_D
$CsPbI_3$	GGA	1346	107.4
	SCAN	1434	116
	LDA	1413	117.3
$CsPbI_2Br$	GGA	1398	113.9
	SCAN	1412	116.9
	LDA	1456	123.3
$CsPbIBr_2$	GGA	1448	120.4
	SCAN	-	-
	LDA	1456	123.3
$CsPbBr_3$	GGA	1502	127.7
	SCAN	1584	136.8
	LDA	1542	136.3

The Debye temperature (θ_D) is a key fundamental physical quantity for solids, related to thermodynamic parameters including melting temperature, thermal expansion and heat capacity. These thermodynamic parameters affect the perfomance of opto-electronic devices. The Debye temperature calculated using equation (3.88) is correlated with B and G moduli, as well as the density of the material. Table 4.5 lists the calculated average sound velocity and Debye temperature obtained using both GGA-PBE, SCAN and LDA. The results show that the $CsPbI_3$, $CsPbI_2Br$, $CsPbBr_2I$ and $CsPbBr_3$ perovskites have a low θ_D, indicating that the melting point, acoustic velocity and the inter-atomic binding forces are low for these compounds. It was also observed that the substitution of the I^- ion with Br^- ion increases the values of the Debye temperature.

The temperature dependence of C_v plots of $CsPbI_3$, $CsPbI_2Br$, $CsPbBr_2I$ and $CsPbBr_3$, are shown in Figure 4.11 (a) - (d) with the temperature ranging from 0 to 600 K. The C_v parameter rises with increasing temperature due to phonon thermal softening occurs which eventually becomes stable. The maximum heat capacity for $CsPbI_3$, $CsPbI_2Br$, $CsPbBr_2I$

and $CsPbBr_3$ are 120.26, 121.23, 120.83, and 120.34 $J/mol^{-1}K^{-1}$, respectively. It was notable that the C_v, at higher temperatures reaches the Dulong-Petit limit.

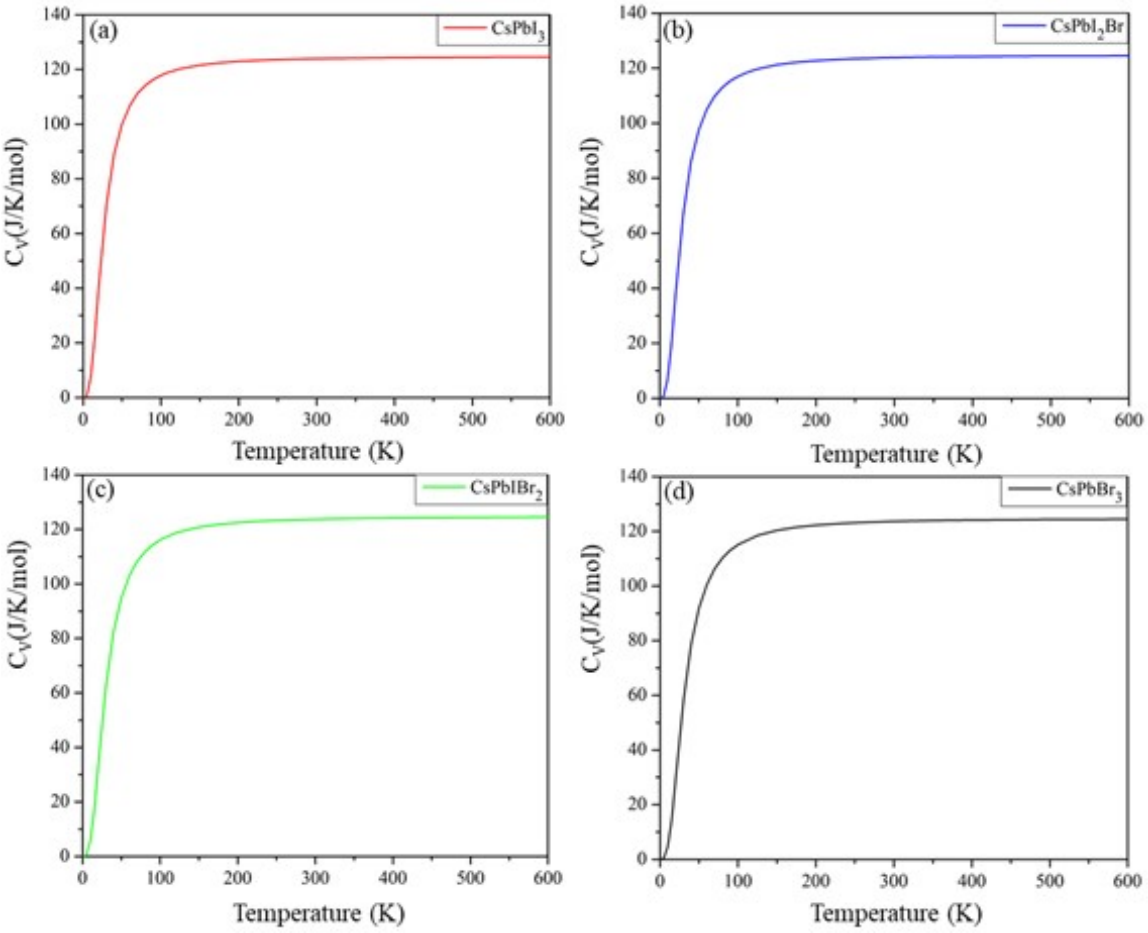


Figure 4.11: Temperature dependence of heat capacity of (a) $CsPbI_3$, (b) $CsPbI_2Br$, (c) $CsPbBr_2I$ and (d) $CsPbBr_3$ perovskites obtained using GGA-PBE and LDA the functionals.

Temperature-dependent thermodynamic properties (i.e., enthalpy, Gibbs-free energy, and entropy) are shown in Figure 4.12 (a) - (d). From the figures, the enthalpy rise with increasing temperature, while the free energy and entropy decreased as the temperature increased. Entropy is a physical characteristic that measures the randomness or disorder in a system. It further demonstrates that when the temperature approaches zero, the three thermodynamic parameters decreased, which is consistent with the third law of thermodynamics.

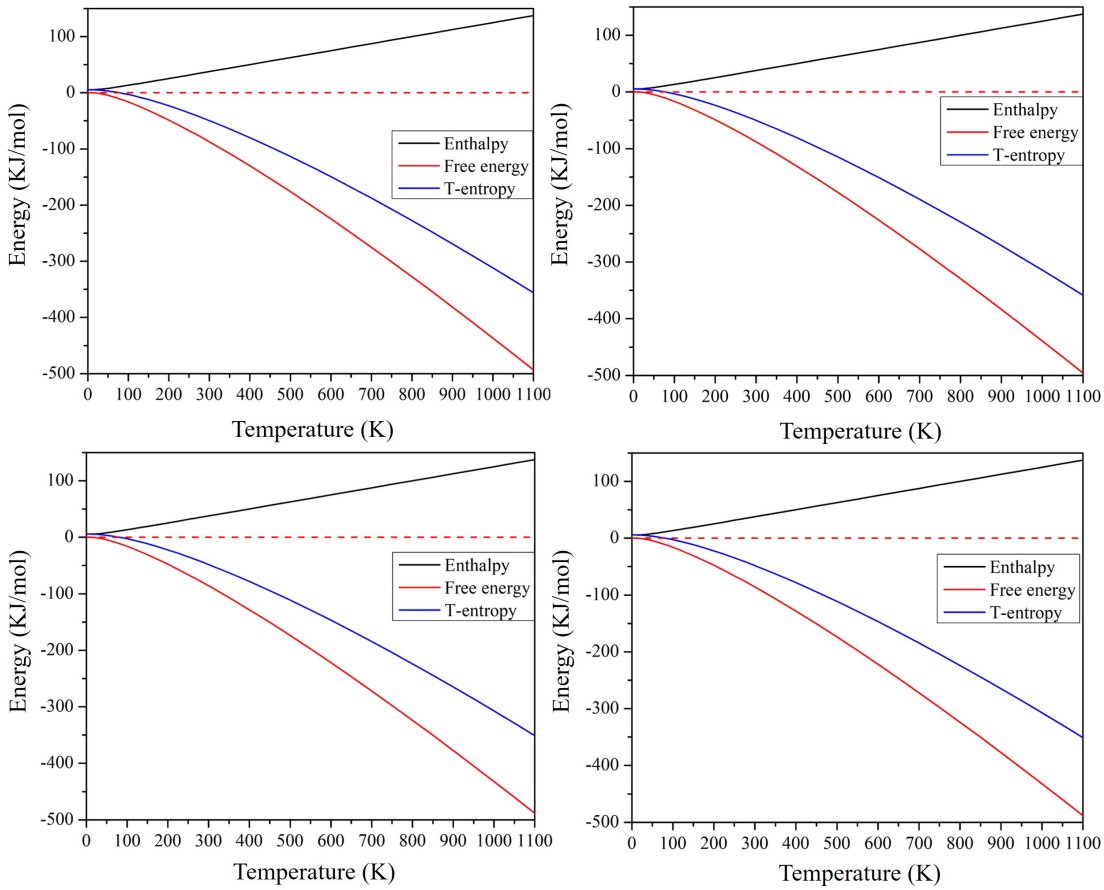


Figure 4.12: Temperature dependence of thermodynamic properties, that is, enthalpy, temperature entropy, and free energy of (a) $CsPbI_3$, (b) $CsPbI_2Br$, (c) $CsPbBr_2I$ and (d) $CsPbBr_3$ perovskites obtained using GGA-PBE.

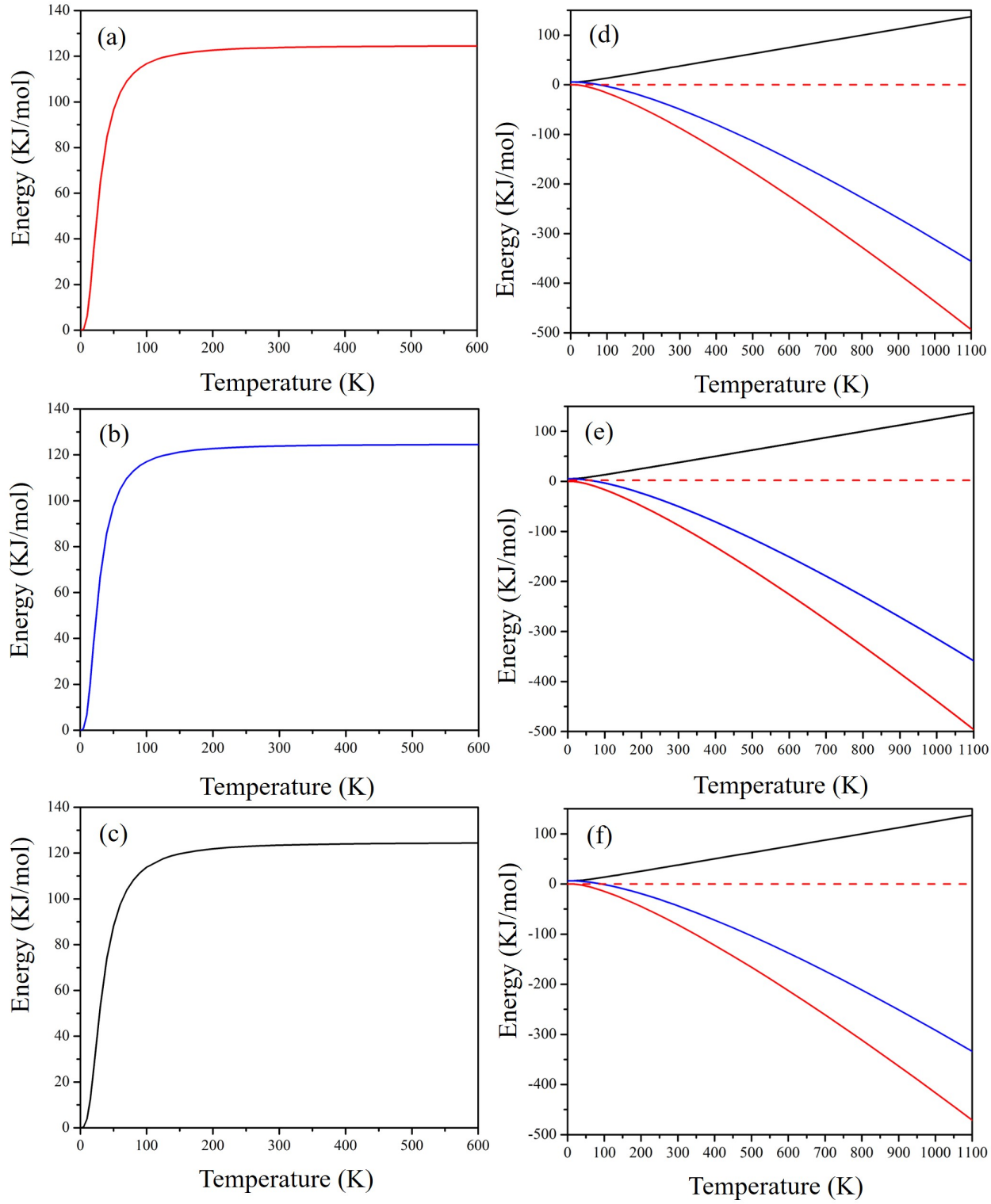


Figure 4.13: Temperature dependence of heat capacity of (a) $CsPbI_3$, (b) $CsPbI_2Br$ and (c) $CsPbBr_3$ perovskites and their (d) - (e) enthalpy, temperature entropy, and free energy using SCAN functional.

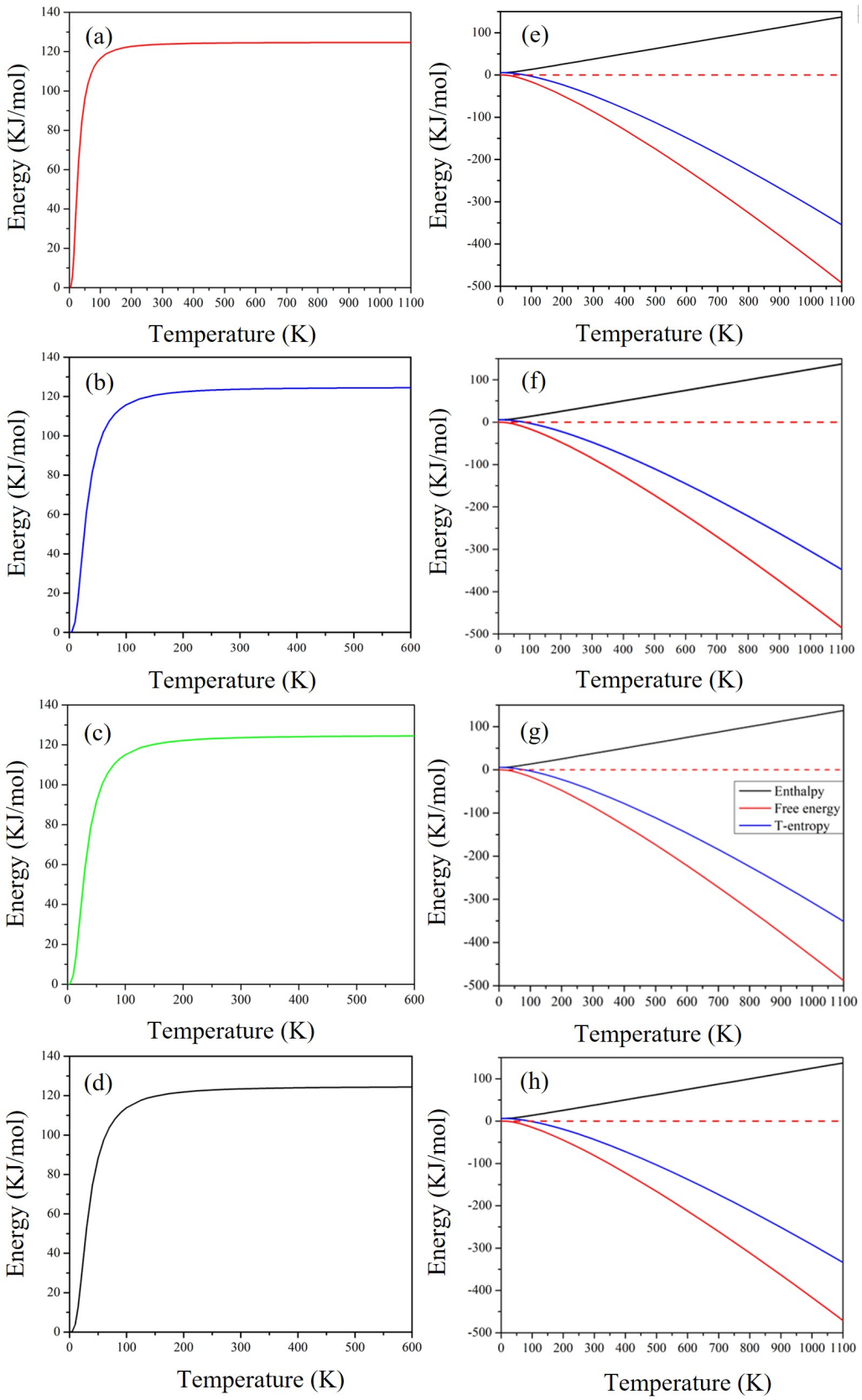


Figure 4.14: Temperature dependence of heat capacity of (a) $CsPbI_3$, (b) $CsPbI_2Br$, (c) $CsPbIBr_2$ and (d) $CsPbBr_3$ perovskites and their (e) - (h) enthalpy, temperature entropy, and free energy using LDA functional.

4.8 Summary

The structural, electronic, optical, mechanical and thermodynamic properties of the $CsPbI_3$, $CsPbI_2Br$, $CsPbBr_2I$ and $CsPbBr_3$ perovskite materials were investigated using GGA-PBE, SCAN, and LDA exchange-correlation functionals using DFT. SCAN meta-GGA incorporate more complex exchange correlation functionals that depend not only on the electron density, but also on its Laplacian and gradients. SCAN approximation reproduced structural parameters and energy band gap better than GGA-PBE and LDA. The band structures of $CsPbI_3$, $CsPbI_2Br$, $CsPbBr_2I$ and $CsPbBr_3$ indicated that they all exhibit a direct band gap. All $CsPbI_{3-x}Br_x$ (x = 0, 1, 2, 3) perovskites were found to be ductile and mechanically stable according to elastic constants, the Pugh ratio and the Poisson ratio. The thermodynamic properties illustrated that as the temperature approaches zero, the three thermodynamic parameters, namely enthalpy, free energy, and entropy, were consistent with the third law of thermodynamics. The optical absorption and reflectivity spectra of these perovskite materials are promising candidates for the application in solar cells.

5

Doping $CsPbI_3$ with Transition Metals (Mn, Fe, Ni and Zn)

5.1 Introduction

Transition metal doping is a method that can be used to introduce TM ions into the $CsPbI_3$ perovskite material to modify the material's properties such as electronic and optical, which can improve the performance of opto-electronic devices including photo-detectors, LEDs and solar cells. Different transition metal ions that have been used in doping $CsPbI_3$ are Cr, Cu, Fe, Sr, Ni, Mn, Co and Ag [98, 163]. Each transition metal ion has different intrinsic properties which may influence the properties of the perovskite compounds. The choice of the transition metal ion is informed by a specific application. One of the key

advantages of the TM ion doping is that it can introduce new energy levels into a material, which can broaden the absorption spectrum of the material. This can lead to an increase in the absorption of light and overall improvement of the solar cell performance. Additionally, transition metal doping can also introduce new recombination pathways, and this may decrease charge carrier recombination and increase the efficiency of these photovoltaic devices. The choice of the transition metal ion is informed by the similar charge state of $5s^2$ lone pair in Pb^{2+} and the $4s^2$ lone pair in the selected transition metals. These transition metals can maintain a stable ns^2 electronic configuration, making them feasible to replace Pb^{2+} due to its toxicity concerns. Essentially, transition metals exhibiting similar ionic radii to that of Pb^{2+} and exhibiting +2 oxidation state. The ionic radii differences are below 30 % typical margin observed in literature. In this chapter, first-principles density functional theory was employed to study the structural, electronic, optical, elastic and thermodynamics properties of transition metal (Mn, Fe, Ni, and Zn) doped $CsPbI_3$ perovskites using GGA+U functional.

5.2 Computational Method

To investigate the effect of dopants structural, electronic, machanical, optical and thermodynamic properties of transition metal doped in $CsPbI_3$, one Pb^{2+} was replaced with one metal impurity in 2 x 2 x 2 supercell models containing 40 atoms, making it possible to achieve a desired doping percentage of 12.5 %, as shown in Figure 5.1. The calculations were performed using the VASP [114, 164]. GGA was employed as an exchange-correlation functional parameterization proposed by Perdew, Burke, and Ernzerhof for the calculations [117]. All the calculations have considered the spin polarization. GGA+U method was used to calculate the properties in all analyzed doped systems in order to correct the strong Coulomb interactions of 3d electrons. All the dopants, Mn, Fe, Ni, and Zn, had Hubbard, U_{eff} values set at 3.5, 4.3, 6.4, and 6.0 eV, respectively [105, 165–167]. The threshold of the total convergence energy employed was 10^{-8} eV $atom^{-1}$. The cut-off kinetic energy used was 500 eV. The BZ integrations used were $6 \times 6 \times 6$ for Monkhorst-Pack

k-point mesh [136]. Moreover, the spin-polarized mode was considered in all calculations. The electronic configuration for transition metal Mn, Fe, Ni, and Zn are

Mn: [Ar] $3d^5\ 4s^2$

Fe: [Ar] $3d^6\ 4s^2$

Ni: [Ar] $3d^8\ 4s^2$

Zn: [Ar] $3d^1\ 4s^2$

5.3 Structural Properties

The study of TM doped materials $CsPb_{0.875}TM_{0.125}I_3$, (where TM = Mn, Fe, Ni, and Zn) has a space group Pm-3m with a cubic structure. The undoped material has a unit cell that consists of five atoms, as shown in Figure 5.1, with the Cs atom occupying the crystal's body centered position at 1b Wyckoff site (0.5, 0.5, 0.5). The B-site cations are situated at 1a Wyckoff site (0, 0, 0) and occupy the corner positions of the cubes, whereas I atoms occupy the face centred positions at the 3d Wyckoff site (0.5, 0, 0). Figure 5.1 shows the constructed supercell of $CsPbI_3$ perovskites consisting of 40 atoms i.e. 24 I atoms, 8 Pb atoms, and 8 Cs atoms. An impurity was added in the undoped 2 x 2 x 2 supercell of $CsPbI_3$ by replacing the Pb^{2+} atom with TM dopant (Mn^{2+}, Fe^{2+}, Ni^{2+}, and Zn^{2+}) ions resulting in a doping concentration of approximately 12.5 %.

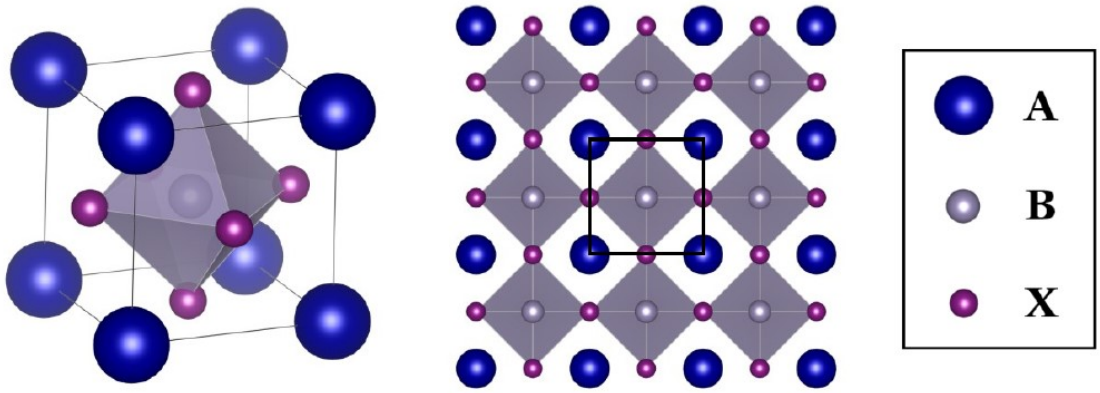


Figure 5.1: The constructed polyhedron unit cell (left) and supercell cubic perovskite crystal structure with A-cation (blue), B-cation (grey) and X-anions (magenta).

The computed structural parameters of undoped and TM doped $CsPbI_3$ perovskite com-

pared with reported experimental and theoretical values are summarized in Table 5.1. The substitution of Pb atom with the transition metal (Mn, Fe, Ni, and Zn) atom decreases the unit cell volume and lattice constants as demonstrated in Table 5.1. This is because of the ionic radii differences between the host and dopant. These transition metals have a smaller ionic radius compared to the Pb atom. Lead (Pb) has an ionic radius of 2.20 Å and was substituted by the smaller value of the ionic radii of manganese (0.83 Å), iron (0.78 Å), nickel (0.69 Å), and zinc (0.74 Å). This behavior of lattice parameters can also be explained in terms the electronic configuration of 3d TM (Mn, Fe, Ni, and Zn) that replaces the Pb atom in $CsPbI_3$. The introduction of 3d electrons in VB and CB near Fermi level resulted in the alteration of the crystal configuration. To demonstrate the transition metal doping effect on $CsPbI_3$ lattice constants, the calculated bond lengths and angles are presented in Table 5.1. The substitution of Pb with the TM = (Mn, Fe, Ni, and Zn) resulted into an increase in Pb-I bond-length average of 3.312 Å. The calculated bond lengths between TM and I were found to be varying from 2.898 Å – 3.009 Å as presented in Table 5.1. Transition metal doping does not change the bond angles, they remain unchanged before and after doping. The calculated structural parameters correspond with what has been reported previously, particularly Mn doped $CsPbI_3$ perovskite. The study analyzed the resulting changes of the mentioned properties when Pb^{2+} is replaced with selected transition metals.

Table 5.1: The computed structural parameters, angle, and bond length for transition metal doped $CsPbI_3$ perovskites are compared with experimental and theoretical values.

Compound	Lattice contant (Å)			Volume (Å^3)	Angle (°)	Bond length (Å)	Band gap (eV)
	This work	Cal.	Exp.				
$CsPbI_3$	a = 6.398	a = 6.38 [168]	6.29 [169]	V = 261.83	$\alpha = \beta = \gamma = 90.00$	Pb - I = 3.199 Pb - I = 3.2 [170]	1.488 1.44 [171]
$CsPb_{0.875}Mn_{0.125}I_3$	a= 6.341	a = 6.33 [99]	-	254.99	$\alpha = \beta = \gamma = 90.00$	Pb - I = 3.332 Mn - I = 3.009 Mn - I = 3.0 [170]	1.274 1.24 [99]
$CsPb_{0.875}Fe_{0.125}I_3$	a = 6.323		-	V = 252.81	$\alpha = \beta = \gamma = 90.00$	Pb - I = 3.368 Fe - I =2.955	1.270
$CsPb_{0.875}Ni_{0.125}I_3$	a = 6.308		-	V = 250.92	$\alpha = \beta = \gamma = 90.00$	Pb - I = 3.409 Pb - I = 3.19 [171] Ni - I = 2.898 Ni - I = 2.89 [171]	0.491
$CsPb_{0.875}Zn_{0.125}I_3$	a = 6.321		-	V = 251.94	$\alpha = \beta = \gamma = 90.00$	Pb - I = 3.359 Zn - I = 2.962	0.717

5.4 Electronic Properties

5.4.1 Band Structure

The electronic properties are important for studying the materials behavior when applied in opto-electronic and photovoltaic devices. It is necessary to investigate the energy band gap to determine whether a compound is a metal, semiconductor or an insulator, and also study the total and partial DOS. [51, 172]. The standard DFT is not accurate computing the energy band gap of d-electrons transition metals. Therefore, GGA+U offers high quality and simple way to compute strongly correlated interactions in systems that contain d-electron transition metals. Figure 5.2 illustrates the measured band structure of $CsPbTMI_3$ (where TM = Mn, Fe, Ni, and Zn) along the high symmetry including the points Γ, X, M, R, and Γ in the direction of the first Brillouin region. Figure 5.2 shows the band structure of the undoped $CsPbI_3$, indicating that the compound has a direct band gap of 1.488 eV and is also consistent with the previous theoretical reported value by Liu *et al* [171].

The incorporation of the dopants into the host of the semiconductor reduces the band gap because of the formation of dopant levels at the CB or VB edge as depicted in Figure

5.2. It is also evident that the VBM and CBM are displayed at distinct k-points, which indicates the indirect band gap. As a result, TM-doped compared to undoped $CsPbI_3$ may show increased absorbance in the visible range and easier electron transport from the VB to the CB. These $CsPb_{0.875}TM_{0.125}I_3$ perovskites have an indirect band gap albeit with intermediate states observed. The creation of the intermidiate states make it easier for the electron transfer from the VB to the CB. The band gap was reduced from 1.488 eV ($CsPbI_3$) to 1.274 eV ($CsPb_{0.875}Mn_{0.125}I_3$), 1.270 eV ($CsPb_{0.875}Fe_{0.125}I_3$), 0.491 eV ($CsPb_{0.875}Ni_{0.125}I_3$), and 0.717 eV ($CsPb_{0.875}Zn_{0.125}I_3$). For $CsPb_{0.875}Fe_{0.125}I_3$, there is flat-gap state at the Fermi energy caused by Fe t_{2g} orditals as seen in 5.2 [173]. These TM doped $CsPbI_3$ compounds exhibit high absorbance in the visible region compared to undoped $CsPbI_3$ because of the intermediate state appearance. Hence, TM doping is necessary to improve the opto-electronic properties of the perovskite materials for solar cell applications.

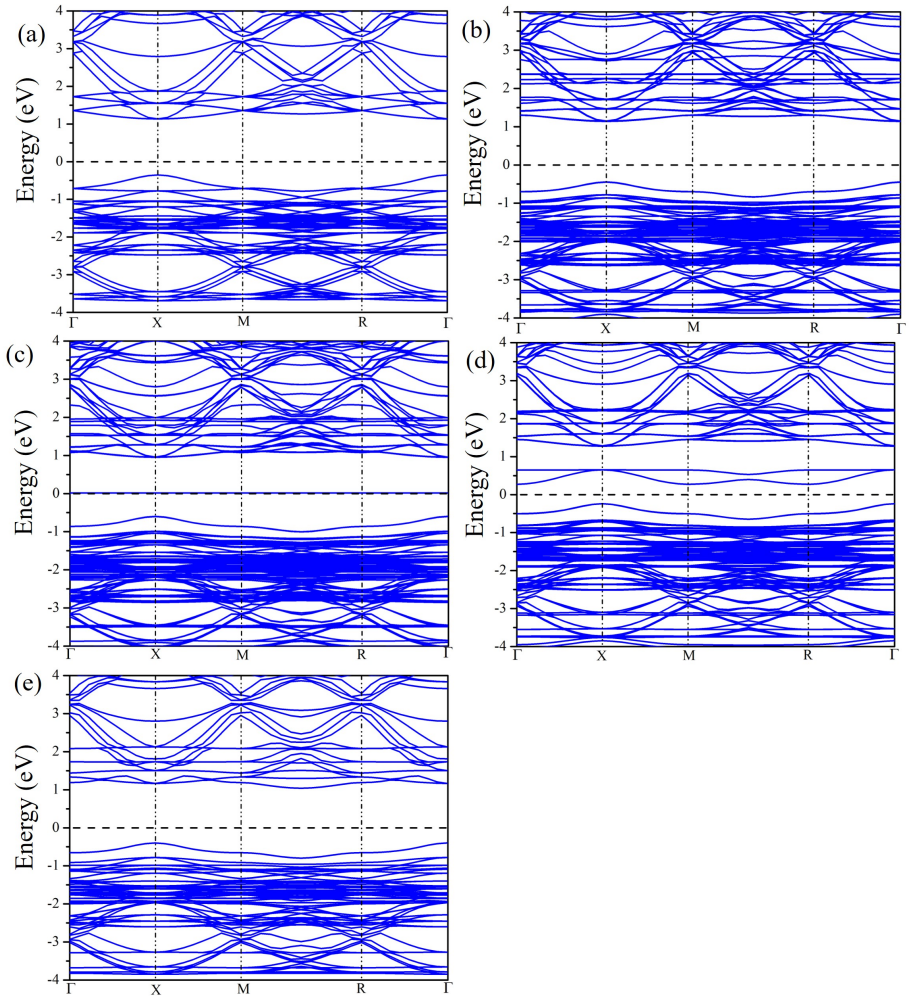


Figure 5.2: Electronic band structure of the (a) Mn-doped $CsPbI_3$, (b) Fe-doped $CsPbI_3$, (c) Ni-doped $CsPbI_3$, and (d) Zn-doped $CsPbI_3$ perovskites.

5.4.2 Density of States

The computed total and partial DOS of undoped and TM-doped $CsPbI_3$ are illustrated in Figure 5.3-5.4 with an energy band gap at the E_F separating the VB and CB at 0 eV. As seen from Figure 5.3, the VBM of undoped $CsPbI_3$ is mainly contributed by the Pb-s, Pb-p, and I-p orbitals (from -4 eV to 0 eV) below the E_F. There is also spectral peaks around -8 eV which is from Cs-p and Pb-s states. The CBM is mainly contributed by the Pb-p orbital near the band edges and minor peaks from Cs-d orbital.

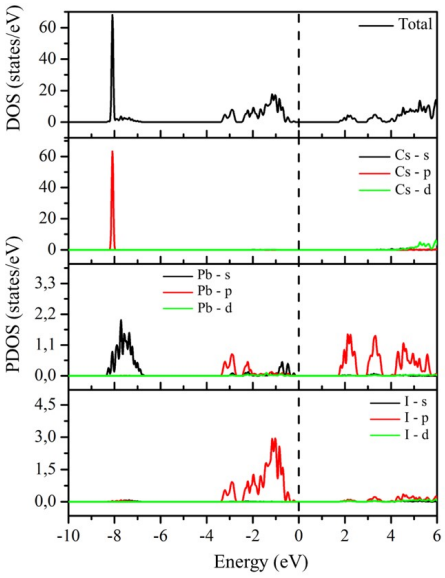


Figure 5.3: Total and partial DOS for undoped $CsPbI_3$ perovskite.

The spin-polarized DOS of the perovskites compounds doped with 12.5 % of Mn, Fe, Ni and Zn were calculated as shown in Figure 5.3. The VBM of the doped $CsPbI_3$ shows that the minority and majority spin states of the total DOS plot have an asymmetrical feature for Mn, Fe, and Ni dopants, indicating that doped perovskite compounds have magnetic properties. Zn-doped material exhibit symmetrical features showing that the material is non-magnetic. As a result, the substitution of TM for Pb in $CsPbI_3$ results in the appearance of an electronic state at the top of the valence band in the majority spin channel. PDOS plots show that the CB edges of magnetic dopants indicate rising contribution of Mn (3d), Fe (3d), and Ni (3d) states especially in the spin down channel. Furthermore, Figure 5.4 indicates that the impurity states generated are primarily a result of the hybridization of Mn (3d), Fe (3d), Zn (3d), and Ni (3d), Pb (4p), and I (5p) orbitals. Figure 5.4 (b) shows the spin-up bands located at -4 to -2 eV in the VB above the Fermi level and the spin-down bands located in the E_F and CB because of half-filled Fe ions (e_g, t_{2g}). The interaction between the dopant's transition metal and the adjacent I atom leads to the splitting of energy levels near the Fermi energy. These findings suggest that the magnetic characteristics observed in the TM-doped $CsPbI_3$ may be attributed to the p–d hybridization.

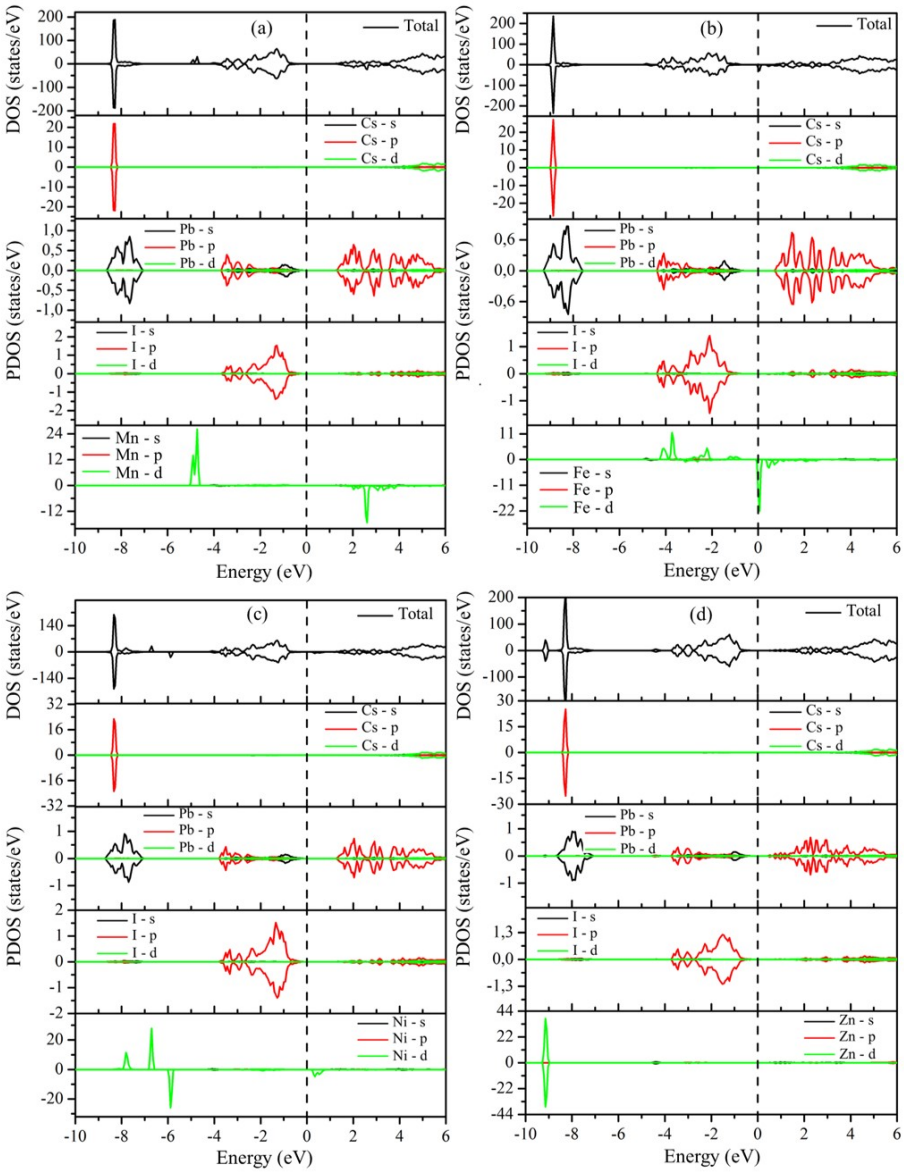


Figure 5.4: Total and partial density of states for (a) $CsPb_{0.875}Mn_{0.125}I_3$, (b) $CsPb_{0.875}Fe_{0.125}I_3$, (c) $CsPb_{0.875}Ni_{0.125}I_3$, and (d) $CsPb_{0.875}Zn_{0.125}I_3$ perovskite materials.

5.5 Optical Properties

5.5.1 Dielectric Function

A material's optical response is defined by a set of frequency (or energy) based factors that are highly dependent on the electronic band structure's features. Essentially, the optical properties of the compounds are determined by the interaction between particles of incident light and charge carriers at the surface. The calculated $\varepsilon_1(\omega)$ and $\varepsilon_2(\omega)$ of dielectric

function of $CsPbI_3$ and $CsPb_{0.875}TM_{0.125}I_3$ are displayed in Figure 5.5 - 5.6. Both the $\varepsilon_1(\omega)$ and $\varepsilon_2(\omega)$ have the most intense peaks in the low energy area (visible region) for both undoped and TM doped $CsPbI_3$.

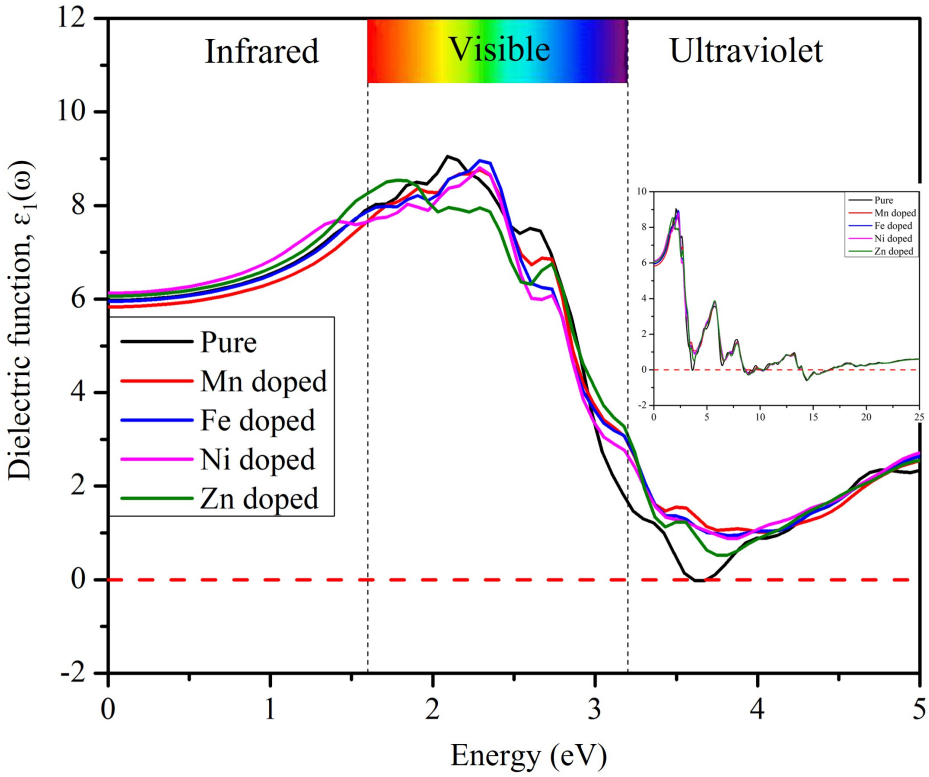


Figure 5.5: The calculated real part of the dielectric function, $\varepsilon_1(\omega)$ for undoped $CsPbI_3$ and TM doped perovskites.

The static dielectric function plays an important role in influencing charge recombination rates and overall efficiency in opto-electronic devices. It is the value of the dielectric function at 0 eV. A high static dielectric function is advantageous as it decreases charge recombination rates, consequently improving the device's efficiency [174]. The static frequency limit of dielectric function $\varepsilon_1(0)$ is observed at 5.97, 5.84, 5.96, 6.12 and 6.06 for undoped $CsPbI_3$, $CsPb_{0.875}Mn_{0.125}I_3$, $CsPb_{0.875}Fe_{0.125}I_3$, $CsPb_{0.875}Ni_{0.125}I_3$, and $CsPb_{0.875}Zn_{0.125}I_3$ perovskite materials, respectively. $CsPbI_3$ doped with Ni and Zn have a slightly greater static dielectric function than the undoped compound, suggesting that these perovskites may be more effective for use in photovoltaic devices. Furthermore, pure and TM-doped $CsPbI_3$ have dielectric functions that are high at low photon energies but reduce at high photon energies.

Past the zero frequency limit, $\varepsilon_1(\omega)$ of the compounds rises until the maximum value of 9.05 at 2.09 eV, 8.76 at 2.28 eV, 8.96 at 2.29 eV, 8.82 at 2.29 eV and 8.53 at 1.79 eV for $CsPbI_3$, $CsPb_{0.875}Mn_{0.125}I_3$, $CsPb_{0.875}Fe_{0.125}I_3$, $CsPb_{0.875}Ni_{0.125}I_3$, and $CsPb_{0.875}Zn_{0.125}I_3$ perovskite compounds, respectively. For both undoped and TM-doped, $\varepsilon_2(\omega)$ of the dielectric function demonstrated a sharp peak in the low energy region.

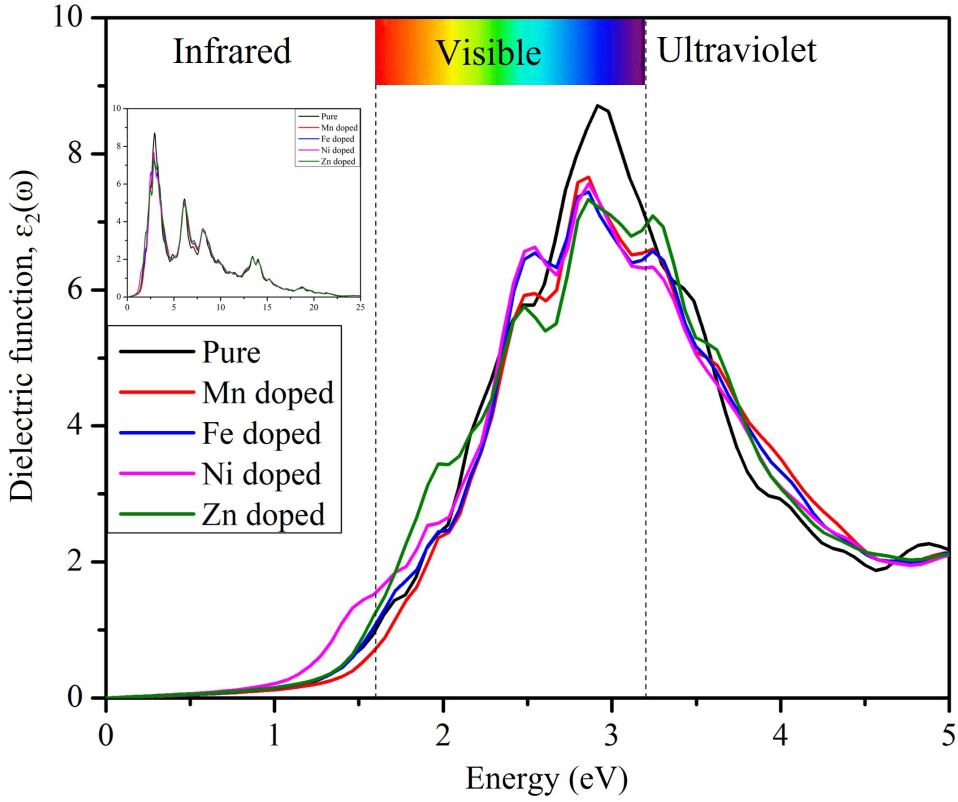


Figure 5.6: The calculated imaginary part of the dielectric function, $\varepsilon_2(\omega)$ for undoped $CsPbI_3$ and TM doped perovskites.

5.5.2 Refractive Index

The index of refraction defines the group velocity of electromagnetic waves within a material [19]. The calculated refractive index of undoped $CsPbI_3$ and TM doped is illustrated in Figure 5.7. The computed $n(\omega)$ of these compounds follows similar trend as the real part of the dielectric function. The static frequency limit $n(0)$, are 3.6 for $CsPbI_3$, 2.37 for $CsPb_{0.875}Mn_{0.125}I_3$, 2.43 for $CsPb_{0.875}Fe_{0.125}I_3$, 2.37 for $CsPb_{0.875}Ni_{0.125}I_3$ and 2.46 for $CsPb_{0.875}Zn_{0.125}I_3$ perovskites compounds as shown in the plots. It is notable that the highest peaks of the refractive index for both undoped $CsPbI_3$ and $CsPb_{0.875}TM_{0.125}I_3$ was

observed in the visible region. The compounds doped with Mn, Fe and Ni have the most intense peak compared to undoped $CsPbI_3$ meaning that they can be applied in solar cells.

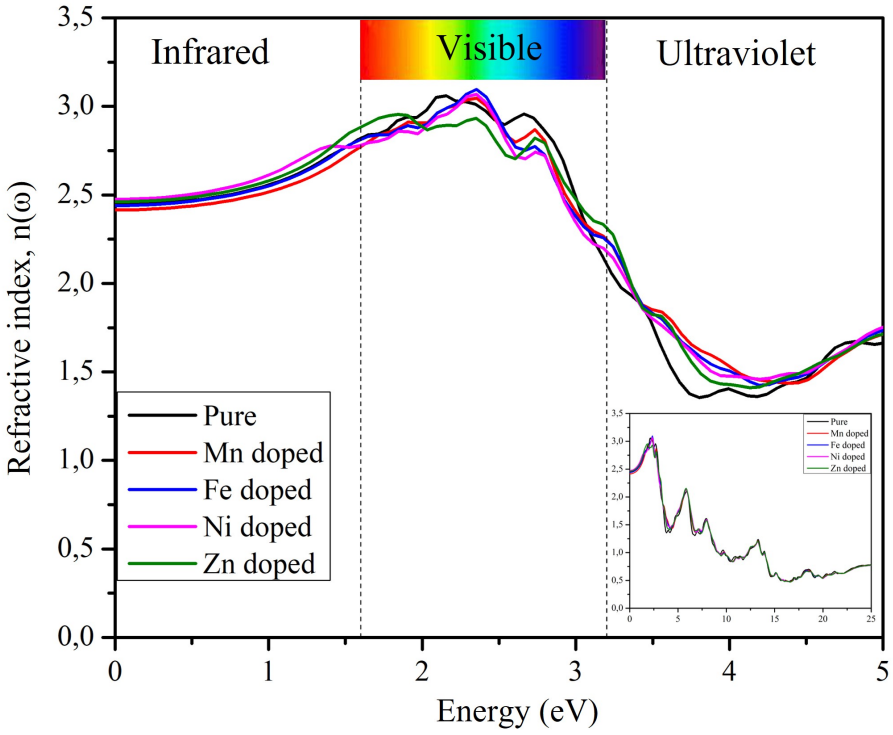


Figure 5.7: The calculated refractive index, $n(\omega)$ for the undoped $CsPbI_3$ and TM doped perovskites.

5.5.3 Extinction Coefficient

The extinction coefficient $(K(\omega))$ quantifies how actively a material absorbs photons at a specific wavelength and is proportional to a material's refractive index. Photons will be absorbed, when $(K(\omega))$ has a positive value, and a value of 0 shows that photons will pass through the material. Extinction coefficient $(K(\omega))$ plots are shown in Figure 5.8. The calculated threshold points of $(K(\omega))$ are 1.40, 1.72, 1.61, 1.35 and 1.54 eV for $CsPbI_3$, Mn-doped $CsPbI_3$, Fe-doped $CsPbI_3$, Ni-doped $CsPbI_3$, and Zn-doped $CsPbI_3$ perovskites respectively. The compounds doped with Fe and Ni have slightly higher peaks observed around 2.5 eV compared to undoped $CPbI_3$ implying that these materials are suitable for opto-electronic and photovoltaic applications.

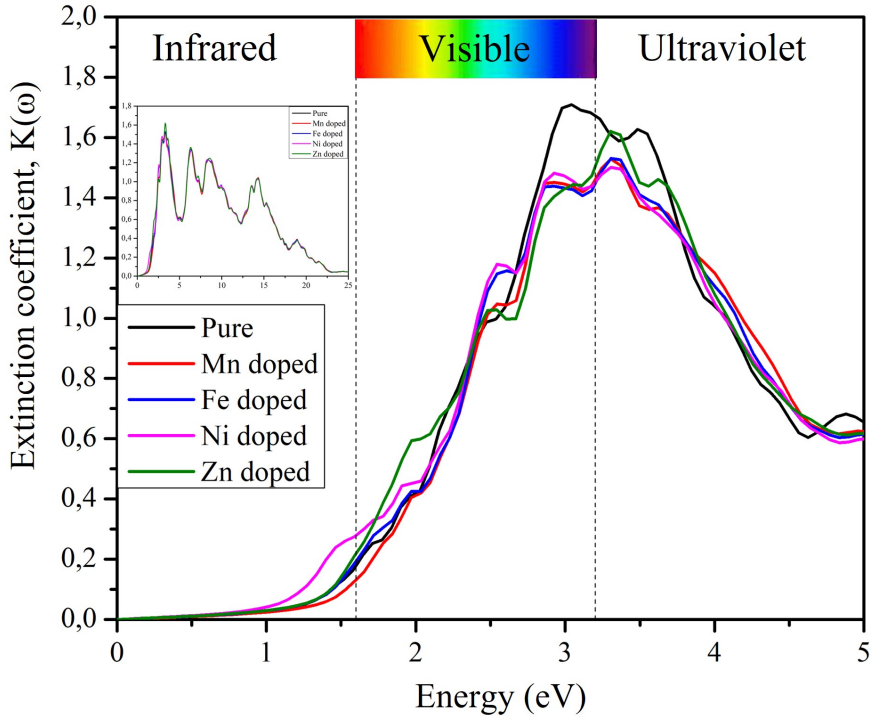


Figure 5.8: The calculated extinction coefficient of undoped $CsPbI_3$ and TM doped perovskites

5.5.4 Reflectivity

Reflectivity, $R(\omega)$ is another important optical parameter that provides information on materials applied in photovoltaic. The reflectivity, $R(\omega)$ quantifies a material's ability to reflect incident light from the surface. The reflectivity, $R(\omega)$ of the $CsPbI_3$, $CsPb_{0.875}Mn_{0.125}I_3$, $CsPb_{0.875}Fe_{0.125}I_3$, $CsPb_{0.875}Ni_{0.125}I_3$, and $CsPb_{0.875}Zn_{0.125}I_3$ perovskite compounds are illustrated in Figure 5.9. The calculated static frequency limit of reflectivity $R(0)$ were 0.165 for undoped $CsPbI_3$, 0.171 for $CsPb_{0.875}Mn_{0.125}I_3$, 0.178 for $CsPb_{0.875}Fe_{0.125}I_3$, 0.175 for $CsPb_{0.875}Ni_{0.125}I_3$, and 0.168 for $CsPb_{0.875}Zn_{0.125}I_3$ perovskite compounds. The reflectivity values for doped systems are slightly lower than undoped $CsPbI_3$ in the low energy region, suggesting that these doped compounds have potential in solar cell applications.

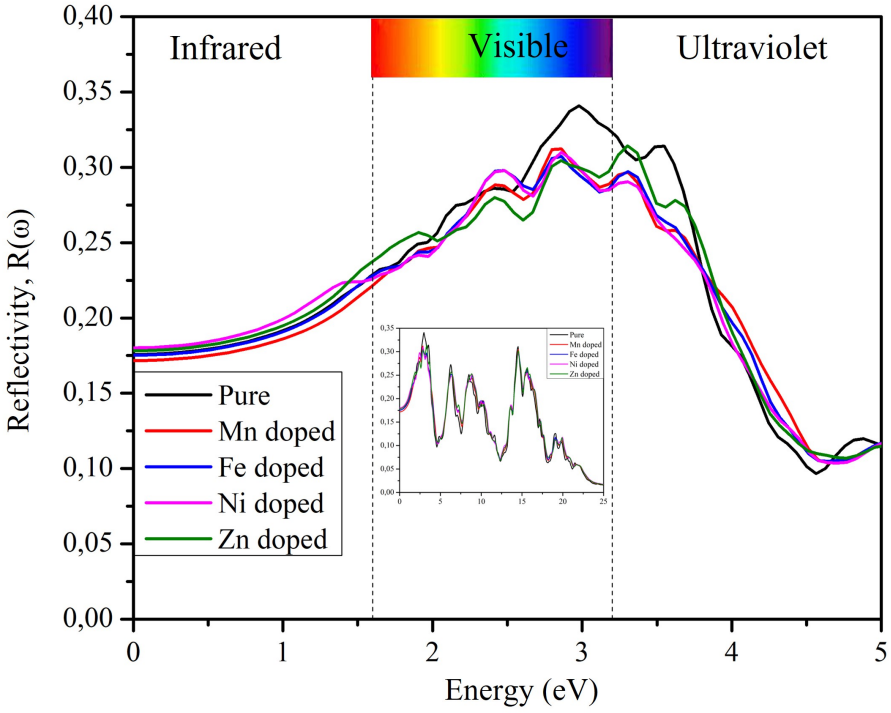


Figure 5.9: The calculated reflectivity, $R(\omega)$ of undoped $CsPbI_3$ and TM doped perovskites.

5.5.5 Conductivity

The optical conductivity denoted as $\sigma(\omega)$ and depicted in Figure 5.10 illustrates the generated current density in response to an incident photon with a specific frequency. The critical threshold was initiated at approximately 1.19, 1.91, 1.88, 1.90 and 1.86 eV for undoped $CsPbI_3$, Mn-doped $CsPbI_3$, Fe-doped $CsPbI_3$, Ni-doped $CsPbI_3$, and Zn-doped $CsPbI_3$ perovskites, respectively. The intense peaks of $\sigma(\omega)$ for undoped and TM doped were observed around 6 eV. The undoped $CsPbI_3$ compound has the most intense peak compared to TM doped materials. The doping of TM resulted in a slightly red-shifted spectral peaks position toward the lower photon energies and an increase in the peaks magnitude between 2 and 3 eV.

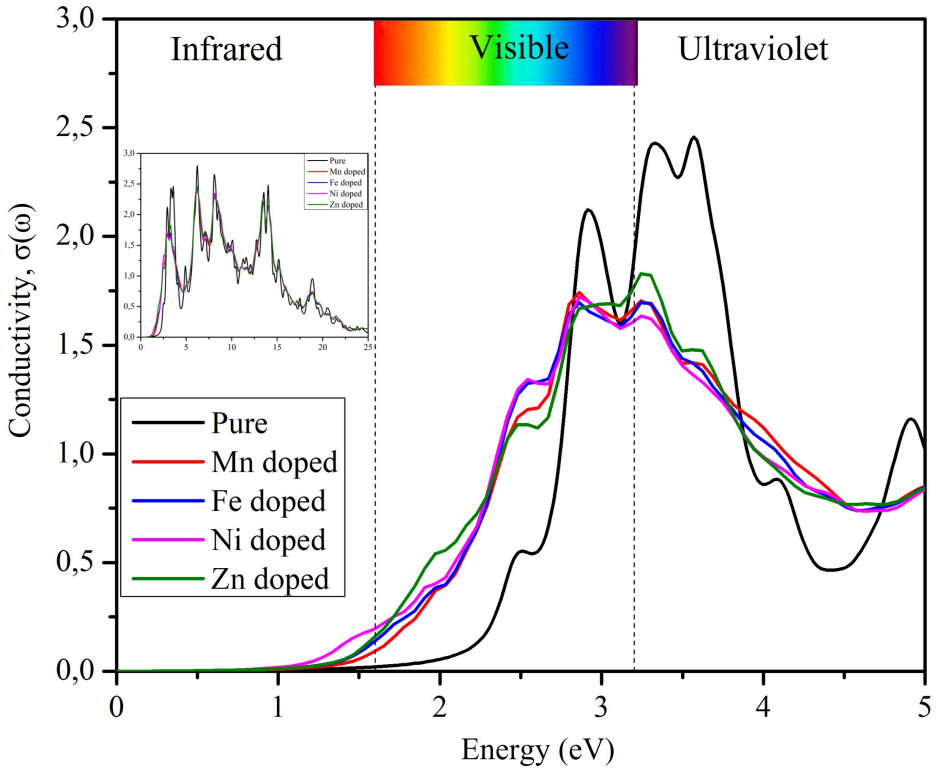


Figure 5.10: The calculated conductivity, $\sigma(\omega)$ of undoped $CsPbI_3$ and TM doped perovskites using GGA-PBE functional.

5.5.6 Absorption

The optical absorption coefficient, $\alpha(\omega)$ for undoped $CsPbI_3$, and $CsPb_{0.875}TM_{0.125}I_3$ where TM = Mn, Fe, Ni, and Zn perovskite compounds are depicted in Figure 5.11. The introduction of transition metal dopants exhibit the higher absorption peak in the low energy area compared to $CsPbI_3$, because of intermediate states, same behavior as it was observed with the electronic properties. However, in the ultra-violet region, $CsPbI_3$ has decreased. As the energy increase, the value of $\alpha(\omega)$ also rises to the highest value around 25 eV as demonstrated in Figure 5.11. Therefore, these transition metal doped $CsPbI_3$ compounds can absorb photons in the visible region of the electromagnetic spectrum, which improves the opto-electronic properties of these perovskites.

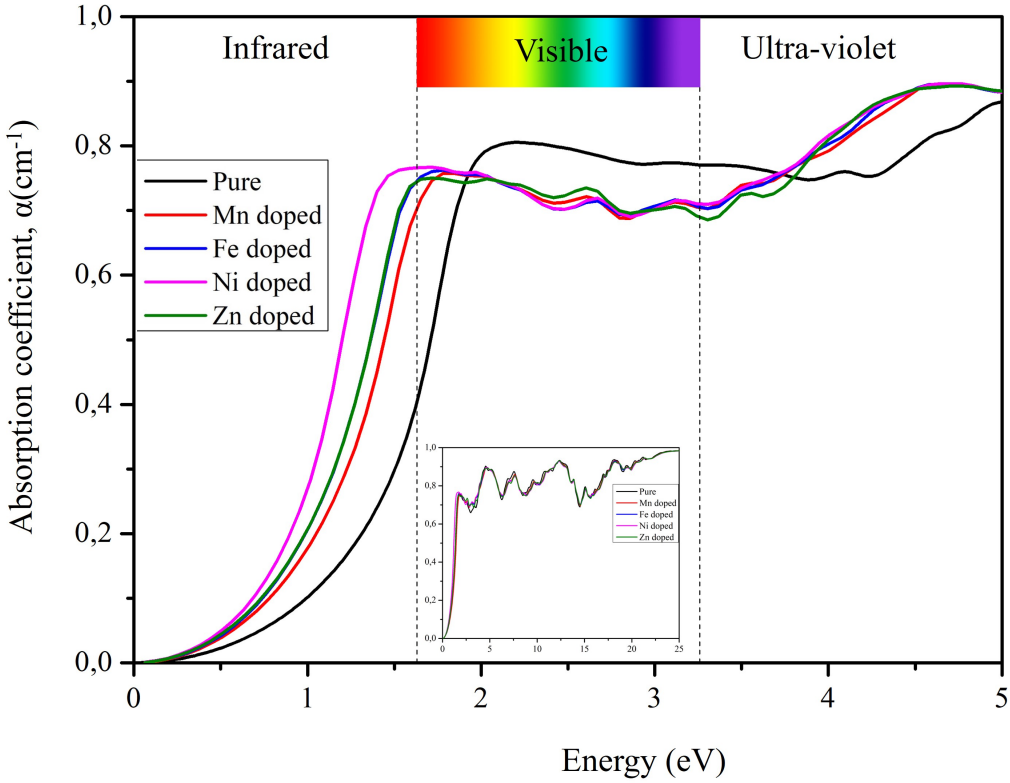


Figure 5.11: The calculated optical absorption coefficient, $\alpha(\omega)$ of the undoped $CsPbI_3$ and TM doped perovskites.

5.6 Elastic Properties

The elastic constants, C_{ij} are important parameters to determine the mechanical stability of a material. The C_{11}, C_{12} and C_{44} of $CsPbI_3$ were calculated and listed in Table 5.2 for the undoped and TM doped $CsPbI_3$. Table 5.2 results show that all these compounds satisfy the cubic Born stability criteria defined in chapter 3, indicating mechanically stability. The calculated C_{11} is greater than 40 GPa for all the compounds, following a trends of Ni > Mn > Zn > Fe. The calculated value of undoped system is 43,02 GPa, higher than literature report of 34.42 GPa obtained using standard GGA. To determine the brittleness and ductility of a material, the Cauchy pressure $(C_{12} - C_{44})$ was calculated and listed in Table 5.2. The Cauchy pressure of ductile materials is positive, whereas the Cauchy pressure of brittle materials is negative. The Cauchy pressure of the undoped and TM doped $CsPbI_3$ in Table 5.2 are all positive, indicating that these compounds are ductile in nature.

Furthermore, Table 5.3 presents the shear modulus, bulk modulus, and Young's mod-

ulus of the material approximated by Voigt-Reuss-Hill average. The small value of B for materials is an indication of the flexibility of the material. The values of B for TM-doped structures are lower than for undoped, but bit higher for Mn-doped system. Shear and Young moduli provide information on a material's stiffness, with small values for doped crystals than for undoped $CsPbI_3$, suggesting that they can easily be made into thin films for opto-electronic applications. A material is ductile above the critical values of 1.75 for B/G and 0.26 for Poisson, and brittle below. Table 5.3 shows that the values of both ratios for undoped and TM doped $CsPbI_3$ are in the ductile region, confirming that these compounds are ductile in nature.

Table 5.2: The calculated elastic contants C_{ij}, and Caunchy pressure of an undoped and TM doped $CsPbI_3$.

Compound	C_{11} (GPa)	C_{12} (GPa)	C_{44} (GPa)	C_{12} - C_{44}
$CsPbI_3$	43.02 34.41 [162]	4.92 4.71 [162]	2.86 3.35 [162]	2.06
$CsPb_{0.875}Mn_{0.125}I_3$	44.76	8.34	4.24	4.10
$CsPb_{0.875}Fe_{0.125}I_3$	40.34	7.16	4.06	3.12
$CsPb_{0.875}Ni_{0.125}I_3$	49.43	8.85	4.35	4.50
$CsPb_{0.875}Zn_{0.125}I_3$	40.71	6.11	3.28	2.83

Table 5.3: The calculated bulk modulus, shear modulus, Young's moduli, Pugh's ratio and Poisson for $CsPbI_3$ and TM doped perovskites

Compound	Bulk modulus (GPa)	Shear modulus (GPa)	Young modulus (GPa)	Poisson	Pugh's ratio
$CsPbI_3$	18.27	6.72	17.74	0.3361	2.7172
$CsPb_{0.875}Mn_{0.125}I_3$	19.80	8.75	20.01	0.3362	2.7195
$CsPb_{0.875}Fe_{0.125}I_3$	17.82	7.62	19.87	0.3229	2.3397
$CsPb_{0.875}Ni_{0.125}I_3$	18.22	6.98	18.44	0.3302	2.6108
$CsPb_{0.875}Zn_{0.125}I_3$	17.61	6.87	18.08	0.3274	2.5638

5.7 Thermodynamic Properties

The relevance of thermodynamic properties, particularly the temperature-dependent bandgap, is crucial for modeling the performance of solar power systems under different temperature conditions. Environmental temperatures significantly affect both lifespan and the efficiency of solar cells. The long-term reliability and stability of photovoltaic materials and systems can be assessed by examining their thermodynamic characteristics [175]. The fundamental concepts of thermodynamics are Debye temperature, heat capacity, entropy, enthalpy, melting temperature and free energy as demonstrated and listed in Figure 5.12 - 5.14 and Table 5.4. Heat capacity offers valuable insights into materials by revealing information about vibrational effects when subjected to heat, and it also helps determine the material's suitability for technological applications. It notable that the calculated value of θ_D for $CsPbI_3$ and $CsPb_{0.875}TM_{0.125}I_3$ are 109.2, 117.2, 116.4, 111.9 and 110.9 K, respectively, as seen in Table 5.4. The Debye temperature is low for these perovskites, they behave as low temperature resistance materials and they have low thermal conductivity.

Melting temperature is also used to differentiate between thermal softness and hardness of a material and can be calculated using independent elastic constants. The melting temperatures for $CsPbI_3$ and $CsPb_{0.875}TM_{0.125}I_3$ are as seen in Table 5.4. It is important to note that the high melting point indicates that these materials remain stable even at extreme temperatures. From this analysis, it was observed that among pure and TM doped $CsPbI_3$, $CsPb_{0.875}Ni_{0.125}I_3$ has the highest melting temperature compared to others. The heat capacity provides information about lattice vibration and phase transition. The lattice vibration that occur within a material have an effect on its temperature sensitivity.

Table 5.4: The computed average sound velocity v_s, Debye temperature θ_D, and melting temperature for undoped $CsPbI_3$ and $CsPb_{0.875}TM_{0.125}I_3$ perovskites.

Compound	Average sound velocity (v_s)	Debye temperature (θ_D)	Melting temperature (T_m)
$CsPbI_3$	1396	109.2	807.25
$CsPb_{0.875}Mn_{0.125}I_3$	1464	117.2	817.53
$CsPb_{0.875}Fe_{0.125}I_3$	1463	116.4	791.53
$CsPb_{0.875}Ni_{0.125}I_3$	1414	111.9	845.13
$CsPb_{0.875}Zn_{0.125}I_3$	1396	110.9	793.60

The temperature dependence ranging from 0 - 600 K of the specific heat capacity C_v for $CsPbI_3$ and $CsPb_{0.875}TM_{0.125}I_3$ are shown in Figures 5.12 (a) – 5.13 (a) - (d) and exhibit the same behavior throughout the considered temperature. It increases abruptly for all the materials below 150 K and then gradually slows down towards 200 K until it becomes almost constant at higher temperature. The maximum heat capacity for $CsPbI_3$, and $CsPb_{0.875}TM_{0.125}I_3$ was observed in accordance with Dulong-petit limit at high temperatures, which is approximately around 950-952 $J/mol^{-1}K^{-1}$ for TM doped materials. Enthalpy, entropy and Gibbs-free are determined temperature dependent thermodynamics properties illustrated in Figures 5.12 (b) – 5.14 (a) - (d). These figures clearly depict the trend of increasing enthalpy with rising temperature, while both free energy and entropy exhibit a decreasing trend as temperature increases.

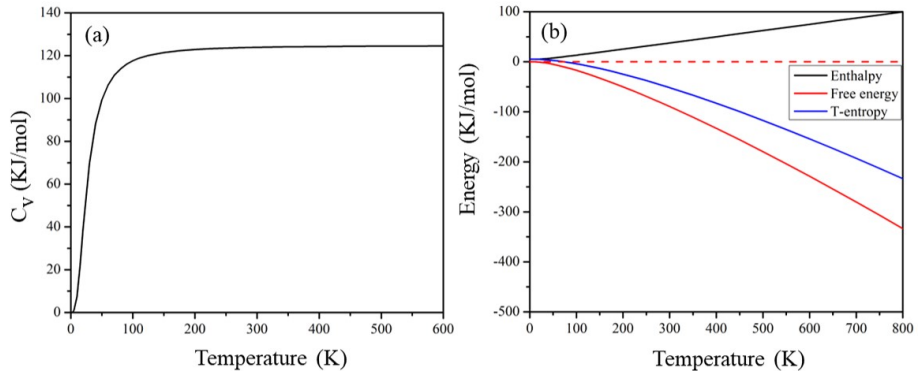


Figure 5.12: The calculated heat capacity, enthalpy, entropy and free energy against temperature for $CsPbI_3$ perovskite.

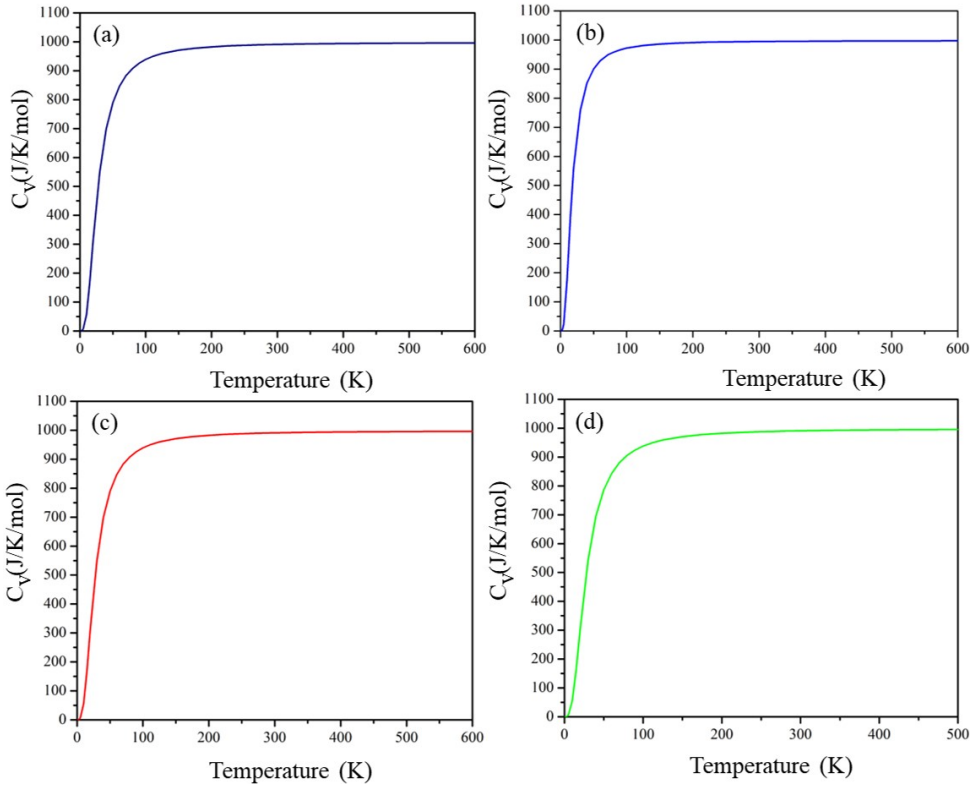


Figure 5.13: The calculated heat capacity against temperature for $CsPb_{0.875}TM_{0.125}I_3$ perovskite materials.

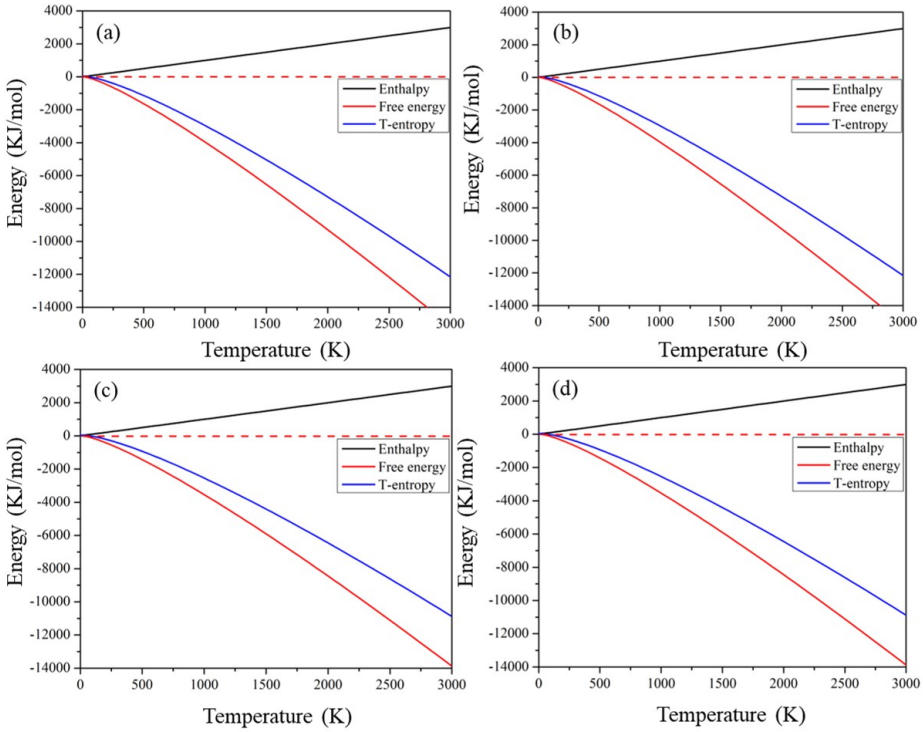


Figure 5.14: The calculated enthalpy, entropy and free energy against temperature for $CsPb_{0.875}TM_{0.125}I_3$ perovskite materials.

5.8 Summary

In summary, the structural, electronic, optical, mechanical and thermodynamics properties of the TM dopants in the $CsPbI_3$ perovskite were studied employing the first-principles DFT calculations. It was observed that the substitution of Pb atom with the TM (Mn, Fe, Ni, and Zn) reduces the lattice constants. The Pb-I bond length increases because of the smaller ionic radius of the TM than Pb. There was modification in the electronic structures after the introduction of the dopants which lead to reduced and indirect band gap. These transition metals optical absorb in the visible region with an intense $\alpha(\omega)$ compared to undoped $CsPbI_3$ and this is because of an intermediate energy band creation in the transition metal dopants band gap. The doping of TM resulted in a slightly red-shifted spectral peaks position toward the lower photon energies and an increase in the conductivity. These perovskite materials are ductile and mechanically stable. The comparative analysis of $CsPbI_3$ and $CsPb_{0.875}TM_{0.125}I_3$ where TM = Mn, Fe, Ni and Zn have demonstrated that these perovskite compounds have enhanced opto-electronic properties and may be used in the solar

cell devices notwithstanding their indirect band gap. Furthermore, an analysis of different thermodynamic parameters, including the Debye temperature, specific heat, enthalpy, entropy, and free energy was conducted and demonstration the suitability of these materials for use these material in an higher temperature. The heat capacity and entropy of these perovskite materials increases with temperature.

6

Prediction of Mixed Halides $CsPb(I/Br)_3$ Structures

6.1 Introduction

Research on material constituents mixing often concentrates on examining the stability of various phases, such as ordered intermediate ground states and end members, as well as investigating the miscibility gaps between them. Certain intermediate phases can remain stable even at high temperatures and may prove advantageous for specific applications. For some purposes, disordered solid solutions, particularly mixed halides achieved through element mixing, are preferred as they offer properties that can be adjusted easily. The perovskite structure tends to show enhanced stability in relation to phase transitions. The

impact of halides on halide-perovskites and their optical band gap is widely recognized. These halides provide an effective means of adjusting the band gap of these materials. The value of the energy band gap increases as the size of the halide decreases. For example, $CsPbI_3$ has a reported band gap of approximately 1.73 eV [58], and that of $CsPbBr_3$ is approximately 2.30 eV [28]. $CsPbBr_3$ is therefore considered less suitable for applications in photovoltaic because of this large band gap. However, the thermal stability and phase stability of $CsPbBr_3$ are better than those of $CsPbI_3$ and this has generated research interest. $CsPbBr_3$ has been utilized as an active absorber in various PSC configurations and has PCE up to 9% [176]. Most recently, there significant attention has been given to cesium lead mixed iodide and bromide perovskites ($CsPbI_{3-x}Br_x$). Various mixtures of Cs based perovskites containing bromide and iodide with improved thermal stability and reduced band gap have been tested in perovskite solar cells [41, 43]. This resulted in a notable increase in PCE reaching approximately 16% of the solar cells [43]. The substitution of bromide in $CsPbI_3$ reduces the temperature that is necessary for the formation of the $CsPbI_2Br$ black phase from 623 K to 523 K, and the $CsPbI_2Br$ exhibits improved stability compared to $CsPbI_3$. This chapter presents cluster expansion method used to predict new structures of Br doped $CsPbI_3$ and further predict their structural, electronic, optical, mechanical and thermodynamic properties.

6.2 Computational Methodology

6.2.1 Cluster Expansion

To determine the structural properties and stability of $CsPbI_{3-x}Br_x$ systems, the total energy for all the potential configurations must be calculated. Cluster expansion accounts for the energies of various atomic configurations by generating an Ising-like Hamiltonian and was used to calculate the configurational total energy. The cluster expansion method was implemented within UNCLE code [138] discussed in chapter 3. The UNCLE code progressively increases the number of clusters considered until ideal degree of precision is attained in the CE. This technique was employed to determine phase diagram and the

ground-state structure of $CsPbI_{3-x}Br_x$ systems. The CVS is provided as an indicator to evaluate the accuracy of the CE fit.

6.2.2 Monte Carlo

The UNCLE code [138] was employed to perform the Monte Carlo simulations for $CsPb(I/Br)_3$ systems. To achieve the desired precision in the average concentration of the $CsPb(I/Br)_3$ compounds, the averaging times were set to 0.1%. The Monte Carlo moves involved exchanging the positions of I^- and Br^- ions. The phase diagrams were calculated employing the canonical ensemble (NVT) with specific parameters such as system volume (V), temperature (T), and number of particles (N), as implemented in the UNCLE code. The simulations used a supercell of 25x25x25 atoms. The temperature range explored in the simulations was set from 100 K to 3200 K.

6.2.3 Geometry Optimization

First principle DFT was employed to optimize and calculate the properties of predicted structures implemented within VASP [101-104]. GGA was used as an exchange-correlation functionals [105]. The kinetic energy cut-off was 520, 550, and 500 eV with the k-points of 4 x 4 x 5, 5 x 4 x 5 and 5 x 5 x 6 for these cluster expansion predicted structures of $Cs_2Pb_2I_3Br_3$, $Cs_2Pb_2I_5Br$ and $Cs_3Pb_3IBr_8$, respectively. The convergence threshold for the total energy was set at 10^{-6} eV/atom. The compounds were considered fully optimized when forces were smaller than 10^{-4} eV/Å.

6.3 Ground States Search

To begin the ground states search of the $CsPb(I/Br)_3$ system using CE, the DFT enthalpies of formation of $CsPb(I/Br)_3$ were initially calculated. Furthermore, 42 additional structures, suggested by the genetic algorithm, were included. Using these structures, a GA was started and 2 meV cross validation score per atom was obtained. In the first run of CE, a new input structure was selected by the CE, which predicted it as a ground state. The total

energy of new structures was calculated using VASP and added to the input set. Cluster expansion predictions were modified and fitted in the procedure.

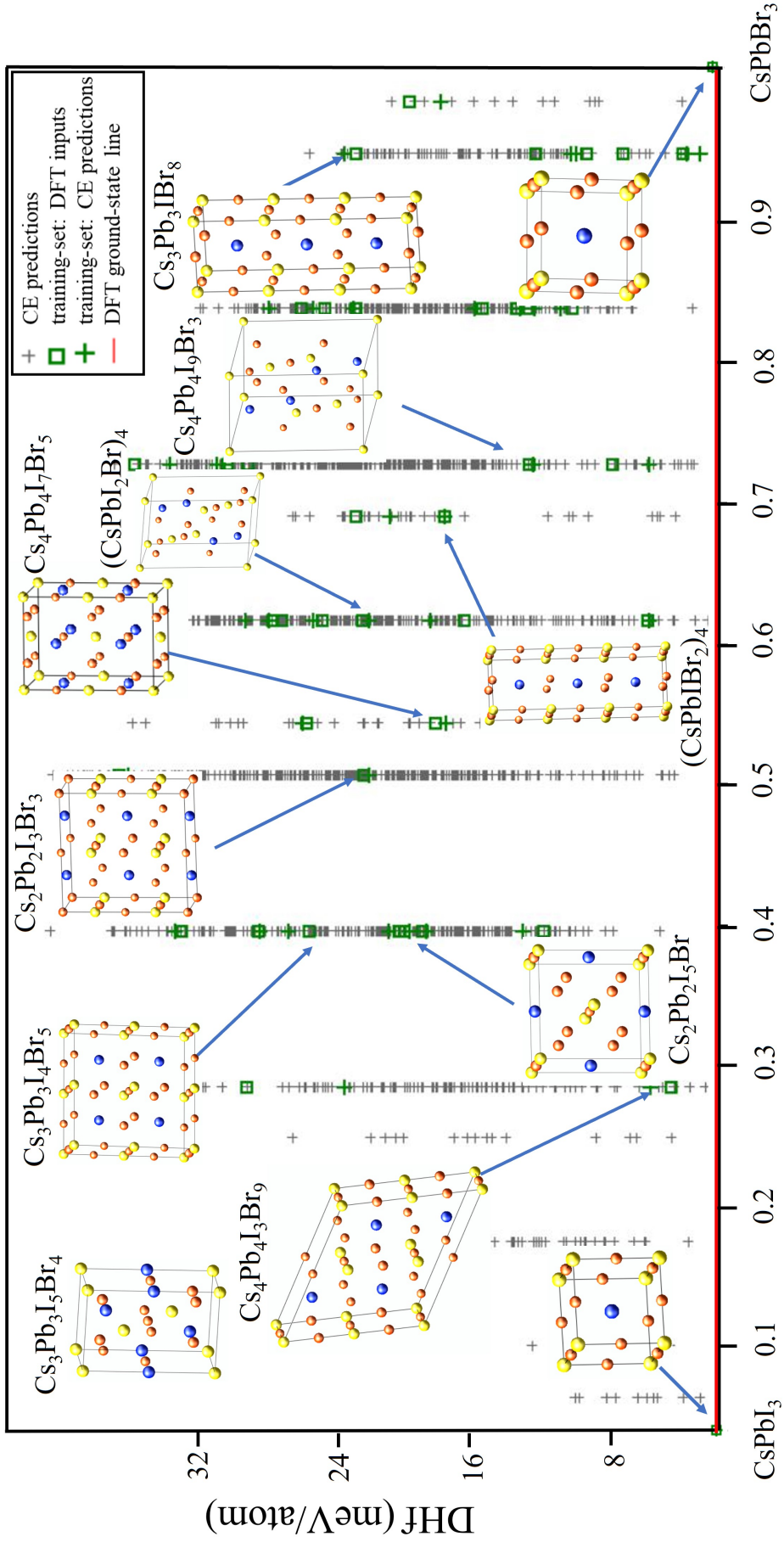
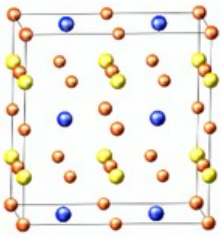
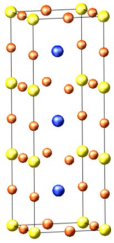
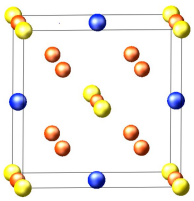


Figure 6.1: Ground state diagram of $CsPb(IBr)_3$.

The system was considered to have converged when no new ground state structures were discovered. Figure 6.1 depicts the predicted formation energies against Br concentration. The green cross represents energies predicted from the fitted CE energy functionals, green square represents energies predicted from fitted DFT inputs, black cross represents formation energies predicted by CE and red dash represents the DFT ground state line.

Table 6.1: Cluster expansion structural predicted structures $(CsPb)_xI_yBr_z$ (where x = 1 to 3 and y and z = 1 to 8) for binary system at various composition.

Compound	Atom	site	x	y	z
Cmmm $Cs_2Pb_2I_3Br_3$ 	I	4j	0	1/4	1/2
	I2	2a	0	0	0
	Br	2b	1/2	0	0
	Br2	4e	1/4	1/4	0
	Cs	4h	1/4	0	1/2
	Pb	4i	0	1/4	0
P4/mmm $Cs_2Pb_2I_5Br$ 	I	1b	0	0	1/2
	I2	4j	1/4	1/4	0
	Br	1d	1/2	1/2	1/2
	Cs	2e	0	1/2	1/2
	Cs	1a	1/2	0	1/2
	Pb	1a	0	0	0
	Pb2	1c	1/2	1/2	0
Pmmm $Cs_3Pb_3IBr_8$ 	I	2f	0	1/2	0
	Br	4i	0	1/2	0.67
	Br2	2g	0	0	0.83
	Br3	1b	0	0	1/2
	Cs	2h	1/2	1/2	0.17
	Cs2	1d	1/2	1/2	1/2
	Pb	2g	0	0	0.33
	Pb2	1a	0	0	0

6.3.1 Miscibility Gap

From Table 6.2, it is apparent that there would be variations within the calculations because of stochastic method used in the cluster expansion method. However, based on the final line of the table (4^{th} iteration), it can be inferred that the final CE includes 42 structures from the training set and with CVS of 0.65 meV/pos for the system, which is accurately enough to indicate relative energies of ordered structures. Furthermore, the CVS represents just a small fraction of the formation energy. The next column remained unpopulated until 2^{nd} iteration, implying that the optimized scheme transitioned from the miscible constituents to the miscibility gap mode. Therefore, the system with a miscibility gap has no stable structures with respect to existing pure phases.

Table 6.2: The development of an iterative procedure that lists stable structures constructed of numerous pure phases.

Elastic Iteration	No. of structures	No. of new structures	CSV score (meV/pos)
0	0	2	-
0	0	12	-
1	12	10	0.026
2	22	10	0.46
3	32	10	0.60
4	42	10	0.65

6.4 Monte-Carlo

In order to visually examine the behavior of phase segregation in $CsPbI_{1-x}Br_x$ compounds, simulation cells with fixed halides content (50.0 % concentration) underwent annealing at temperatures that varied from 0 K to 3200 K. This annealing process was carried out using the canonical ensemble simulation technique called Monte-Carlo. Observations were made of the spatial distributions of halides (I-Br) atoms within annealing simulation units. Figure 6.2 presents the spatial distribution patterns of I-Br atoms at four representative

temperatures (300 K, 500 K, 600 K and 700 K) for $CsPbI_{1-x}Br_x$ compounds, as these temperatures exhibited similar spatial morphologies. To enhance the visibility of the spatial distribution morphology, the figures include the display of Cs and Pb atoms in $CsPbI_{1-x}Br_x$ compounds. The findings suggest that a homogeneous distribution of I and Br atoms for $CsPbI_{1-x}Br_x$ may be obtained at higher temperatures. The distribution morphologies are further depicted in Figure 6.3. The figure reveals that the clustering morphology at 50 % takes a thick lamellar shape. The formation of the lamellar morphology at 50 % has been previously reported for other systems, both experimentally and theoretically [177]. The lamellar shape starts to loose shape form at 600 K, and completely dissapears at 700 K. Thus, the agglomerative cluster starts to scatter and becomes homogeneous at 700 K [178].

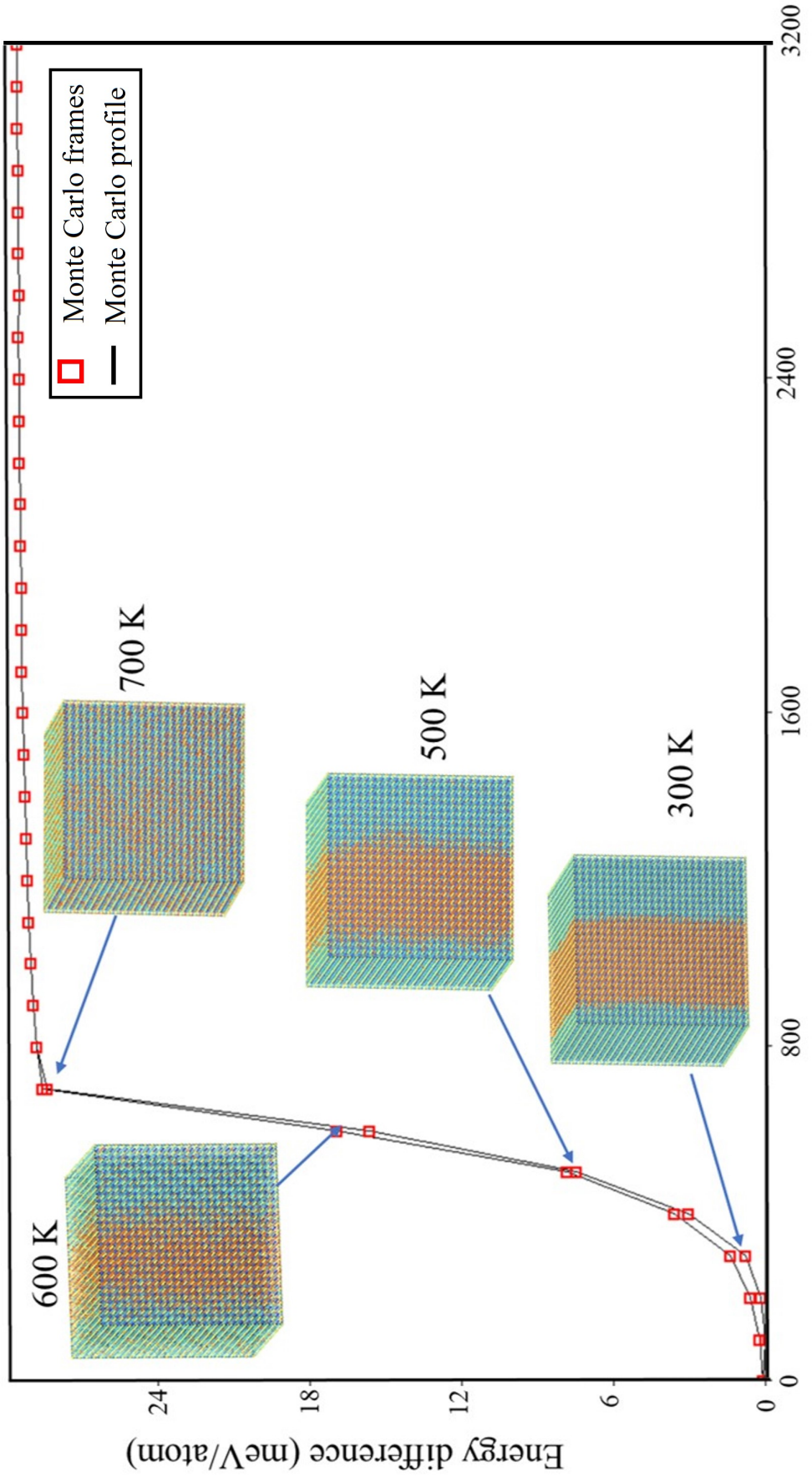


Figure 6.2: Temperature profile cross section through 25x25x25 Monte Carlo simulation for $CsPb(IBr)_3$.

From the observations depicted in Figure 6.2, it is evident that there is a segregation of I and Br halide atoms in the considered $CsPbI_{1-x}Br_x$ compounds between 300 K and 500 K. This indicates that phase segregation can occur in $CsPbI_{1-x}Br_x$ compounds, leading to the separation of $CsPbI_3$ (or I-rich $CsPbI_{1-x}Br_x$) and $CsPbBr_3$ (or Br-rich $CsPbI_{1-x}Br_x$) at a low temperature. As the temperature increases, the agglomerated clusters gradually disperse at 600 K and the spatial distribution of halides (I and Br) atoms becomes homogenous at 700 K. These findings are consistent with literature reports $CsPbI_3$ exists as non-provskite polymorph at room temperature [91]. The temperature around 590 K is at which the non-perovskite polymorph changes into the perovskite polymorph.

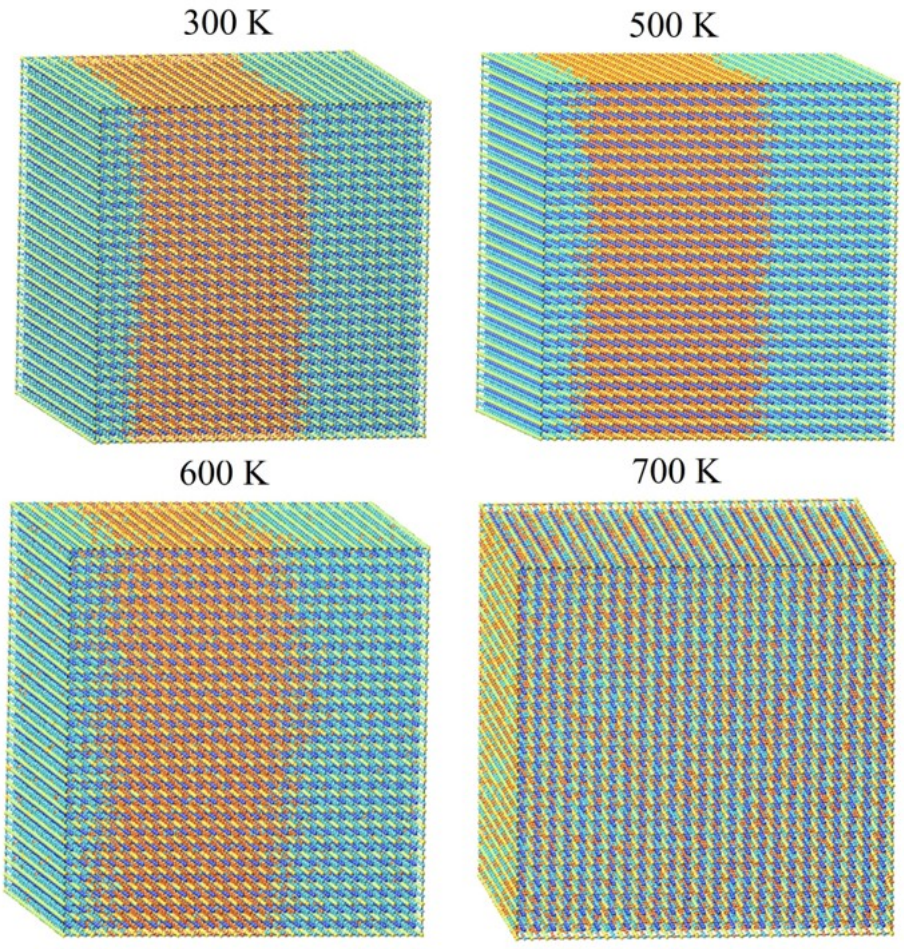


Figure 6.3: Monte Carlo simulation cells of $CsPbI_{0.5}Br_{0.5}$ at different temperature. Blue and orange balls are I and Br atoms.

6.5 Structural Properties

From the 42 structures predicted by cluster expansion, we randomly selected three structures to investigate their structural, opto-electronic, mechanical, and thermodynamic properties. The structural parameters of the selected compounds calculated are shown in Table 6.3. The random selection is mainly guided by previous studies on unconventional perovskites indicating that the perovskite formula can be altered into $A_2B_2X_6$, $A_3B_3X_9$ and $A_3B_2X_9$ phases, which we reported to be stable. The lattice constants for $Cs_2Pb_2I_3Br_3$, and $Cs_3Pb_3IBr_8$ calculated are of an orthorhombic system, where a $\neq$ b $\neq$ c whereas $Cs_2Pb_2I_5Br$ has tetragonal system lattice constants with a = b $\neq$ c, as seen in Table 6.3. The Pb-I bond length is longer compared to Pb-Br bond length for $Cs_2Pb_2I_3Br_3$, $Cs_2Pb_2I_5Br$ and $Cs_3Pb_3IBr_8$ structures which is because of the ionic radius difference of Br and I. There is no previously published experimental nor theoretical work to compare the calculated structural properties for these predicted structures.

Table 6.3: The calculated structural parameters, angle and bond length of (a) $Cs_2Pb_2I_3Br_3$, (b) $Cs_3Pb_3IBr_8$ and (c) $Cs_2Pb_2I_5Br$.

Compound	$Cs_2Pb_2I_3Br_3$	$Cs_3Pb_3IBr_8$	$Cs_2Pb_2I_5Br$
Crystal Phase	Orthorhombic	Orthorhombic	Tetragonal
Lattice constant (Å)	a = 11.973 b = 12.412 c = 6.403	a = 5.987 b = 17.967 c = 5.152	a = b = 9.044 c = 6.206
Volume ($Å^3$)	V = 951.42	V = 661.66	V = 507.57
Angle (°)	$\alpha = \beta = \gamma = 90.00$	$\alpha = \beta = \gamma = 90.00$	$\alpha = \beta = \gamma = 90.00$
Bond length (Å)	Pb - I = 3.207 Pb - Br = 2.999	Pb - I = 3.201 Pb - Br = 3.001	Pb - I = 3.194 Pb - Br = 3.103
Band gap (eV)	1.69	1.90	1.52

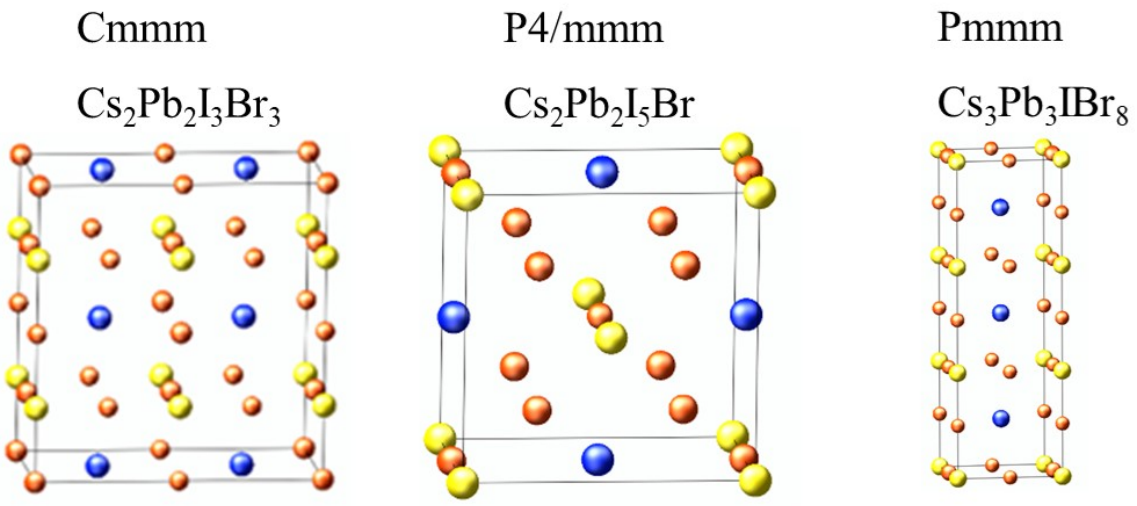


Figure 6.4: The cluster expansion predicted structure $Cs_2Pb_2I_3Br_3$, $Cs_2Pb_2I_5Br$ and $Cs_3Pb_3IBr_8$.

6.6 Electronic Properties

6.6.1 Band Structure

The calculated band structures for $Cs_2Pb_2I_3Br_3$, $Cs_2Pb_2I_5Br$ and $Cs_3Pb_3IBr_8$ are shown in Figure 6.5. For $Cs_2Pb_2I_3Br_3$ and $Cs_2Pb_2I_5Br$, the VBM and CBM were observed at Z-point and at S-point for $Cs_3Pb_3IBr_8$, indicating direct band gap materials as illustrated in Figure 6.5. The calculated band gaps of $Cs_2Pb_2I_3Br_3$, $Cs_2Pb_2I_5Br$ and $Cs_3Pb_3IBr_8$ are 1.69, 1.52 and 1.90 eV as seen in Table 6.3. Again, there are no reported experimental nor theoretical values to compare with. However, comparing these structures with the experimental band gap of $CsPbI_3$ (1.73 eV) and $CsPbBr_3$ (2.30 eV) demonstrates that mixing halogens can reduce the band gap of perovskites materials, making them suitable for solar cell application.

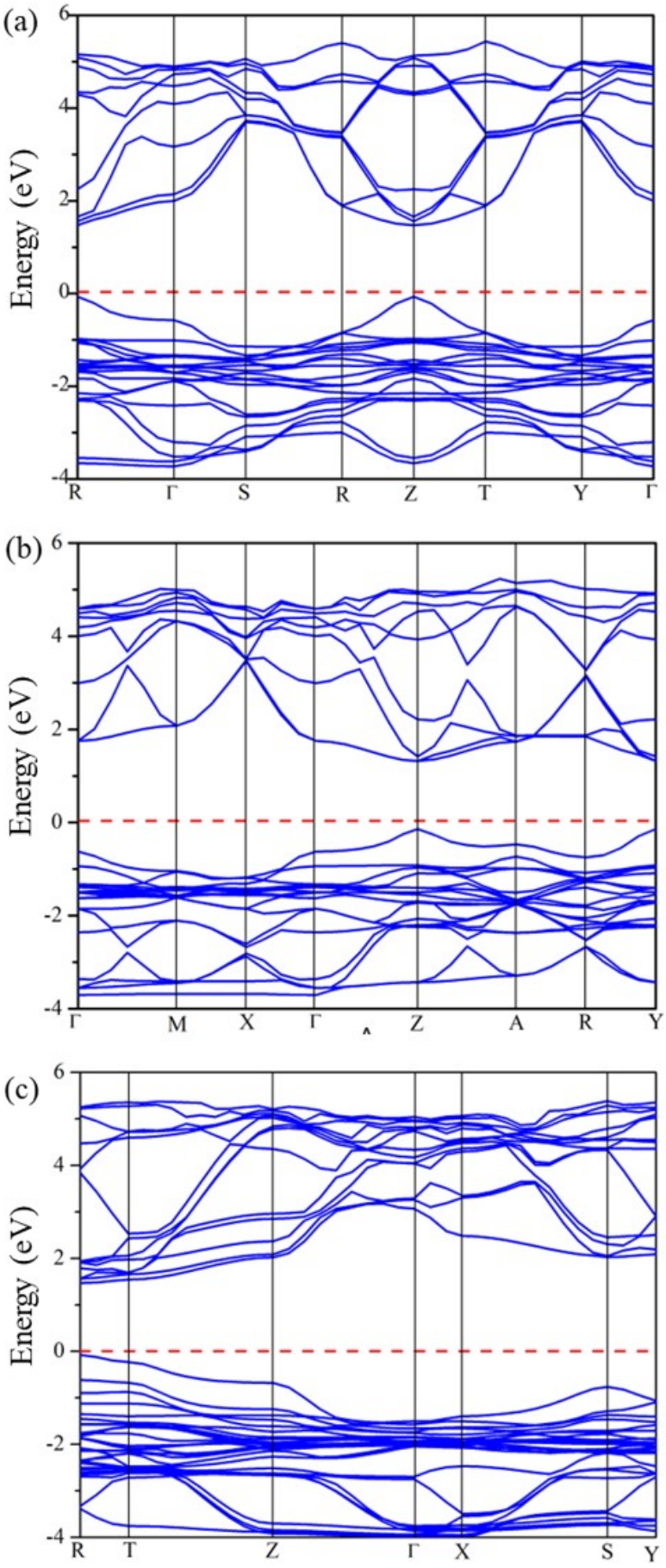


Figure 6.5: The calculated band structures of the predicted (a) $Cs_2Pb_2I_3Br_3$, (b) $Cs_2Pb_2I_5Br$ and (c) $Cs_3Pb_3IBr_8$ structures.

6.6.2 Density of States

The total and partial DOS of the predicted structures $Cs_2Pb_2I_3Br_3$, $Cs_2Pb_2I_5Br$ and $Cs_3Pb_3IBr_8$ are shown in Figure 6.6, which determine the orbital contribution of atoms to the electronic states in the VB and CB. The valence band between -15.0 eV and -5 eV is made up of halides (I-5s and Br-4s orbitals) and small contribution from Cs-5p and Pb-(4s and 4p) orbitals as depicted in Figure 6.6. The valence upper band close to the band edge (-5.0 eV to 0 eV), a contribution of Pb-(4s and 4p) and halides (I-5p and Br-4p) states is shown. The CB is mainly comprised of Pb-4p orbitals near the band edge and a small contribution from the halide atoms (I-5p and Br-4p). These halogen atoms contribute to both valence and conduction bands and this positively contributes to the electronic properties of the perovskite materials. These predicted structures have similar density of states as $CsPbI_3$ and $CsPbI_3$.

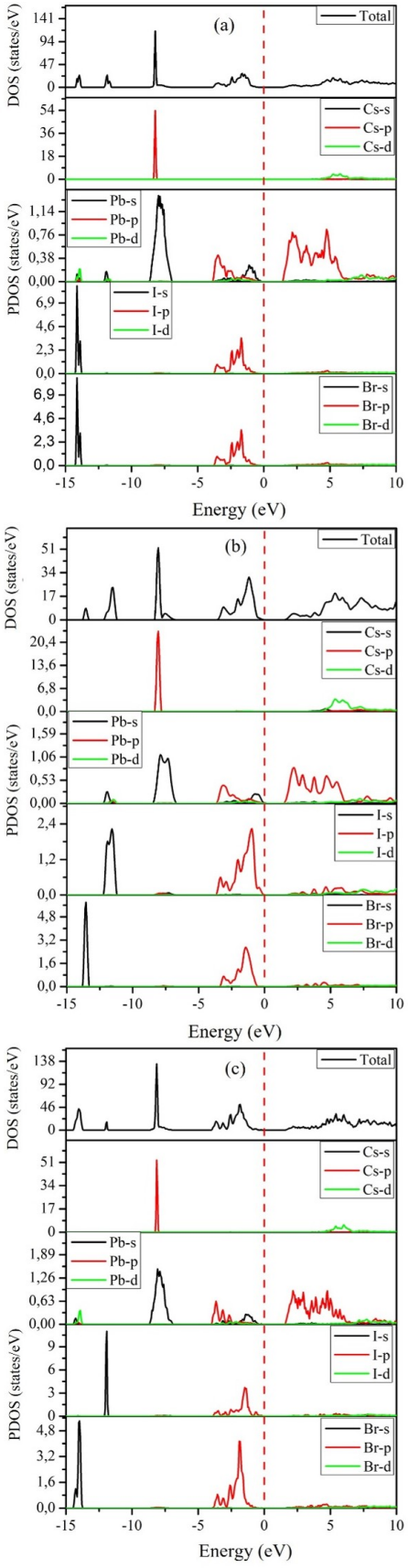


Figure 6.6: The calculated total and partial density of states for the predicted structures (a) $Cs_2Pb_2I_3Br_3$, (b) $Cs_2Pb_2I_5Br$ and (c) $Cs_3Pb_3IBr_8$.

6.7 Optical Properties

6.7.1 Dielectric Function

The dielectric function describes a material's reaction to an incident electromagnetic wave. Figure 6.7 displays the real part ε_1 calculated and plotted against frequency of the predicted structures $Cs_2Pb_2I_3Br_3$, $Cs_2Pb_2I_5Br$ and $Cs_3Pb_3IBr_8$. The static value of the ε_1 defines the amount of carrier recombination and performance of opto-electronic device [174]. The static values of the dielectric constant $\varepsilon_1(0)$ are 4.82, 5.88, and 4.80 for $Cs_2Pb_2I_3Br_3$, $Cs_2Pb_2I_5Br$ and $Cs_3Pb_3IBr_8$, respectively. These compounds display the most intense peaks at low energy (visible) region. The calculated real part maximum values were 6.95 at 2.41 eV, 8.88 at 2.26 eV, and 4.41 at 2.96 eV for $Cs_2Pb_2I_3Br_3$, $Cs_2Pb_2I_5Br$ and $Cs_3Pb_3IBr_8$ respectively. The real part dielectric function of these compounds has a higher peak in the visible region (low energy) but decreases in the ultra-violet region which demonstrates that they are suitable for solar cell devices. It is also observed that the spectral peaks of these predicted structures red shifted compared to $CsPbI_3$ and $CsPbBr_3$.

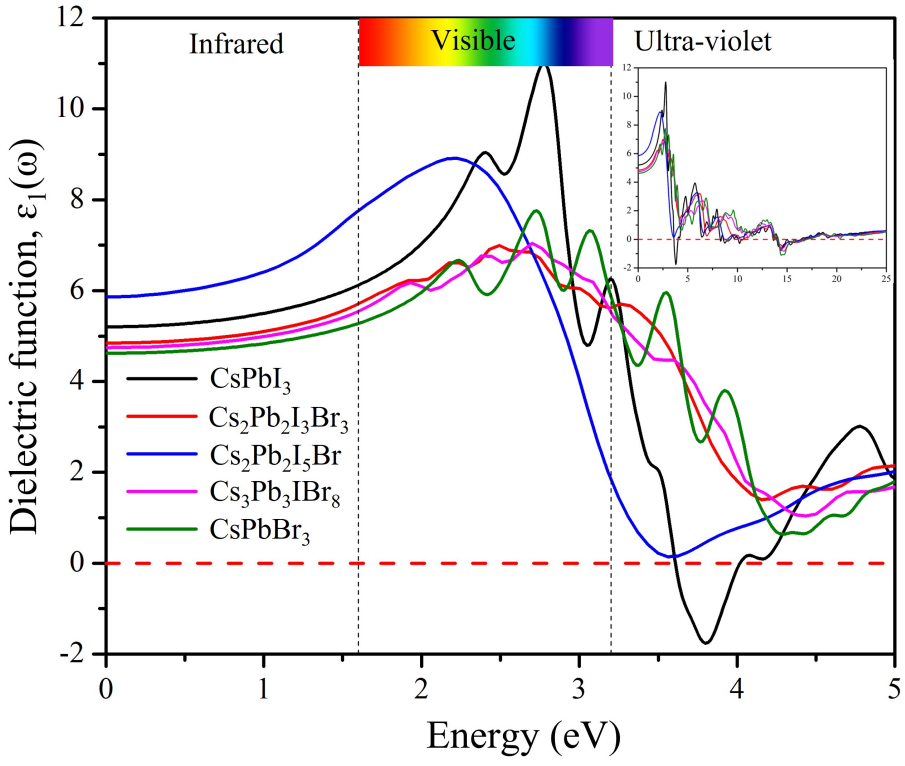


Figure 6.7: The calculated real $\varepsilon_1(\omega)$ dielectric function of the predicted structures (a) $Cs_2Pb_2I_3Br_3$, (b) $Cs_2Pb_2I_5Br$ and (c) $Cs_3Pb_3IBr_8$.

Figure 6.8 shows the imaginary part ε_2 calculated and plotted against incident photon energy for the predicted structures $Cs_2Pb_2I_3Br_3$, $Cs_2Pb_2I_5Br$ and $Cs_3Pb_3IBr_8$. The imaginary dielectric function, ε_2 begins at approximately 1.63 eV, 1.47 eV, and 1.82 eV for $Cs_2Pb_2I_3Br_3$, $Cs_2Pb_2I_5Br$ and $Cs_3Pb_3IBr_8$, respectively, which is related to the band gap of these compounds. As photon energy increases, the calculated imaginary part also increases and reaches highest peaks of 5.87 at 3.70 eV, 8.29 at 3.03 eV, and 5.53 at 3.86 eV for $Cs_2Pb_2I_3Br_3$, $Cs_2Pb_2I_5Br$ and $Cs_3Pb_3IBr_8$, respectively. Once these maximum values are reached, the ε_2 of dielectric functions begins to drop due to an increase in the energy of the photon. $Cs_2Pb_2I_5Br$ is the second most intense peak compared to others indicating that mixed halides can also improve the intensity of the imaginary dielectric function.

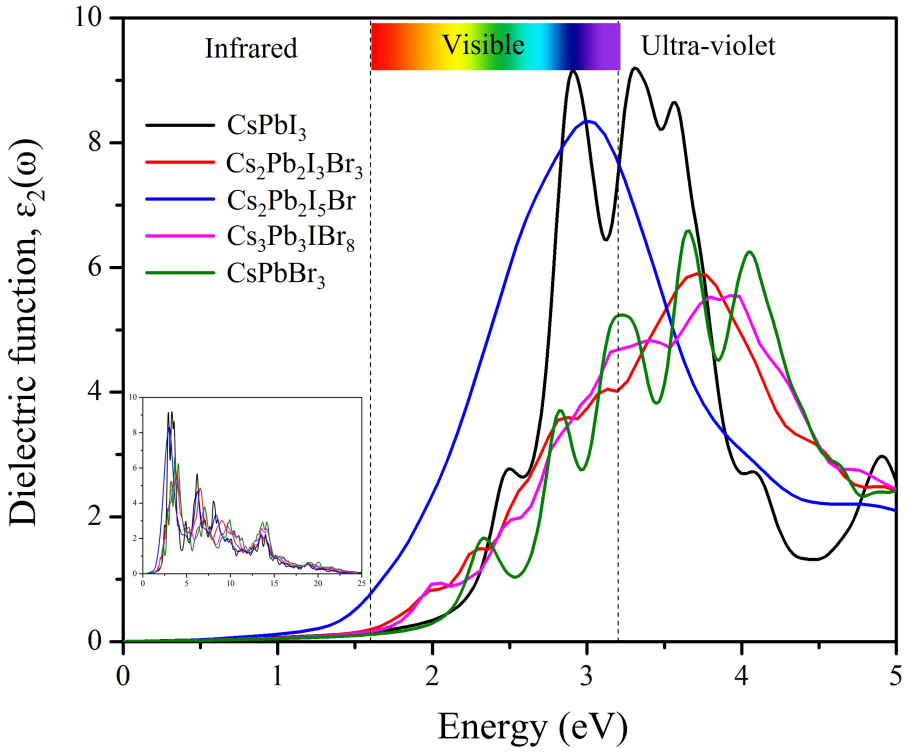


Figure 6.8: The calculated imaginary $\varepsilon_2(\omega)$ dielectric function of the predicted structures (a) $Cs_2Pb_2I_3Br_3$, (b) $Cs_2Pb_2I_5Br$ and (c) $Cs_3Pb_3IBr_8$.

6.7.2 Refractive Index

Figure 6.9 shows the calculated refractive index as a function of photon energy for the predicted cluster expansion structures $Cs_2Pb_2I_3Br_3$, $Cs_2Pb_2I_5Br$ and $Cs_3Pb_3IBr_8$. The static refractive indices $n(0)$ for $Cs_2Pb_2I_3Br_3$ is 2.20, for $Cs_2Pb_2I_5Br$ is 2.43 and for $Cs_3Pb_3IBr_8$

is 2.19. The refractive index increases and approaches the maximum value around 2.67 at 2.51 eV for $Cs_2Pb_2I_3Br_3$, 3.06 at 2.36 eV for $Cs_2Pb_2I_5Br$ and 2.69 at 2.72 eV for $Cs_3Pb_3IBr_8$. The degree of light refraction is determined by the refractive index, which is an essential parameter that is particularly useful in PV devices. The $n(\omega)$ is greater than one for all the compounds because photons interact with electrons, slow down when entering a substance. The higher the refractive index, the greater the amount of slowing down that occurs when photons travel through the material. Typically, any mechanism that increases the electron density in a substance will also increase its refractive index.$Cs_2Pb_2I_5Br$ has the most intense peak around 2 eV as compared to $CsPbI_3$ and $CsPbBr_3$, indicating that mixed halides can also improve the intensity of the refractive index.

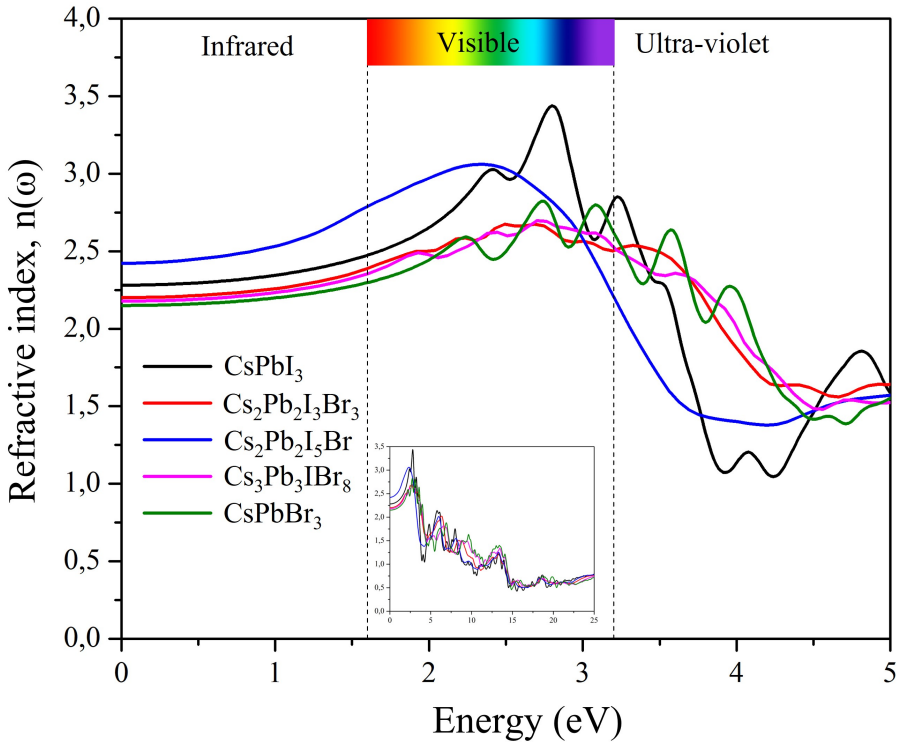


Figure 6.9: The calculated refractive index $n(\omega)$ of the predicted structures (a) $Cs_2Pb_2I_3Br_3$, (b) $Cs_2Pb_2I_5Br$ and (c) $Cs_3Pb_3IBr_8$.

6.7.3 Extinction Coefficient

The ability of a material to reduce the amount of light that passes through it is referred to as extinction coefficient, $k(\omega)$. If absorption will occur, $(k(\omega))$ will have a positive value whereas $(k(\omega)) = 0$ indicates that photons travel through the material. Figure 6.10

demonstrates the calculated extinction coefficient for the predicted structures. Imaginary part of the $n(\omega)$, is extinction coefficient $(K(\omega))$ of the materials. It is indicative of the radiation absorbed and have similar behavior as $\varepsilon_2(\omega)$. The extinction coefficient, $k(max)$ highest peaks were 1.37 at 6.71 eV for $Cs_2Pb_2I_3Br_3$, 1.73 at 3.24 eV for $Cs_2Pb_2I_5Br$ and 1.34 at 4.12 eV for $Cs_3Pb_3IBr_3$. Among the predicted structures, $Cs_2Pb_2I_5Br$ has the most intense peak in the visible region compared to $CsPbI_3$ and $CsPbBr_3$.

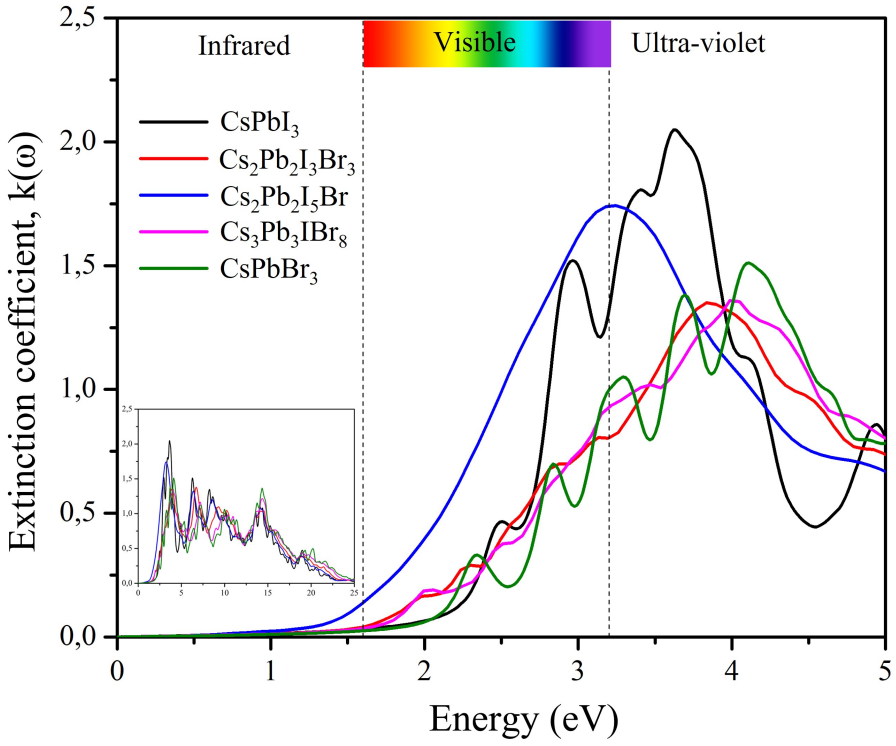


Figure 6.10: The calculated extinction coefficient $k(\omega)$ of the predicted structures (a) $Cs_2Pb_2I_3Br_3$, (b) $Cs_2Pb_2I_5Br$ and (c) $Cs_3Pb_3IBr_8$.

6.7.4 Reflectivity

For a photon of light incident on a material, we can determine how much light gets reflected using reflectivity spectra as shown in Figure 6.11, which displays the plots of $R(\omega)$ against frequency from 0 eV to 25 eV. The values of static reflectivity $R(0)$ was observed to be 0.141 for $Cs_2Pb_2I_3Br_3$, 0.174 for $Cs_2Pb_2I_5Br$ and 0.137 for $Cs_2Pb_2I_5Br$. As the photon energy increases, the reflectivity also increases and reaches maximum $R(max)$ of 0.308 at 14.699 eV for $(Cs_2Pb_2I_3Br_3)_3$, 0.339 at 3.191 eV for $Cs_2Pb_2I_5Br$ and 0.353 at 14.80 eV for $Cs_3Pb_3IBr_8$.

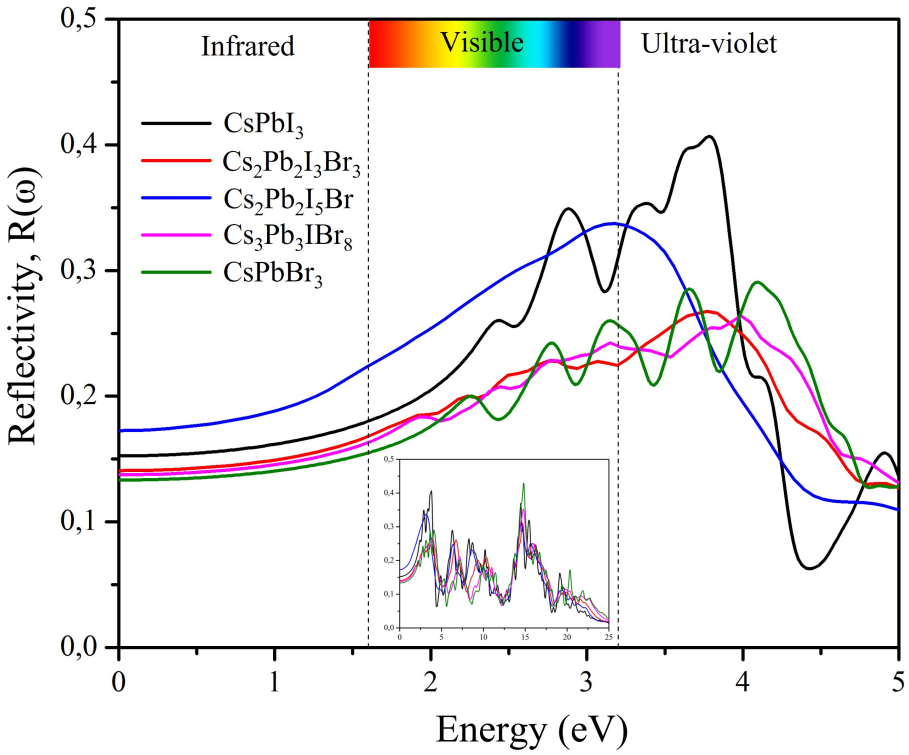


Figure 6.11: Calculated reflectivity $R(\omega)$ of predicted structures(a) $Cs_2Pb_2I_3Br_3$, (b) $Cs_2Pb_2I_5Br$ and (c) $Cs_3Pb_3IBr_8$.

6.7.5 Absorption

The amount of light at a given wavelength (energy) that enters a material before it is absorbed is measured by the substance's optical absorption coefficient [162]. It additionally gives information on the optimal solar energy conversion efficiency, which is essential for a material to be used in solar cells. Figure 6.12 depicts the absorption coefficient $\alpha(\omega)$ spectra of $Cs_2Pb_2I_3Br_3$, $Cs_2Pb_2I_5Br$ and $Cs_3Pb_3IBr_8$ as a function of photon energy. The absorption spectra demonstrate the penetration capability of photons passing through a material before absorption. The absorption spectra starts at 1.168 for $Cs_2Pb_2I_3Br_3$, 1.117 for $Cs_2Pb_2I_5Br$ and 1.169 for $Cs_3Pb_3IBr_8$, which is related to the energy band gap of the materials. The strongest peaks were observed in the ultraviolet region at 18.33, 18.28 and 12.16 eV for $Cs_2Pb_2I_3Br_3$, Cs_2PbI_5Br and $Cs_3Pb_3IBr_8$, respectively. Mixing halogens (I and Br) depicts similar peaks compared to the two compound ($CsPbI_3$ and $CsPbBr_3$) however the predicted structures optical absorption peaks red-shifted in the visible region suggesting that these materials can be applied to solar cells.

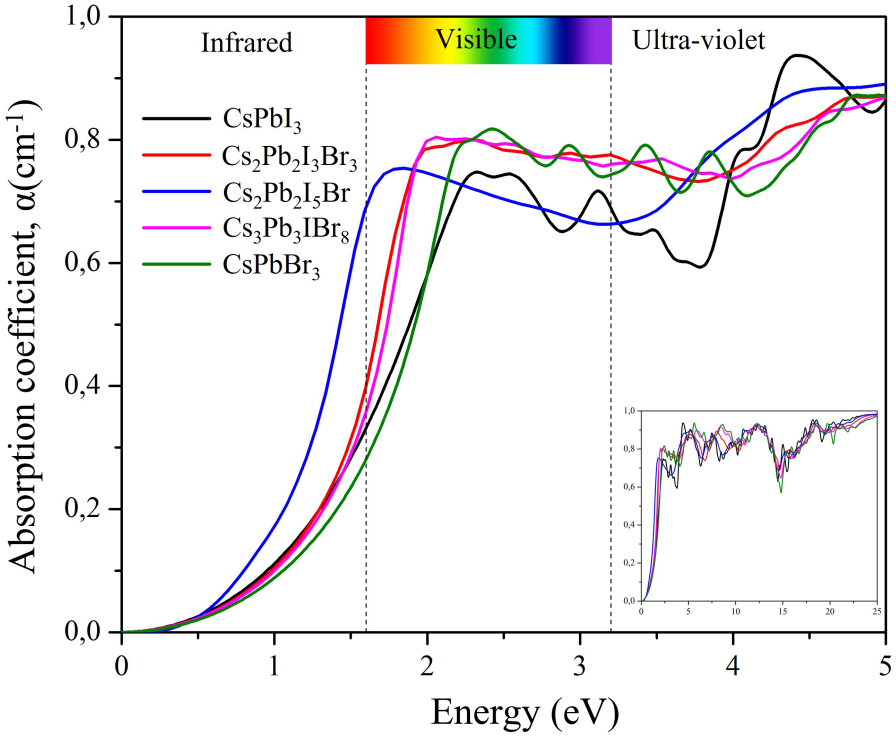


Figure 6.12: The optical absorption coefficient $\alpha(\omega)$ of the predicted structures (a) $Cs_2Pb_2I_3Br_3$, (b) $Cs_2Pb_2I_5Br$ and (c) $Cs_3Pb_3IBr_8$.

6.7.6 Conductivity

The optical conductivity showing optically activated free charge carriers of the predicted structures are shown in Figure 6.13 (a - c). It can be seen that these predicted perovskite compounds have high optcal conductivity in the high energy region. The maximum $\sigma(\omega)$ is observed at 6.55 eV for $Cs_2Pb_2I_3Br_3$, 13.51 eV for $Cs_2Pb_2I_5Br$ and 14.184 eV for $Cs_3Pb_3IBr_8$ and then started to decrease with increasing photon energy. Compared to $CsPbI_3$ that has the most intense peak, $Cs_2Pb_2I_5Br$ has the second intense peak and the spectral peak red-shifted.

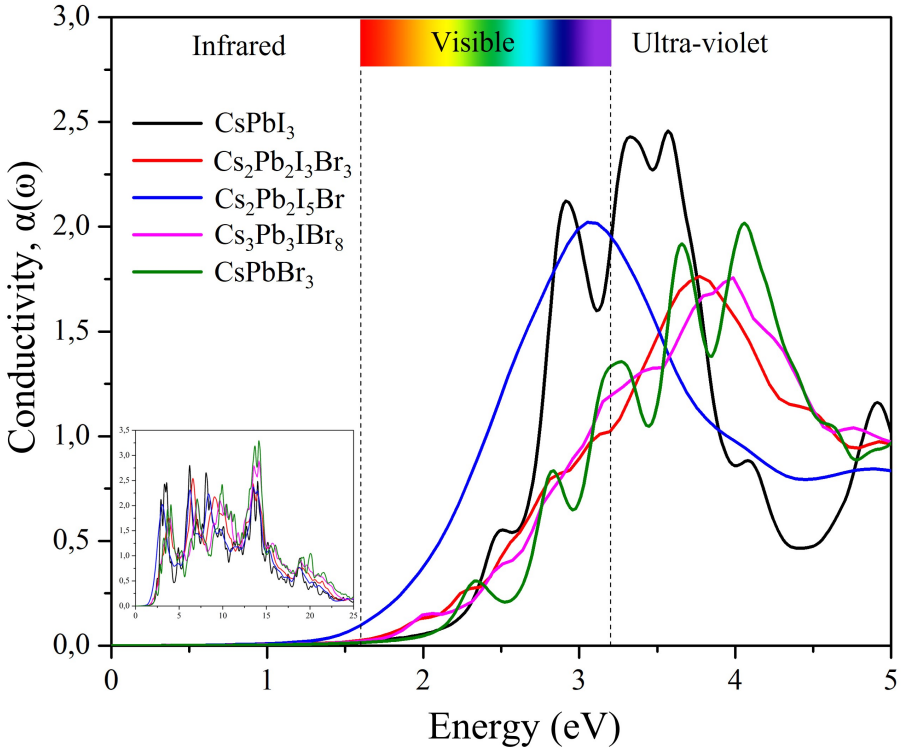


Figure 6.13: The optical conductivity $\sigma(\omega)$ of the predicted structures (a) $Cs_2Pb_2I_3Br_3$, (b) $Cs_2Pb_2I_5Br$ and (c) $Cs_3Pb_3IBr_8$.

6.8 Elastic Properties

The $Cs_2Pb_2I_5Br$ material belongs to the tetragonal system and has six independent elastic constant C_{11}, C_{12}, C_{13}, C_{33}, C_{44} and C_{66}, while $Cs_2Pb_2I_3Br_3$ and $Cs_3Pb_3IBr_8$ belong to orthorhombic system with nine elastic constants C_{11}, C_{12}, C_{13},C_{22}, C_{23}, C_{33}, C_{44}, C_{55} and C_{66} demonstrated in Table 6.4. These elastic constants determine the mechanical stability of compounds as discussed in chapter 3, equations (3.65) and (3.70). Using these equations, the elastic constants of these structures were determined and suggest that these predicted structures are mechanically stable.

Table 6.4: The calculated elastic constants C_{ij} of (a) $Cs_2Pb_2I_3Br_3$, (b) $Cs_2Pb_2I_5Br$ and (c) $Cs_3Pb_3IBr_8$.

Elastic Constants	$Cs_2Pb_2I_3Br_3$	$Cs_2Pb_2I_5Br$	$Cs_3Pb_3IBr_8$
C_{11}	41.92	39.60	23.29
C_{12}	6.39	6.11	16.49
C_{13}	5.96	5.24	5.16
C_{22}	41.78	37.72	-
C_{23}	5.96	4.84	-
C_{33}	40.37	35.89	36.92
C_{44}	3.97	3.45	3.75
C_{55}	4.02	3.79	-
C_{66}	4.43	4.67	15.22

The parameters G and B moduli are crucial characteristics of crystals that demonstrate their capability to resist compression and shear deformations. Table 6.5 presents the elastic constants, G, B, Y, v, and Pugh's ratio of the predicted structures $Cs_2Pb_2I_3Br_3$, $Cs_2Pb_2I_5Br$ and $Cs_3Pb_3IBr_8$. It is evident that $Cs_2Pb_2I_3Br_3$ has a high G, B, and Y moduli. This indicates that the $Cs_2Pb_2I_3Br_3$ compound has relatively good resistance to deformation, a good capability to resist shear strain, and good rigidity. All of the B/G and Poisson ratios for these materials are higher than 1.75 and 0.26, indicating that they are ductile [179]. The results also show that the material $Cs_2Pb_2I_3Br_3$, has the highest ductility other two predicted perovskite materials and it is simple to produce into thin films.

Table 6.5: The calculated bulk, shear, Young's moduli, Pugh's and Poisson ratio of (a) $Cs_2Pb_2I_3Br_3$, (b) $Cs_2Pb_2I_5Br$ and (c) $Cs_3Pb_3IBr_8$.

Elastic Constants	$Cs_2Pb_2I_3Br_3$	$Cs_3Pb_3IBr_8$	$Cs_2Pb_2I_5Br$
Bulk	17.85	16.16	15.23
Shear	7.74	7.23	6.77
Young	20.17	18.77	17.59
Poisson	0.3105	0.3053	0.3063
Pugh	2.3057	2.2348	2.2480

6.9 Thermodynamic Properties

The calculated entropy, free energy, enthalpy, and heat capacity against temperature are presented in Figure 6.14. Entropy refers to level of disorder of a material, and the middle lines in Figure 6.14 (d-f) demonstrate the product of entropy and temperature for these materials. The thermal motion of compounds increases, as the temperature rises resulting in high degree of disorder, entropy and temperature. The top solid lines in Figure 6.14 (d-f) demonstrate materials enthalpy, which increases with increasing temperature as all three quantities (U, P, and V) increase. The bottom three curves in Figure 6.14 show the free energy of the compound, which may be expressed as F = U - TS. However, both U and TS increase with increasing temperature, the increase in TS is greater, resulting in an increase in the value of TS-H. As the temperature increases, the value of H-TS decreases and hence, F = U - TS decreases with increasing temperature.

The C_v of a material is composed of contributions from lattice vibration, and electron motion. Figure 6.14 illustrates the variation of heat capacity with temperature. The heat capacity of these predicted structures increases rapidly below 200 K in accordance with the T^3 Law of the Debye Model at low temperatures. At higher temperatures, C_v increases slowly and until the Dulong-Petit limit [180].

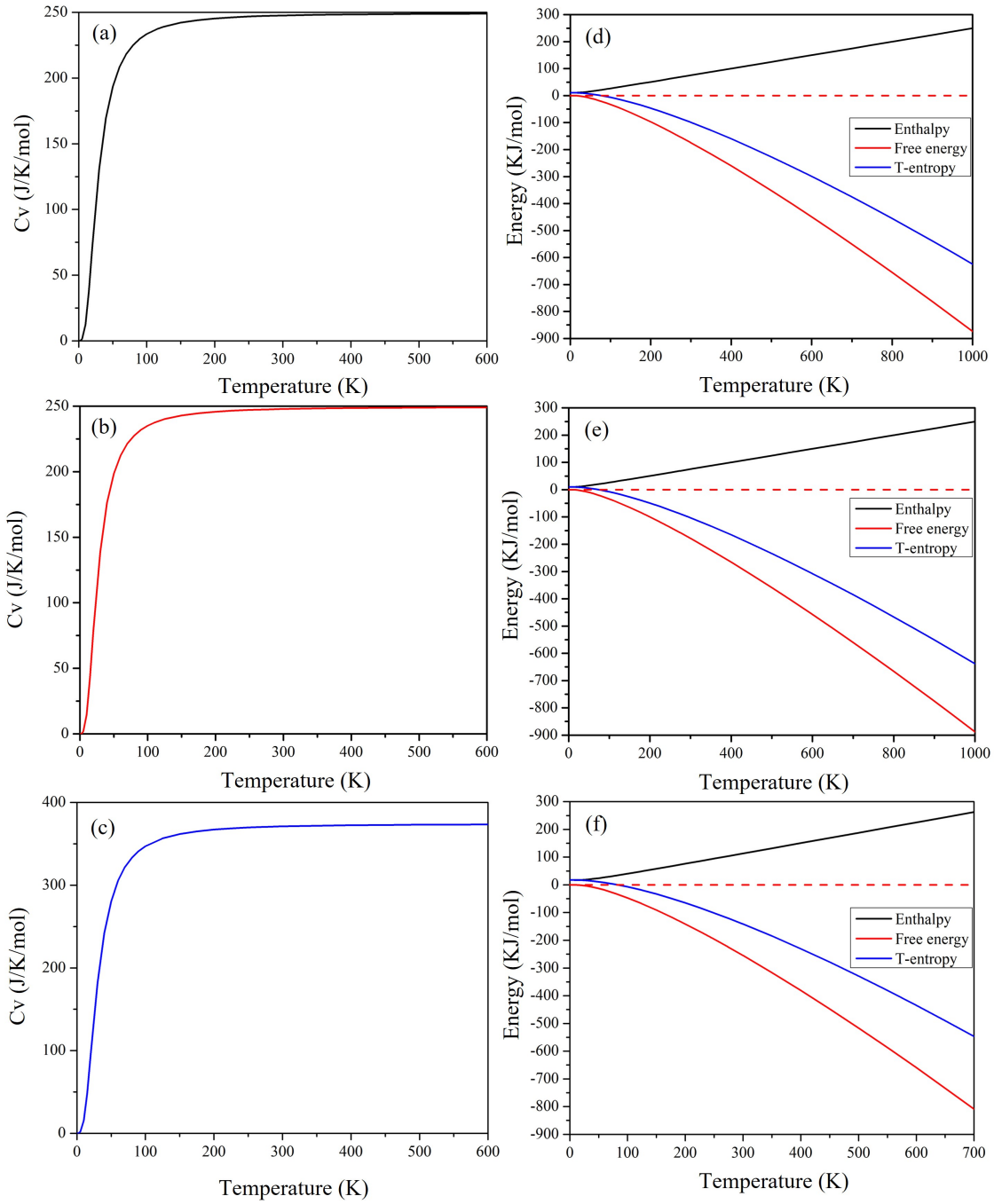


Figure 6.14: Temperature dependence of heat capacity of (a) $Cs_2Pb_2I_3Br_3$, (b) $Cs_2Pb_2I_5Br$ and (c) $Cs_3Pb_3IBr_8$ perovskites and their (d) - (e) enthalpy, temperature entropy, and free energy.

6.10 Summary

The combined methods including cluster expansion, Monte Carlo and DFT were employed to study the ground state search and phase stability of $(CsPb)_xI_yBr_z$ (where x = 2 or 3 and

y and z = 1 to 8) materials. To conduct Monte Carlo calculations, a set of effective cluster interactions, capable of providing an accurate formation energy for ordered $CsPbI_{1-x}Br_x$ configurations, was initially established within the cluster expansion framework. There were 42 new ordered phases that were generated from a binary phase diagram. These newly generated phases demonstrated a miscibility gap because of thermodynamically unstable and phase separation. To further study the thermodynamic properties and phase separation at different temperature for $CsPbI_{1-x}Br_x$ at 50 % concentrations, Monte Carlo method was used. The electronic properties show that $Cs_2Pb_2I_3Br_3$, $Cs_2Pb_2I_5Br$ and $Cs_3Pb_3IBr_8$ are semiconductors with energy band gap values between 1.60, 1.59 and 1.90 eV, respectively. The optical properties demonstrated a strong ability of photon absorption because of their narrow band gap materials. In all of these predicted perovskite materials, specific heat capacity at low temperature obeys Debye law and at high temperature approaches the Dulong-petit limit. The comparative analysis of predicted structures with $CsPbI_3$ and $CsPbBr_3$, demonstrated that the opto-electronic properties of the perovskite materials are enhanced with the mixed halides and can be used in solar cell applications.

7

Conclusion and Future Work

7.1 Conclusion

The structural, electronic, optical, mechanical and thermodynamic properties of B-site and X-site doped $CsPbI_3$ were successfully studied using the first-principle calculations. The computed lattice constants are in good agreement with both previous theoretical and experimental results. The electronic band structures and DOS analyses revealed that the $CsPbI_{3-x}Br_x$ (x = 0,1,2,3) perovskite compounds are direct band gap semiconductors, as predicted by all GGA, SCAN and LDA functionals. The opto-electronic properties, which describe the nature of valence band and conduction band edges are governed by contributions from the ions on the B-site and X-site of ABX_3 perovskite. The electronic band gap of $CsPbI_3$ was engineered by gradually replacing I^- ion with Br^- ions, which led to the formation of $CsPbI_2Br$, $CsPbBr_2I$, and $CsPbBr_3$ materials. The calculated energy band gaps were increasing with increasing content of Br^- ions. For example, in the case of SCAN meta-GGA exchange correlation functional, energy band gap increased in this order: 1.449 eV> 1.470 eV> 1.588 eV> 1.876 eV for $CsPbI_3$, $CsPbI_2Br$, $CsPbBr_2I$, and $CsPbBr_3$, respectively. Previous studies reported that lower energy band perovskite materials have lower exciton binding energy. The undoped $CsPbI_3$ has the lowest energy band gap, suggesting that it is more thermally stable. However, its binding energy might be lower, resulting in lower power conversion efficiency. The investigation revealed that these perovskite materials displayed mechanical stability, ductility, and elastic anisotropy. Various optical properties such as dielectric function, refractive index, conductivity, re-

flectivity, extinction coefficient and optical absorption coefficients were also determined and analyzed. These optical properties have demonstrated that these perovskite materials absorb in the visible region. The mechanical properties of these perovskite compounds show that these materials are ductile in nature because their calculated bulk modulus is low, ranging between 15.09 GPa – 18.85 GPa for GGA, 14.13 GPa – 22.17 GPa for SCAN meta-GGA, 20.59 GPa – 25.70 GPa for LDA. The ratio of bulk to shear, and Poisson ratio of the materials $CsPbI_3$, $CsPbI_2Br$, $CsPbBr_2I$, and $CsPbBr_3$ revealed that they are ductile. Three indicators verified the ductility of these materials i.e., Pugh's ratio, Cauchy pressure and Poisson's ratio. The energy-dependent optical parameters, especially the absorption coefficient in the visible-infrared regions and direct band gap , indicate that these perovskite materials may be good for use in photovoltaic opto-electronic and solar cell applications. Different thermodynamic parameters including Debye temperature, specific heat, enthalpy, Gibbs-free energy, and entropy are examined,The maximum heat capacity for $CsPbI_3$, $CsPbI_2Br$, $CsPbBr_2I$ and $CsPbBr_3$ are 120.26, 121.23, 120.83, and 120.34 $J/mol^{-1}K^{-1}$, respectively. It was observed that the heat capacity reaches the Dulong-Petit limit at higher temperatures. It further demonstrates that when the temperature approaches zero, the three thermodynamic parameters decreased, which is consistent with the third law of thermodynamics.

Furthermore, to resolve the issues related to the presence Pb^{2+} toxicity in all-inorganic halide perovskites, $CsPbI_3$ was doped with a smaller percentage (i.e., 12.5 % doping concentration) of transition metals, Mn^{2+}, Fe^{2+}, Ni^{2+} and Zn^{2+}. The structural, electronic, optical, mechanical and thermodynamic properties of $CsPb_{0.875}TM_{0.125}I_3$ (TM = Mn, Fe, Ni, and Zn) were investigated using DFT. To correct the strong Coulomb interactions of the 3d electrons of the transition metals, spin polarized GGA+U was used. When a transition metal replaces a Pb atom, the bond length and lattice constants contract because transition metals have smaller ionic radii than Pb. The direct band gap of $CsPbI_3$ calculated were 1.488 eV, while all TM-doped $CsPbI_3$ perovskites exhibited an indirect band gap with reduced energy band gap notwithstanding the inclusion spin polarized hybrid functional. Doping with the transition metals enhanced the absorption in the visible region, but it was low in the ultra-violet region compared to $CsPbI_3$, making them good candidates for use in solar cell applications. However, reduced energy band gap is not favorable for photovoltaics application. The results on reduced band gap when doped with transitional metals are consistent with literature results. According to the calculated elastic properties, these compounds were discovered to be ductile and mechanically stable. Thermodynamics properties such as specific heat capacity exhibit the same behavior for pure and TM doped $CsPbI_3$ throughout the considered temperature. Debye temperature is low for these perovskites, they behave as low temperature resistance materials.

Lastly, cluster expansion was used to investigate the mixed $CsPb(IBr)_3$ phase stabilities and to determine the phase changes using Monte-Carlo simulations. The cluster expansion

calculations generated 42 new stable $(CsPb)_xI_yBr_z$ (where x = 1 to 3 and y and z = 1 to 8) structures that contained multiple components and ranked as the metastable structures based on their enthalpy of formation. The simulations involved exchanging the positions of I and Br atoms to find stable structures. In addition, Monte Carlo simulations were employed to determine the thermodynamic properties of these $CsPb(IBr)_3$ compounds for the 50 % concentrations obtained from the cluster expansion. The simulations demonstrated that $CsPbI_{0.5}Br_{0.5}$ is a system that separates into different phases at 300 K but changes to homogenous phases as the temperature increases to 700 K. Three of the predicted ground state structures $Cs_2Pb_2I_3Br_3$, $Cs_2Pb_2I_5Br$ and $Cs_3Pb_3IBr_8$ were randomly selected and further investigated by calculating their structural, opto-electronic, mechanical, and thermodynamics properties using DFT. The electronic structures indicated that all the predicted structures are direct band gap semiconductors. The calculated energy band gap of $Cs_2Pb_2I_3Br_3$, $Cs_2Pb_2I_5Br$ and $Cs_3Pb_3IBr_8$ are 1.69 eV, 1.52 eV and 1.90 eV, respectively. The calculated optical properties of $Cs_2Pb_2I_3Br_3$, $Cs_2Pb_2I_5Br$ and $Cs_3Pb_3IBr_8$ exhibited similar properties as those of Br doped cubic $CsPbI_3$. The elastic properties demonstrated that these predicted structures are ductile in nature and mechanically stable. These findings demonstrated that mixed halide perovskites can modify the band gap and enhance structural stability, making them good candidates for photovoltaic applications.

7.2 Future Work

(i) Incorporate spin-orbit coupling (SOC) in the calculations, especially important for heavy elements like Pb and I, to accurately capture their relativistic effects on electronic structure.
(ii) Use molecular dynamics (MD) or other dynamic simulation techniques to study the behavior of doped $CsPbI_3$ at finite temperatures. Investigate the role of thermal vibrations on the stability and properties of the material.
(iii) Study the interfaces between doped $CsPbI_3$ and other materials used in device architectures (e.g., electron/hole transport layers). Understand how interfacial properties affect device performance.

A

Appendix

Figure A1 and A2 represents the total and partial density of states for CsPbI, $CsPbI_2Br$, $CsPbIBr_2$ and $CsPbBr_3$ perovskites using LDA and GGA functionals , that were not shown in chapter 3.

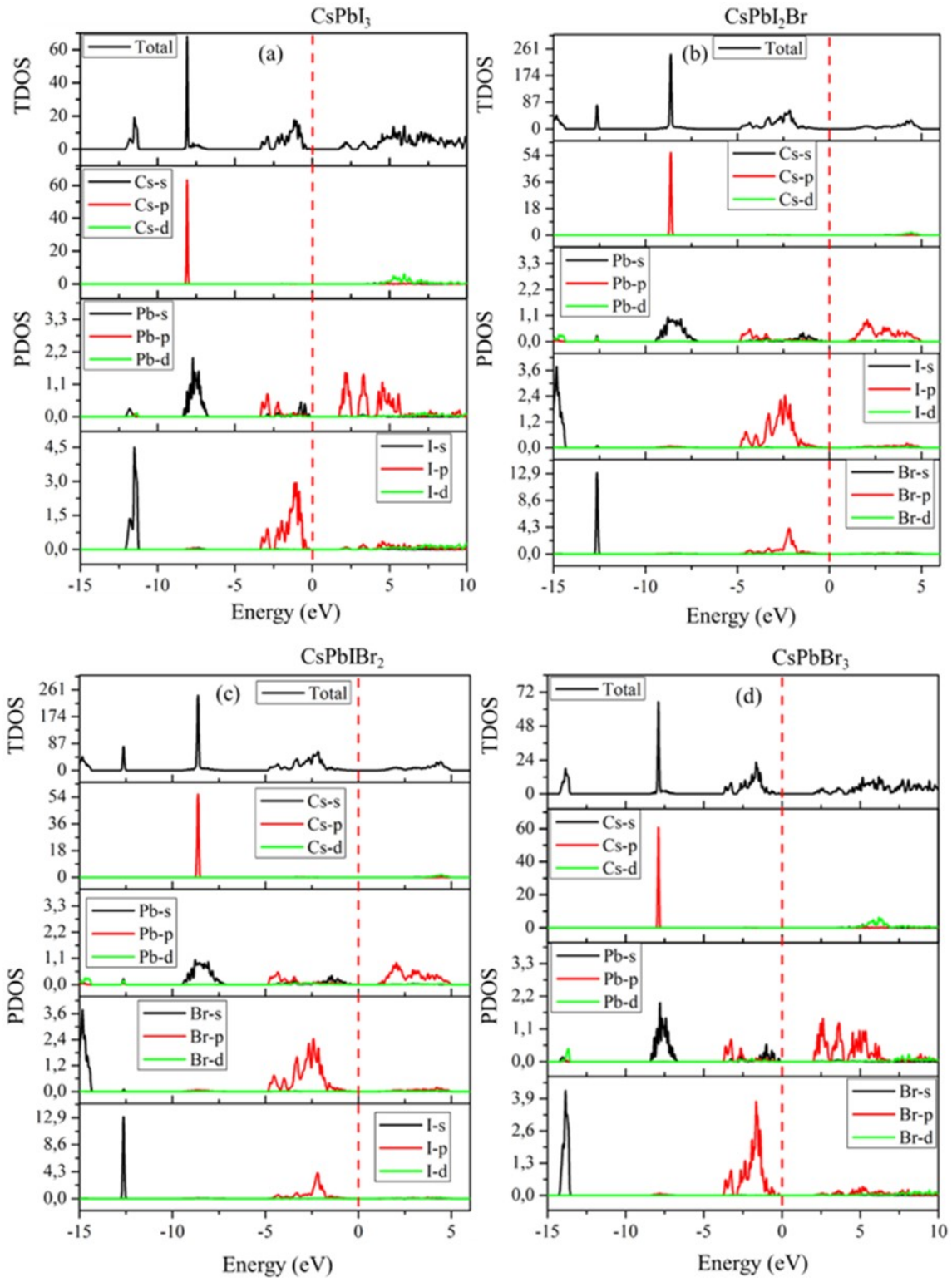


Figure A.1: Total and partial density of states for (a) $CsPbI_3$, (b) $CsPbI_2Br$, (c) $CsPbIBr_2$ and (d) $CsPbBr_3$ perovskites using GGA.

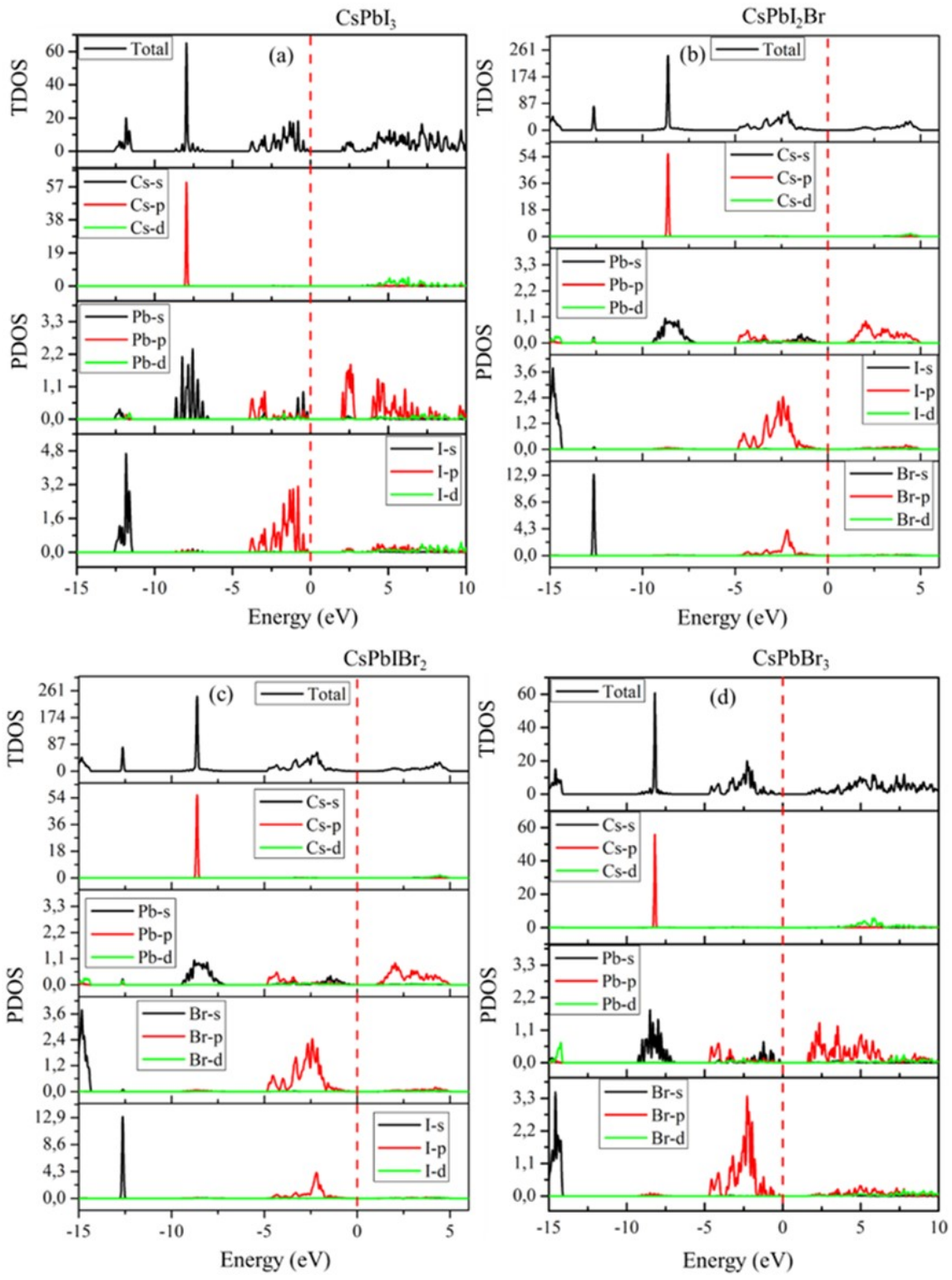


Figure A.2: Total and partial density of states for (a) $CsPbI_3$, (b) $CsPbI_2Br$, (c) $CsPbIBr_2$ and (d) $CsPbBr_3$ perovskites using LDA.

References

[1] J.P. Dorian, H.T. Franssen, and D.R. Simbeck. Global challenges in energy. *Energy Policy*, 34(15):1984–1991, 2006.

[2] B.K. Bose. Global warming: Energy, environmental pollution, and the impact of power electronics. *IEEE Industrial Electronics Magazine*, 4(1):6–17, 2010.

[3] A.M. Bagher, M.M.A. Vahid, and M. Mohsen. Types of solar cells and application. *American Journal of Optics and Photonics*, 3(5):94–113, 2015.

[4] T.C.J. Yang, P. Fiala, Q. Jeangros, and C. Ballif. High-bandgap perovskite materials for multijunction solar cells. *Joule*, 2(8):1421–1436, 2018.

[5] M.J. Bierman and S. Jin. Potential applications of hierarchical branching nanowires in solar energy conversion. *Energy and Environmental Science*, 2(10):1050–1059, 2009.

[6] Y. Wu, W. Chen, G. Chen, L. Liu, Z. He, and R. Liu. The impact of hybrid compositional film/structure on organic–inorganic perovskite solar cells. *Nanomaterials*, 8 (6):356, 2018.

[7] J.C. Germino, R. Szostak, S.G. Motti, R.F. Moral, P.E. Marchezi, H.S. Seleghini, L.G. Bonato, F.L. de Araújo, T.D. Atvars, L.M. Herz, and Fenning D. Postpassivation of multication perovskite with rubidium butyrate. *ACS Photonics*, 7(8): 2282–2291, 2020.

[8] T. He, Y. Jiang, X. Xing, and M. Yuan. Structured perovskite light absorbers for efficient and stable photovoltaics. *Advanced Materials*, 32(26):1903937, 2020.

[9] Y. Hu, L. Song, Y. Chen, and W. Huang. Two-terminal perovskites tandem solar cells: recent advances and perspectives. *Solar RRL*, 3(7):1900080, 2019.

[10] X.K. Liu, W. Xu, S. Bai, Y. Jin, J. Wang, R.H. Friend, and F. Gao. Metal halide perovskites for light-emitting diodes. *Nature Materials*, 20(1):10–21, 2021.

[11] W. Xie, Z. Gao, K. Liu, W.P. Pan, R. Vaia, D. Hunter, and A. Singh. Thermal characterization of organically modified montmorillonite. *Thermochimica Acta*, 367: 339–350, 2001.

[12] T. Leijtens, K. Bush, R. Cheacharoen, R. Beal, A. Bowring, and M.D. McGehee. Towards enabling stable lead halide perovskite solar cells; interplay between structural, environmental, and thermal stability. *Journal of Materials Chemistry A*, 5(23): 11483–11500, 2017.

[13] H. Choi, J. Jeong, H.B. Kim, S. Kim, B. Walker, G.H. Kim, and J.Y. Kim. Cesium-doped methylammonium lead iodide perovskite light absorber for hybrid solar cells. *Nano Energy*, 7:80–85, 2014.

[14] D.P. McMeekin, G. Sadoughi, W. Rehman, G.E. Eperon, M. Saliba, M.T. Hörantner, A. Haghighirad, N. Sakai, L. Korte, B. Rech, and Johnston M.B. A mixed-cation lead mixed-halide perovskite absorber for tandem solar cells. *Science*, 351(6269): 151–155, 2016.

[15] Y. Gao, Y. Dong, K. Huang, C. Zhang, B. Liu, S. Wang, J. Shi, H. Xie, H. Huang, S. Xiao, and J. He. Highly efficient, solution-processed $CsPbI_2Br$ planar heterojunction perovskite solar cells via flash annealing. *ACS Photonics*, 5(10):4104–4110, 2018.

[16] C.F.J. Lau, X. Deng, J. Zheng, J. Kim, Z. Zhang, M. Zhang, J. Bing, B. Wilkinson, L. Hu, R. Patterson, and S. Huang. Enhanced performance via partial lead replacement with calcium for a $CsPbI_3$ perovskite solar cell exceeding 13% power conversion efficiency. *Journal of Materials Chemistry A*, 6(14):5580–5586, 2018.

[17] R.G. Wilks and M. Bär. Perovskite solar cells: Danger from within. *Nature Energy*, 2(1):1–2, 2017.

[18] X. He. Perovskite photovoltaics: Current status and outlook. *Translational Materials Research*, 2:030301, 2015.

[19] V. Arjun, K.P. Muthukumaran, K. Ramachandran, A. Nithya, and S. Karuppuchamy. Fabrication of efficient and stable planar perovskite solar cell using copper oxide as hole transport material. *Journal of Alloys and Compounds*, 923:166285, 2022.

[20] K.T. Butler. The chemical forces underlying octahedral tilting in halide perovskites. *Journal of Materials Chemistry C*, 6(44):12045–12051, 2018.

[21] J.M. Frost and A. Walsh. Molecular motion and dynamic crystal structures of hybrid halide perovskites. *Organic-Inorganic Halide Perovskite Photovoltaics: From Fundamentals to Device Architectures*, 2016.

[22] S.C. Tidrow. Mapping comparison of goldschmidt's tolerance factor with perovskite structural conditions. *Ferroelectrics*, 470(1):13–27, 2014.

[23] D. Ji, S. Feng, L. Wang, S. Wang, M. Na, H. Zhang, C. Zhang, and X. Li. Regulatory tolerance and octahedral factors by using vacancy in $APbI_3$ perovskites. *Vacuum*, 164:186–193, 2019.

[24] S. Dastidar, D.A. Egger, L.Z. Tan, S.B. Cromer, A.D. Dillon, S. Liu, L. Kronik, A.M. Rappe, and A.T. Fafarman. High chloride doping levels stabilize the perovskite phase of cesium lead iodide. *Nano Letters*, 16(6):3563–3570, 2016.

[25] C.C. Stoumpos and M.G. Kanatzidis. The renaissance of halide perovskites and their evolution as emerging semiconductors. *Accounts of Chemical Research*, 48 (10):2791–2802, 2015.

[26] T. Rath, J. Handl, S. Weber, B. Friesenbichler, P. Fürk, L. Troi, T. Dimopoulos, B. Kunert, R. Resel, and G. Trimmel. Photovoltaic properties of a triple cation methylammonium/formamidinium/phenylethylammonium tin iodide perovskite. *Journal of Materials Chemistry A*, 7(16):9523–9529, 2019.

[27] M. Petrović, V. Chellappan, T. Ye, and S. Ramakrishna. Charge carrier decay and diffusion in organic-inorganic $CH_3NH_3PbI_{3-x}Cl_x$ perovskite based solar cell. *Physica Status Solidi (RRL)–Rapid Research Letters*, 9(12):682–686, 2015.

[28] G.E. Eperon, S.D. Stranks, C. Menelaou, M.B. Johnston, L.M. Herz, and H.J. Snaith. Formamidinium lead trihalide: a broadly tunable perovskite for efficient planar heterojunction solar cells. *Energy and Environmental Science*, 7(3):982–988, 2014.

[29] J.S. Manser, J.A. Christians, and P.V. Kamat. Intriguing optoelectronic properties of metal halide perovskites. *Chemical Reviews*, 116(21):12956–13008, 2016.

[30] J. Song, W. Hu, X.F. Wang, G. Chen, W. Tian, and T. Miyasaka. $HC(NH_2)_2PbI_3$ as a thermally stable absorber for efficient ZnO-based perovskite solar cells. *Journal of Materials Chemistry A*, 4(21):8435–8443, 2016.

[31] A.A. Zhumekenov, M.I. Saidaminov, A. Haque, E. Alarousu, S.P. Sarmah, B. Murali, I. Dursun, X.H. Miao, A.L. Abdelhady, T. Wu, and O.F. Mohammed. Formamidinium lead halide perovskite crystals with unprecedented long carrier dynamics and diffusion length. *ACS Energy Letters*, 1(1):32–37, 2016.

[32] D.N. Minh, J. Kim, J. Hyon, J.H. Sim, H.H. Sowlih, C. Seo, J. Nam, S. Eom, S. Suk, S. Lee, and E. Kim. Room-temperature synthesis of widely tunable formamidinium

lead halide perovskite nanocrystals. *Chemistry of Materials*, 29(13):5713–5719, 2017.

[33] Y. Zhou, M. Yang, S. Pang, K. Zhu, and N.P. Padture. Exceptional morphology-preserving evolution of formamidinium lead triiodide perovskite thin films via organic-cation displacement. *Journal of the American Chemical Society*, 138(17): 5535–5538, 2016.

[34] J.H. Noh, S.H. Im, J.H. Heo, T.N. Mandal, and S.I. Seok. Chemical management for colorful, efficient, and stable inorganic–organic hybrid nanostructured solar cells. *Nano Letters*, 13(4):1764–1769, 2013.

[35] Y. Ying, X. Luo, and H. Huang. Pressure-induced topological nontrivial phase and tunable optical properties in all-inorganic halide perovskites. *The Journal of Physical Chemistry C*, 122(31):17718–17725, 2018.

[36] U.G. Jong, C.J. Yu, Y.H. Kye, S.N. Hong, and H.G. Kim. Manifestation of the thermoelectric properties in Ge-based halide perovskites. *Physical Review Materials*, 4 (7):075403, 2020.

[37] S. Masi, A.F. Gualdrón-Reyes, and I. Mora-Sero. Stabilization of black perovskite phase in $FAPbI_3$ and $CsPbI_3$. *ACS Energy Letters*, 5(6):1974–1985, 2020.

[38] C.Y. Chen, H.Y. Lin, K.M. Chiang, W.L. Tsai, Y.C. Huang, C.S. Tsao, and H.W. Lin. All-vacuum-deposited stoichiometrically balanced inorganic cesium lead halide perovskite solar cells with stabilized efficiency exceeding 11%. *Advanced Materials*, 29(12):1605290, 2017.

[39] G.E. Eperon, G.M. Paternò, R.J. Sutton, A. Zampetti, A.A. Haghighirad, F. Cacialli, and H.J. Snaith. Inorganic cesium lead iodide perovskite solar cells. *Journal of Materials Chemistry A*, 3(39):19688–19695, 2015.

[40] A. Swarnkar, A.R. Marshall, E.M. Sanehira, B.D. Chernomordik, D.T. Moore, J.A. Christians, T. Chakrabarti, and J.M. Luther. Quantum dot–induced phase stabilization of α-$CsPbI_3$ perovskite for high-efficiency photovoltaics. *Science*, 354(6308): 92–95, 2016.

[41] M. Kulbak, S. Gupta, N. Kedem, I. Levine, T. Bendikov, G. Hodes, and D. Cahen. Cesium enhances long-term stability of lead bromide perovskite-based solar cells. *The Journal of Physical Chemistry Letters*, 7(1):167–172, 2016.

[42] Q. Ma, S. Huang, S. Chen, M. Zhang, C.F.J. Lau, M.N. Lockrey, H.K. Mulmudi, Y. Shan, J. Yao, J. Zheng, and X. Deng. The effect of stoichiometry on the stability of

inorganic cesium lead mixed-halide perovskites solar cells. *The Journal of Physical Chemistry C*, 121(36):19642–19649, 2017.

[43] C.F.J. Lau, X. Deng, Q. Ma, J. Zheng, J.S. Yun, M.A. Green, S. Huang, and A.W.Y. Ho-Baillie. $CsPbIBr_2$ perovskite solar cell by spray-assisted deposition. *ACS Energy Letters*, 1(3):573–577, 2016.

[44] R.E. Brandt, V. Stevanović, D.S. Ginley, and T. Buonassisi. Identifying defect-tolerant semiconductors with high minority-carrier lifetimes: beyond hybrid lead halide perovskites. *Mrs Communications*, 5(2):265–275, 2015.

[45] M. Saliba, T. Matsui, K. Domanski, J.Y. Seo, A. Ummadisingu, S.M. Zakeeruddin, J.P. Correa-Baena, W.R. Tress, A. Abate, A. Hagfeldt, and M. Grätzel. Incorporation of rubidium cations into perovskite solar cells improves photovoltaic performance. *Science*, 354(6309):206–209, 2016.

[46] D.M. Trots and S.V. Myagkota. High-temperature structural evolution of caesium and rubidium triiodoplumbates. *Journal of Physics and Chemistry of Solids*, 69(10): 2520–2526, 2008.

[47] P. Pitriana, T.D.K. Wungu, H. Herman, and R. Hidayat. Electronic structure calculations of alkali lead iodide ($APbI_3$ A = Li, Na, K, Rb or Cs) using density functional theory method. *Journal of Physics: Conference Series*, 1204(1):012107, 2019.

[48] F. Zheng, W. Chen, T. Bu, K.P. Ghiggino, F. Huang, Y. Cheng, P. Tapping, T.W. Kee, B. Jia, and X. Wen. Triggering the passivation effect of potassium doping in mixed-cation mixed-halide perovskite by light illumination. *Advanced Energy Materials*, 9(24):1901016, 2019.

[49] J. Chang, Z. Lin, H. Zhu, F.H. Isikgor, Q.H. Xu, C. Zhang, Y. Hao, and J. Ouyang. Enhancing the photovoltaic performance of planar heterojunction perovskite solar cells by doping the perovskite layer with alkali metal ions. *Journal of Materials Chemistry A*, 4(42):16546–16552, 2016.

[50] J.K. Nam, S.U. Chai, W. Cha, Y.J. Choi, W. Kim, M.S. Jung, J. Kwon, D. Kim, and J.H. Park. Potassium incorporation for enhanced performance and stability of fully inorganic cesium lead halide perovskite solar cells. *Nano Letters*, 17(3):2028–2033, 2017.

[51] M. Roknuzzaman, J.A. Alarco, H. Wang, and K.K. Ostrikov. Structural, electronic and optical properties of lead-free antimony-copper based hybrid double perovskites for photovoltaics and optoelectronics by first principles calculations. *Computational Materials Science*, 186:110009, 2021.

[52] W.J. Yin, T. Shi, and Y. Yan. Unique properties of halide perovskites as possible origins of the superior solar cell performance. *Advanced Materials*, 26(27):4653–4658, 2014.

[53] Y. Zhao and K. Zhu. Solution chemistry engineering toward high-efficiency perovskite solar cells. *The Journal of Physical Chemistry Letters*, 5(23):4175–4186, 2014.

[54] W. Ahmad, J. Khan, G. Niu, and J. Tang. Inorganic $CsPbI_3$ perovskite-based solar cells: A choice for a tandem device. *Solar RRL*, 1(7):1700048, 2017.

[55] H. Yuan, Y. Zhao, Y. Duan, J.and Wang, X. Yang, and Q. Tang. All-inorganic $CsPbBr_3$ perovskite solar cell with 10.26% efficiency by spectra engineering. *Journal of Materials Chemistry A*, 6(47):24324–24329, 2018.

[56] J.Y. Kim, J.W. Lee, H.S. Jung, H. Shin, and N.G. Park. High-efficiency perovskite solar cells. *Chemical Reviews*, 120(15):7867–7918, 2020.

[57] T.M. Brenner, D.A. Egger, L. Kronik, G. Hodes, and D. Cahen. Hybrid organic-inorganic perovskites: low-cost semiconductors with intriguing charge-transport properties. *Nature Reviews Materials*, 1(1):1–16, 2016.

[58] S. Xu, A. Libanori, G. Luo, and J. Chen. Engineering bandgap of $CsPbI_3$ over 1.7 eV with enhanced stability and transport properties. *Iscience*, 24(3):102235, 2021.

[59] J. Yuan, L. Zhang, C. Bi, M. Wang, and J. Tian. Surface trap states passivation for high-performance inorganic perovskite solar cells. *Solar RRL*, 2(10):1800188, 2018.

[60] H. Zhang, C. Liang, M. Sun, F. Sun, C. Ji, X. Wan, D. Li, F. You, and Z. He. Controlled crystallization of CsRb-based multi-cation perovskite using a blended sequential process for high-performance solar cells. *Solar RRL*, 5(5):2100050, 2021.

[61] S. Shao and M.A. Loi. The role of the interfaces in perovskite solar cells. *Advanced Materials Interfaces*, 7(1):1901469, 2020.

[62] Z.E. Shi, S.H. Liu, C.H. Tsai, C.W. Li, C.P. Chen, and Y.H. Yu. Enhancing charge transport performance of perovskite solar cells by using reduced graphene oxide-cysteine/nanogold hybrid material in the active layer. *FlatChem*, 28:100254, 2021.

[63] V.M. Le Corre, M. Stolterfoht, L. Perdigon Toro, M. Feuerstein, C. Wolff, L. Gil-Escrig, H.J. Bolink, D. Neher, and L.J.A. Koster. Charge transport layers limiting the efficiency of perovskite solar cells: how to optimize conductivity, doping, and thickness. *ACS Applied Energy Materials*, 2(9):6280–6287, 2019.

[64] J. Liang, C. Wang, Y. Wang, Z. Xu, Z. Lu, Y. Ma, H. Zhu, Y. Hu, C. Xiao, X. Yi, and G. Zhu. All-inorganic perovskite solar cells. *Journal of the American Chemical Society*, 138(49):15829–15832, 2016.

[65] B.W. Park, S.M. Jain, X. Zhang, A. Hagfeldt, G. Boschloo, and T. Edvinsson. Resonance raman and excitation energy dependent charge transfer mechanism in halide-substituted hybrid perovskite solar cells. *ACS Nano*, 9(2):2088–2101, 2015.

[66] S. Pitchaiya, M. Natarajan, A. Santhanam, V. Asokan, A. Yuvapragasam, V.M. Ramakrishnan, S.E. Palanisamy, S. Sundaram, and D. Velauthapillai. A review on the classification of organic/inorganic/carbonaceous hole transporting materials for perovskite solar cell application. *Arabian Journal of Chemistry*, 13(1):2526–2557, 2020.

[67] J. Burschka, N. Pellet, S.J. Moon, R. Humphry-Baker, Peng Gao, M.K. Nazeeruddin, and M. Grätzel. Sequential deposition as a route to high-performance perovskite-sensitized solar cells. *Nature*, 499(7458):316–319, 2013.

[68] J.H. Heo, S.H. Im, J.H. Noh, T.N. Mandal, C.S. Lim, J.A. Chang, Y.H. Lee, H.J. Kim, A. Sarkar, M.K. Nazeeruddin, and M. Grätzel. Efficient inorganic–organic hybrid heterojunction solar cells containing perovskite compound and polymeric hole conductors. *Nature Photonics*, 7(6):486–491, 2013.

[69] H. Chen, X. Pan, W. Liu, M. Cai, D. Kou, Z. Huo, X. Fang, and S. Dai. Efficient panchromatic inorganic–organic heterojunction solar cells with consecutive charge transport tunnels in hole transport material. *Chemical Communications*, 49(66): 7277–7279, 2013.

[70] R. He, S. Nie, X. Huang, Y. Wu, R. Chen, J. Yin, B. Wu, J. Li, and N. Zheng. Scalable preparation of high-performance ZnO–SnO_2 cascaded electron transport layer for efficient perovskite solar modules. *Solar RRL*, 6(3):2100639, 2022.

[71] J. Han, H. Kwon, E. Kim, D.W. Kim, H.J. Son, and D.H. Kim. Interfacial engineering of a ZnO electron transporting layer using self-assembled monolayers for high performance and stable perovskite solar cells. *Journal of Materials Chemistry A*, 8 (4):2105–2113, 2020.

[72] N. Cheng, P. Liu, S. Bai, Z. Yu, W. Liu, S.S. Guo, and X.Z. Zhao. Application of mesoporous SiO_2 layer as an insulating layer in high performance hole transport material free $CH_3NH_3PbI_3$ perovskite solar cells. *Journal of Power Sources*, 321: 71–75, 2016.

[73] T. Saga. Advances in crystalline silicon solar cell technology for industrial mass production. *NPG Asia Materials*, 2(3):96–102, 2010.

[74] S. Bhattacharya and S. John. Beyond 30% conversion efficiency in silicon solar cells: a numerical demonstration. *Scientific Reports*, 9(1):12482, 2019.

[75] A. Bosio, S. Pasini, and N. Romeo. The history of photovoltaics with emphasis on CdTe solar cells and modules. *Coatings*, 10(4):344, 2020.

[76] J. Ramanujam and U.P. Singh. Copper indium gallium selenide based solar cells-a review. *Energy and Environmental Science*, 10(6):1306–1319, 2017.

[77] P.M. Maleka, R.S. Dima, O.M. Ntwaeaborwa, and R.R. Maphanga. Study of inorganic lead halide perovskites properties using first-principles density functional theory for photovoltaic and optoelectronic devices. *Materials Today: Proceedings*, 62:S12–S22, 2022.

[78] P.M. Maleka, R.S. Dima, O.M. Ntwaeaborwa, and R.R. Maphanga. Density functional theory study of br doped $CsPbI_3$ perovskite for photovoltaic and optoelectronic applications. *Physica Scripta*, 98(4):045505, 2023.

[79] M. Faghihnasiri, M. Izadifard, and M.E. Ghazi. Dft study of mechanical properties and stability of cubic methylammonium lead halide perovskites ($CH_3NH_3PbX_3$, X = I, Br, Cl). *The Journal of Physical Chemistry C*, 121(48):27059–27070, 2017.

[80] T.B. Song, Q. Chen, H. Zhou, C. Jiang, H.H. Wang, Y.M. Yang, Y. Liu, J. You, and Y. Yang. Perovskite solar cells: film formation and properties. *Journal of Materials Chemistry A*, 3(17):9032–9050, 2015.

[81] J. Cui, H. Yuan, J. Li, X. Xu, Y. Shen, H. Lin, and M. Wang. Recent progress in efficient hybrid lead halide perovskite solar cells. *Science and Technology of Advanced Materials*, 2015.

[82] S. Ghosh, A. Mallick, B. Dou, M.F. Van Hest, S.M. Garner, and D. Basak. A novel blanket annealing process to achieve highly transparent and conducting al doped ZnO thin films: Its mechanism and application in perovskite solar cells. *Solar Energy*, 174:815–825, 2018.

[83] D. Di Girolamo, F. Di Giacomo, F. Matteocci, A.G. Marrani, D. Dini, and A. Abate. Progress, highlights and perspectives on nio in perovskite photovoltaics. *Chemical Science*, 11(30):7746–7759, 2020.

[84] J.J. Yoo, G. Seo, M.R. Chua, T.G. Park, Y. Lu, F. Rotermund, Y.K. Kim, C.S. Moon, N.J. Jeon, J.P. Correa-Baena, and V. Bulović. Efficient perovskite solar cells via improved carrier management. *Nature*, 590(7847):587–593, 2021.

[85] Y. Zhou, J. Chen, O.M. Bakr, and H.T. Sun. Metal-doped lead halide perovskites: synthesis, properties, and optoelectronic applications. *Chemistry of Materials*, 30 (19):6589–6613, 2018.

[86] M. Roknuzzaman, K. Ostrikov, H. Wang, A. Du, and T. Tesfamichael. Towards lead-free perovskite photovoltaics and optoelectronics by ab-initio simulations. *Scientific Reports*, 7(1):14025, 2017.

[87] A. Natik, Y. Abid, R. Moubah, F. Khelfaoui, E.K. Hlil, H. Zaari, A. Benyoussef, M. Abid, and H. Lassri. Structural, elastic, electronic and optical properties of $RbPbI_3$ perovskites studied using ab-initio calculations. *Phase Transitions*, 93(1): 54–61, 2020.

[88] Y. Cui, S. Wang, L. Ding, and F. Hao. Green-solvent-processable perovskite solar cells. *Advanced Energy and Sustainability Research*, 2(2):2000047, 2021.

[89] H.S. Kim, Y.J. An, J.I. Kwak, H.J. Kim, H.S. Jung, and N.G. Park. Sustainable green process for environmentally viable perovskite solar cells. *ACS Energy Letters*, 7(3): 1154–1177, 2022.

[90] J. Xu, Z. Hu, L. Huang, X. Huang, X. Jia, J. Zhang, J. Zhang, and Y. Zhu. In situ recycle of PbI_2 as a step towards sustainable perovskite solar cells. *Progress in Photovoltaics: Research and Applications*, 25(12):1022–1033, 2017.

[91] I. Chung, B. Lee, J. He, R.P. Chang, and M.G. Kanatzidis. All-solid-state dye-sensitized solar cells with high efficiency. *Nature*, 485(7399):486–489, 2012.

[92] Y. Yamada, T. Nakamura, M. Endo, A. Wakamiya, and Y. Kanemitsu. Near-band-edge optical responses of solution-processed organic–inorganic hybrid perovskite $CH_3NH_3PbI_3$ on mesoporous TiO_2 electrodes. *Applied Physics Express*, 7(3): 032302, 2014.

[93] D. Sabba, H.K. Mulmudi, R.R. Prabhakar, T. Krishnamoorthy, T. Baikie, P.P. Boix, S. Mhaisalkar, and N. Mathews. Impact of anionic Br^- substitution on open circuit voltage in lead free perovskite ($CsSnI_{3-x}Br_x$) solar cells. *The Journal of Physical Chemistry C*, 119(4):1763–1767, 2015.

[94] B. Wu, Y. Zhou, G. Xing, Q. Xu, H.F. Garces, A. Solanki, T.W. Goh, N.P. Padture, and T.C. Sum. Long minority-carrier diffusion length and low surface-recombination velocity in inorganic lead-free $CsSnI_3$ perovskite crystal for solar cells. *Advanced Functional Materials*, 27(7):1604818, 2017.

[95] M.H. Kumar, S. Dharani, W.L. Leong, P.P. Boix, R.R. Prabhakar, T. Baikie, C. Shi, H. Ding, R. Ramesh, M. Asta, and M. Graetzel. Lead-free halide perovskite solar cells with high photocurrents realized through vacancy modulation. *Advanced Materials*, 26(41):7122–7127, 2014.

[96] T. Krishnamoorthy, H. Ding, C. Yan, W.L. Leong, T. Baikie, Z. Zhang, M. Sherburne, S. Li, M. Asta, N. Mathews, and S.G. Mhaisalkar. Lead-free germanium iodide perovskite materials for photovoltaic applications. *Journal of Materials Chemistry A*, 3(47):23829–23832, 2015.

[97] L.J. Chen. Synthesis and optical properties of lead-free cesium germanium halide perovskite quantum rods. *RSC Advances*, 8(33):18396–18399, 2018.

[98] S. Zou, Y. Liu, J. Li, C. Liu, R. Feng, F. Jiang, Y. Li, J. Song, H. Zeng, M. Hong, and X. Chen. Stabilizing cesium lead halide perovskite lattice through Mn (ii) substitution for air-stable light-emitting diodes. *Journal of the American Chemical Society*, 139(33):11443–11450, 2017.

[99] Q.A. Akkerman, D. Meggiolaro, Z. Dang, F. De Angelis, and L. Manna. Fluorescent alloy $CsPb_xMn_{1-x}I_3$ perovskite nanocrystals with high structural and optical stability. *ACS Energy Letters*, 2(9):2183–2186, 2017.

[100] M. Saliba, T. Matsui, J.Y. Seo, K. Domanski, J.P. Correa-Baena, M.K. Nazeeruddin, S.M. Zakeeruddin, W. Tress, A. Abate, A. Hagfeldt, and M. Grätzel. Cesium-containing triple cation perovskite solar cells: improved stability, reproducibility and high efficiency. *Energy and Environmental Science*, 9(6):1989–1997, 2016.

[101] L. Protesescu, S. Yakunin, M.I. Bodnarchuk, F. Krieg, R. Caputo, C.H. Hendon, R.X. Yang, A. Walsh, and M.V. Kovalenko. Nanocrystals of cesium lead halide perovskites ($CsPbX_3$, X = Cl, Br, and I): novel optoelectronic materials showing bright emission with wide color gamut. *Nano Letters*, 15(6):3692–3696, 2015.

[102] J.F. Liao, W.G. Li, H.S. Rao, B.X. Chen, X.D. Wang, H.Y. Chen, and D.B. Kuang. Inorganic cesium lead halide $CsPbX_3$ nanowires for long-term stable solar cells. *Science China Materials*, 4(60):285–294, 2017.

[103] W. Chen, H. Chen, G. Xu, R. Xue, S. Wang, Y. Li, and Y. Li. Precise control of crystal growth for highly efficient $CsPbI_2Br$ perovskite solar cells. *Joule*, 3(1): 191–204, 2019.

[104] P. Hohenberg and W. Kohn. Inhomogeneous electron gas. *Physical Review*, 136 (3B):B864, 1964.

[105] W. Kohn and L.J. Sham. Self-consistent equations including exchange and correlation effects. *Physical Review*, 140(4A):A1133, 1965.

[106] E. Engel and R.M. Dreizler. Density functional theory. *Theoretical and Mathematical Physics*, 102:11–56.

[107] J. Kohanoff. *Electronic Structure Calculations for Solids and Molecules: Theory and Computational Methods*. Cambridge University Press, 2006.

[108] R.M. Martin. *Electronic Structure: Basic Theory and Practical Methods*. Cambridge University Press, 2020.

[109] J.C. Inkson. *Many-Body Theory of Solids: An Introduction*. Springer Science and Business Media, 2012.

[110] E. Kaxiras. *Atomic and Electronic Structure of Solids*. Cambridge University Press, 2003.

[111] M. Born and R. Oppenheimer. *On the Quantum Theory of Molecules*. World Scientific, 2000.

[112] A.D. Becke. A new mixing of hartree-fock and local density-functional theories. *The Journal of Chemical Physics*, 98(2):1372–1377, 1993.

[113] J.C. Slater. The theory of complex spectra. *Physical Review*, 34(10):1293, 1929.

[114] G. Kresse and J. Furthmüller. Efficient iterative schemes for *ab initio* total-energy calculations using a plane-wave basis set. *Physical Review B*, 54(16):11169, 1996.

[115] C. Lee, W. Yang, and R.G. Parr. Development of the colle-salvetti correlation-energy formula into a functional of the electron density. *Physical Review B*, 37(2): 785, 1988.

[116] J.P. Perdew and K. Schmidt. Jacob's ladder of density functional approximations for the exchange-correlation energy. 577(1):1–20, 2001.

[117] J.P. Perdew, K. Burke, and M. Ernzerhof. Generalized gradient approximation made simple. *Physical Review Letters*, 77(18):3865, 1996.

[118] J.P. Perdew, S. Kurth, A. Zupan, and P. Blaha. Accurate density functional with correct formal properties: A step beyond the generalized gradient approximation. *Physical Review Letters*, 82(12):2544, 1999.

[119] Y. Zhao and D.G. Truhlar. A new local density functional for main-group thermochemistry, transition metal bonding, thermochemical kinetics, and noncovalent interactions. *The Journal of Chemical Physics*, 125(19):194101, 2006.

[120] J. Tao, J.P. Perdew, V.N. Staroverov, and G.E. Scuseria. Climbing the density functional ladder: Nonempirical meta–generalized gradient approximation designed for molecules and solids. *Physical Review Letters*, 91(14):146401, 2003.

[121] F. Tran, P. Blaha, and K. Schwarz. Band gap calculations with becke-johnson exchange potential. *Journal of Physics: Condensed Matter*, 19(19):196208, 2007.

[122] T.M. Henderson, B.G. Janesko, and G.E. Scuseria. Range separation and local hybridization in density functional theory. *The Journal of Physical Chemistry A*, 112 (49):12530–12542, 2008.

[123] P.J. Stephens, F.J. Devlin, C.F. Chabalowski, and M.J. Frisch. *Ab initio* calculation of vibrational absorption and circular dichroism spectra using density functional force fields. *The Journal of Physical Chemistry*, 98(45):11623–11627, 1994.

[124] K.S. Kim and K.D. Jordan. Comparison of density functional and mp2 calculations on the water monomer and dimer. *The Journal of Physical Chemistry*, 98(40): 10089–10094, 1994.

[125] V.I. Anisimov and O. Gunnarsson. Density-functional calculation of effective coulomb interactions in metals. *Physical Review B*, 43(10):7570, 1991.

[126] I.I. Mazin and V.I. Anisimov. Insulating gap in feo: Correlations and covalency. *Physical Review B*, 55(19):12822, 1997.

[127] J. Hubbard and B.H. Flowers. Proceedings of the royal society of london, series a. *Mathematical Physical Sciences*, 276(1365):238, 1963.

[128] J. Hubbard. Electron correlations in narrow energy bands. ii. the degenerate band case. *Proceedings of the Royal Society of London. Series A. Mathematical and Physical Sciences*, 277(1369):237–259, 1964.

[129] F. Bloch. Über die quantenmechanik der elektronen in kristallgittern. *Zeitschrift für Physik*, 52(7-8):555–600, 1929.

[130] M.C. Payne, M.P. Teter, D.C. Allan, T.A. Arias, and A.J. Joannopoulos. Iterative minimization techniques for ab initio total-energy calculations: molecular dynamics and conjugate gradients. *Reviews of Modern Physics*, 64(4):1045, 1992.

[131] L. Kleinman and D.M. Bylander. Efficacious form for model pseudopotentials. *Physical Review Letters*, 48(20):1425, 1982.

[132] D.R. Hamann, M. Schlüter, and C. Chiang. Norm-conserving pseudopotentials. *Physical Review Letters*, 43(20):1494, 1979.

[133] D. Vanderbilt. Soft self-consistent pseudopotentials in a generalized eigenvalue formalism. *Physical Review B*, 41(11):7892, 1990.

[134] David J Singh and Lars Nordstrom. *Planewaves, Pseudopotentials, and the LAPW method*. Springer Science & Business Media, 2006.

[135] D.J. Chadi and M.L. Cohen. Tight-binding calculations of the valence bands of diamond and zinc blende crystals. *Lawrence Berkeley National Laboratory*, 1974.

[136] H.J. Monkhorst and J.D. Pack. Special points for brillouin-zone integrations. *Physical Review B*, 13(12):5188, 1976.

[137] C. Wolverton and D. de Fontaine. Cluster expansions of alloy energetics in ternary intermetallics. *Physical Review B*, 49(13):8627, 1994.

[138] D. Lerch, O. Wieckhorst, G.L. Hart, R.W. Forcade, and S. Müller. Uncle: a code for constructing cluster expansions for arbitrary lattices with minimal user-input. *Modelling and Simulation in Materials Science and Engineering*, 17(5):055003, 2009.

[139] L.J. Sham and M. Schlüter. Density-functional theory of the band gap. *Physical Review B*, 32(6):3883, 1985.

[140] A. Authier. *International Tables for Crystallography: Volume D: Physical Properties of Crystals*. Wiley Online Library, 2003.

[141] R.S. Mulliken. Electronic population analysis on lcao–mo molecular wave functions. i. *The Journal of Chemical Physics*, 23(10):1833–1840, 1955.

[142] C. Ambrosch-Draxl and J.O. Sofo. Linear optical properties of solids within the full-potential linearized augmented planewave method. *Computer Physics Communications*, 175(1):1–14, 2006.

[143] S. Kamran, K. Chen, and L. Chen. *Ab initio* examination of ductility features of fcc metals. *Physical Review B*, 79(2):024106, 2009.

[144] J.F. Nye. *Physical Properties of Crystals: Their Representation by Tensors and Matrices*. Oxford University Press, 1985.

[145] R. Hill. The elastic behaviour of a crystalline aggregate. *Proceedings of the Physical Society. Section A*, 65(5):349, 1952.

[146] H. Effenberger, K. Mereiter, and J. Zemann. Crystal structure refinements of magnesite, calcite, rhodochrosite, siderite, smithonite, and dolomite, with discussion of some aspects of the stereochemistry of calcite type carbonates. *Zeitschrift für Kristallographie-Crystalline Materials*, 156(1-4):233–244, 1981.

[147] F. Mouhat and F.X. Coudert. Necessary and sufficient elastic stability conditions in various crystal systems. *Physical Review B*, 90(22):224104, 2014.

[148] A.E. Mattsson, P.A. Schultz, M.P. Desjarlais, T.R. Mattsson, and K. Leung. Designing meaningful density functional theory calculations in materials science-a primer. *Modelling and Simulation in Materials Science and Engineering*, 13(1):R1, 2004.

[149] V. Tvergaard and J.W. Hutchinson. Microcracking in ceramics induced by thermal expansion or elastic anisotropy. *Journal of the American Ceramic Society*, 71(3): 157–166, 1988.

[150] D. Connétable and O. Thomas. First-principles study of the structural, electronic, vibrational, and elastic properties of orthorhombic nisi. *Physical Review B*, 79(9): 094101, 2009.

[151] P. Ravindran, L. Fast, P.A. Korzhavyi, B. Johansson, J. Wills, and O. Eriksson. Density functional theory for calculation of elastic properties of orthorhombic crystals: Application to $TiSi_2$. *Journal of Applied Physics*, 84(9):4891–4904, 1998.

[152] Charles Kittel. *Introduction to solid state physics*. John Wiley & sons, inc, 2005.

[153] Dae-Hyun Chung. Elastic moduli of single crystal and polycrystalline mgo. *Philosophical Magazine*, 8(89):833–841, 1963.

[154] O.L. Anderson. A simplified method for calculating the debye temperature from elastic constants. *Journal of Physics and Chemistry of Solids*, 24(7):909–917, 1963.

[155] J. Hafner. *Ab-initio* simulations of materials using VASP: Density-functional theory and beyond. *Journal of Computational Chemistry*, 29(13):2044–2078, 2008.

[156] G.H. Murtaza and I. Ahmad. First principle study of the structural and optoelectronic properties of cubic perovskites $CsPbM_3$ (M = Cl, Br, I). *Physica B: Condensed Matter*, 406(17):3222–3229, 2011.

[157] R. Rajeswarapalanichamy, R. Padmavathy A. Amudhavalli, and K. Iyakutti. Band gap engineering in halide cubic perovskites $CsPbBr_{3-y}I_y$ (y= 0, 1, 2, 3) a dft study. *Materials Science and Engineering: B*, 258:114560, 2020.

[158] A. Najim, B. Hartiti, H. Absike, H.J.T. Nkuissi, H. Labrim, S. Fadili, P. Thevenin, and M. Ertugrul. Theoretical investigation of structural, electronic, and optical properties of halide cubic perovskite $CsPbBr_{3-x}I_x$. *Materials Science in Semiconductor Processing*, 141:106442, 2022.

[159] M. Ahmad, L. G. Rehman, M. Ali, R. Shafiq, R. Iqbal, T. Ahmad, S. Khan, M. Jalali-Asadabadi, and I. Ahmad Maqbool. Structural, electronic and optical properties of $CsPbX_3$ (X= Cl, Br, I) for energy storage and hybrid solar cell applications. *Journal of Alloys and Compounds*, 705:828–839, 2017.

[160] H.M. Ghaithan, Z.A. Alahmed, and M. Hezam S.M. Qaid, and A.S. Aldwayyan. Density functional study of cubic, tetragonal, and orthorhombic $CsPbBr_3$ perovskite. *ACS Omega*, 5(13):7468–7480, 2020.

[161] J. Qian, Bin B. Xu, and W. Tian. A comprehensive theoretical study of halide perovskites ABX_3. *Organic Electronics*, 37:61–73, 2016.

[162] M. Afsari, A. Boochani, and M. Hantezadeh. Electronic, optical and elastic properties of cubic perovskite $CsPbI_3$: Using first principles study. *Optik*, 127(23):11433–11443, 2016.

[163] D.H. Chung and W.R. Buessem. The voigt-reuss-hill approximation and elastic moduli of polycrystalline MgO, CaF_2, β-ZnS, ZnSe, and CdTe. *Journal of Applied Physics*, 38(6):2535–2540, 1967.

[164] G. Kresse and D. Joubert. From ultrasoft pseudopotentials to the projector augmented-wave method. *Physical Review B*, 59(3):1758, 1999.

[165] M.B. Kanoun, S. Goumri-Said, U. Schwingenschlögl, and A. Manchon. Magnetism in Sc-doped ZnO with zinc vacancies: A hybrid density functional and GGA+U approaches. *Chemical Physics Letters*, 532:96–99, 2012.

[166] S. Ghosal, K. Dutta, S. Chowdhury, and D. Jana. Importance of the hubbard u parameter to explore accurate electronic and optical behaviour of $BiFeO_3$. *Journal of Physics D: Applied Physics*, 55(37):375303, 2022.

[167] F. Tang, Y. Yao, D. Cao, J. Yan, J. Wang, Z. Jiang, Y. Zhou, Z. Jiao, and H. Shu. Structural stability and optoelectronic properties of lead-free halide perovskite $CsSnBr_3$ by introducing transition-metal dopants. *Journal of Electronic Materials*, 51(7):3438–3444, 2022.

[168] Y.H. Chang, C.H. Park, and K. Matsuishi. First-principles study of the structural and the electronic properties of the lead-halide-based inorganic-organic perovskites $(CH_3NH_3)PbX_3$ and $CsPbX_3$ (X = Cl, Br, I). *Journal-Korean Physical Society*, 44: 889–893, 2004.

[169] M.R. Filip, G.E. Eperon, H.J. Snaith, and F. Giustino. Steric engineering of metal-halide perovskites with tunable optical band gaps. *Nature Communications*, 5(1): 5757, 2014.

[170] J. Meng, Z. Lan, W. Lin, M. Liang, X. Zou, Q. Zhao, H. Geng, I.E. Castelli, T. Canton, S.E. Pullerits, and K. Zheng. Optimizing the quasi-equilibrium state of hot carriers in all-inorganic lead halide perovskite nanocrystals through mn doping: fundamental dynamics and device perspectives. *Chemical Science*, 13(6):1734–1745, 2022.

[171] M. Liu, N. Jiang, H. Huang, J. Lin, F. Huang, Y. Zheng, and D. Chen. Ni^{2+}-doped $CsPbI_3$ perovskite nanocrystals with near-unity photoluminescence quantum yield and superior structure stability for red light-emitting devices. *Chemical Engineering Journal*, 413:127547, 2021.

[172] S.K. Mitro, K.M. Hossain, R. Majumder, and M.Z. Hasan. Effect of the negative chemical pressure on physical properties of doped perovskite molybdates in the framework of dft method. *Journal of Alloys and Compounds*, 854:157088, 2021.

[173] K. Yang, D.F. Li, W.Q. Huang, L. Xu, G.F. Huang, and S. Wen. Origin of enhanced visible-light photocatalytic activity of transition-metal (fe, cr and co)-doped CeO_2: effect of 3 d orbital splitting. *Applied Physics A*, 123:1–11, 2017.

[174] X. Liu, B. Xie, C. Duan, Z. Wang, B. Fan, K. Zhang, B Lin, F.J. Colberts, W. Ma, R.A. Janssen, and F. Huang. A high dielectric constant non-fullerene acceptor for efficient bulk-heterojunction organic solar cells. *Journal of Materials Chemistry A*, 6(2):395–403, 2018.

[175] H.S. Kim, C.R. Lee, J.H. Im, K.B. Lee, T. Moehl, A. Marchioro, Soo-Jin Moon, Robin Humphry-Baker, Jun-Ho Yum, Jacques E Moser, et al. Lead iodide perovskite sensitized all-solid-state submicron thin film mesoscopic solar cell with efficiency exceeding 9%. *Scientific Reports*, 2(1):591, 2012.

[176] G.R. Yettapu, D. Talukdar, S. Sarkar, A. Swarnkar, A. Nag, P. Ghosh, and P. Mandal. Terahertz conductivity within colloidal $CsPbBr_3$ perovskite nanocrystals: remarkably high carrier mobilities and large diffusion lengths. *Nano Letters*, 16(8): 4838–4848, 2016.

[177] H.T. Xue, X.D. Yu, J. Aarons, F.L. Tang, X.F. Lu, and J.Q. Ren. Cluster expansion Monte Carlo study of indium-aluminum segregation and homogenization in $CuInSe_2$-$CuAlSe_2$ pseudobinary alloys. *Physical Chemistry Chemical Physics*, 22 (26):14694–14703, 2020.

[178] S. Sharma, N. Weiden, and A. Weiss. Phase diagrams of quasibinary systems of the type: ABX_3—A; ABX_3—AB, and ABX_3—ABX; X= halogen. *Zeitschrift für Physikalische Chemie*, 175(Part_1):63–80, 1992.

[179] S.I. Ranganathan and M. Ostoja-Starzewski. Universal elastic anisotropy index. *Physical Review Letters*, 101(5):055504, 2008.

[180] Z. Ping, L. Zhifeng, Z. Mu, H. Chenghua, Z. Zhou, and W. Jinghe. First-principle study of phase stability, electronic structure and thermodynamic properties of cadmium sulfide under high pressure. *Journal of Physics and Chemistry of Solids*, 75 (5):662–669, 2014.

List of Publications and Presentations

Refereed Journals/Manuscripts Under Preparation

1. P.M. Maleka, R.S. Dima, O.M. Ntwaeaborwa, and R.R. Maphanga, Study of inorganic lead halide perovskites properties using first-principles density functional theory for photovoltaic and opto-electronic devices, *Materials Today: Proceedings*, 2022, vol. 62, S12–S22.

2. P.M. Maleka, R.S. Dima, O.M. Ntwaeaborwa, and R.R. Maphanga, Density functional theory study of Br doped $CsPbI_3$ perovskite for photovoltaic and opto-electronic applications, *Physica Scripta*, 2023, vol. 98, 045505.

3. P.M. Maleka, R.S. Dima, O.M. Ntwaeaborwa, and R.R. Maphanga, A comparative study on Mn-doped $CsPbI_3$ and $CsPbBr_3$ using first principle-based DFT. In South African Institute of Physics 67^{th} Annual Conference (SAIP 2023), ISBN: 978-0-7961-3774-6, Dec 2023. Available online at http://events.saip.org.za.

4. P.M. Maleka, R.S. Dima, O.M. Ntwaeaborwa, and R.R. Maphanga, A combined cluster expansion, Monte Carlo and DFT study of $CsPb(I/Br)_3$ Perovskites for Photovoltaic and Optoelectronic Devices. *MDPI*, 2023, vol. 29, 92.

Conference Abstracts/Posters/Presentations

1. P.M. Maleka, R.S. Dima, O.M. Ntwaeaborwa, and R.R. Maphanga, Study of inorganic lead halide perovskites properties using first-principles density functional theory for photovoltaic and opto-electronic devices, *The* 66^{th} *Annual Conference of the South African Institute of Physics*, The Department of Physics at Nelson Mandela University, South Africa, 4-7 July 2022.

2. P.M. Maleka, R.S. Dima, D.M. Tshwane, O.M. Ntwaeaborwa, and R.R. Maphanga, Density Functional Theory Study of Zn Doped $CsPbI_3$ Perovskite for Photovoltaic and Opto-electronic Applications, *The* 67^{th} *Annual Conference of the South African*

Institute of Physics, The Department of Physics at University of Zululand Richards Bay Campus, 3-7 July 2023.

3. P.M. Maleka, R.S. Dima, D.M. Tshwane, O.M. Ntwaeaborwa, and R.R. Maphanga, Phase separation of Br-doped $CsPbI_3$: A combined cluster expansion, Monte Carlo and DFT study, *CCP2023 - 34th IUPAP Conference on Computational Physics*, Kobe International Conference Center, Kobe Port Island, Kobe, Japan, 4-8 August 2023.